

MASS MEASUREMENTS OF NEUTRON-RICH COBALT ISOTOPES
BEYOND $N=40$ AND THE DEVELOPMENT OF A SINGLE ION
PENNING TRAP MASS SPECTROMETER FOR RARE ISOTOPES

By

Christopher John Izzo

A DISSERTATION

Submitted to
Michigan State University
in partial fulfillment of the requirements
for the degree of

Physics - Doctor of Philosophy

2018

ABSTRACT

MASS MEASUREMENTS OF NEUTRON-RICH COBALT ISOTOPES BEYOND $N=40$ AND THE DEVELOPMENT OF A SINGLE ION PENNING TRAP MASS SPECTROMETER FOR RARE ISOTOPES

By

Christopher John Izzo

Over the past few decades, the use of online Penning trap mass spectrometry (PTMS) has enabled precise, accurate mass measurements of rare isotopes as a probe of nuclear structure far from the valley of beta stability. As the first and only Penning trap coupled to a projectile fragmentation facility, the Low Energy Beam and Ion Trap (LEBIT) facility at the National Superconducting Cyclotron Laboratory allows precision mass measurements of exotic nuclei that are not available at other PTMS facilities.

The nuclear shell model provides a robust framework for understanding nuclear structure effects. While nuclear shell structure is well understood for stable isotopes, the evolution of nuclear structure away from stability remains an active area of rare isotope research. The region near $Z = 28$ and $N = 40$ is a subject of great interest for nuclear structure studies due to spectroscopic signatures in ^{68}Ni suggesting a subshell closure at $N = 40$. Trends in nuclear masses do not appear to support this conclusion, however a complete picture of the mass surfaces in this region has so far been limited by the large uncertainty remaining for nuclei with $N > 40$ along the iron ($Z = 26$) and cobalt ($Z = 27$) chains because these species are not available at traditional isotope separator online (ISOL) facilities. Recent Penning trap mass measurements of $^{68,69}\text{Co}$ at LEBIT provide the first precise examination of nuclear masses beyond $N = 40$ in the Co chain. The motivation, procedure, and results of these measurements are presented in this dissertation. Recent theoretical calculations for these isotopes are also presented, and the importance of these measurements and calculations for

understanding the evolution of nuclear structure near ^{68}Ni is discussed.

In order to expand the reach of LEBIT to isotopes very far away from stability, a new Single Ion Penning Trap (SIPT) has been developed. Many rare isotopes far from stability can only be produced at very low rates incompatible with the current destructive measurement technique used for online PTMS, which requires ~ 100 ions or more to complete a mass measurement. SIPT employs a non-destructive measurement technique which enables complete mass determinations with a single ion. This technique has been used successfully at other facilities for stable particle measurements but has never before been extended to measurements of exotic radioisotopes. The design and offline commissioning tests of SIPT are presented in this work, demonstrating promising outlook for single ion rare isotope measurements in the near future.

ACKNOWLEDGMENTS

Graduate school has presented me with many of the most challenging and rewarding experiences of my life so far, and I owe an enormous debt of gratitude to everyone who helped me navigate this period of my life. First I would like to thank my advisor, Georg Bollen, whose enthusiasm for his research first convinced me to join the LEBIT team. Thank you to Georg for giving me the opportunity to take part in such exciting and important projects, for allowing me to travel to conferences and summer school programs to continue my professional development, and for challenging me to become a better scientist. Thank you as well to the other members of my committee, Alexandra Gade, Vladimir Zelevinsky, Dave Morrissey, and Stuart Tessmer, for taking the time to guide me through the process of completing my PhD and providing helpful feedback at each of our meetings.

I also want to say a huge thank you to Ryan Ringle for supervising me throughout my graduate research. Despite his feelings towards Harry Potter and raspberry beer, Ryan has still been the best mentor I could have hoped for during this formative period of my career.

The work of this thesis would not have been possible without the support of many collaborators who helped me along the way. In particular, I want to thank Matt Redshaw for teaching me the art of FT-ICR detection, Jason Holt for providing valuable theory input to help with the interpretation of my thesis data, and Chandana Sumithrarachchi for many helpful discussions that taught me how to be a “real” nuclear experimentalist.

I have been extremely fortunate to work with an incredible team of LEBIT postdocs and students. During their time as postdocs, Kerim Gulyuz and Martin Eibach were invaluable resources for me as a new grad student with a million questions. I want to thank Adrian Valverde and Rachel Sandler, the other LEBIT graduate students for my first few years in

the group, for their support and friendship. I also have to acknowledge the new guard of LEBIT students, Alec Hamaker, Isaac Yandow, Daniel Puentes, and 0.5*(Jason Surbrook), for making the last part of my time with LEBIT an absolute blast. Best of luck to you guys, try not to destroy the lab once I'm gone and remember to stay clear of Danny's "sangria."

I can't say thank you enough to the many wonderful friends I have made during my time at MSU. I am forever grateful for everyone who took part in the many hallway chats, lunches in the atrium, apartment hangouts, wine nights, study sessions, physics choir rehearsals, board games, Lugnuts games, karaoke nights, movie nights, trivia nights, and countless other adventures over the last five years. A special thank you to Wei Jia Ong, Amy Lovell, and Josh Bradt for providing an incredible support system throughout grad school (particularly during the first couple years when I was drowning in problem sets) and for many much-needed moments of levity and moments of sincerity that always came at just the right time.

Thank you as well to the old HF crew for continuing to support me even as we all scatter around the country and settle into our adult lives. Christine, Emily, Lawrence, Rabia, Renee, Sam, and Steve, you all are my role models. I also have to thank Lindsey Steinberg, whose friendship means more than I can find the words to say.

Thank you to the Chicago Cubs for finally winning the World Series. Seriously, that was a big moment for me.

Finally, I want to acknowledge my incredible family. My parents have shown me so much love and support in every one of my endeavors, and that means the world to me. My sisters, Beth and Cindy, are two of the best people I know and they continually inspire me to be a better person. Most of all, I want to acknowledge my grandparents. My happiness and success are direct products of the sacrifices they made and the loving family structures they worked to build. I will never forget their many stories, jokes, and life lessons.

TABLE OF CONTENTS

LIST OF TABLES	viii
LIST OF FIGURES	ix
Chapter 1 Introduction	1
1.1 Importance of Atomic Masses for Nuclear Science	1
1.1.1 Evolution of Nuclear Structure Away From Stability	2
1.2 Mass Measurements of Rare Isotopes	4
1.3 Motivation for a Non-Destructive Mass Measurement Technique	6
Chapter 2 Penning Trap Mass Spectrometry	9
2.1 Penning Trap Basic Concepts	9
2.1.1 Trapping Fields	9
2.1.2 Ion Motion in a Penning Trap	10
2.1.3 Manipulation of Ion Motion with RF Electric Fields	12
2.2 Overview of Penning Trap Mass Spectrometry	14
2.3 TOF-ICR Technique	18
2.4 FT-ICR Technique	21
Chapter 3 The LEBIT Mass Spectrometer Facility at the NSCL	24
3.1 Beam Stopping at the NSCL	26
3.2 Major Components of the LEBIT Facility	28
3.2.1 Offline Ion Sources	29
3.2.2 Cooler/buncher and Fast Electrostatic Kicker	30
3.2.3 TOF-ICR Penning Trap	32
3.2.4 SIPT	33
Chapter 4 Mass Measurements of Neutron-Rich Cobalt Isotopes Beyond N=40	34
4.1 Motivation for Mass Measurements of $^{68,69}\text{Co}$	34
4.1.1 Evidence for a Subshell Closure at $N = 40$	34
4.1.2 Mass Measurements Around $N = 40$	36
4.2 Experimental Procedure	40
4.2.1 Gas Cell Chemistry	40
4.2.2 SWIFT Beam Purification	43
4.2.3 Isomer Investigations	45
4.3 Results and Discussion	46
4.3.1 Mass Measurement Results	46
4.3.2 Level Assignment	48
4.3.3 Evaluation of Two-Neutron Separation Energy Trends	53

Chapter 5	Development of a Single Ion Penning Trap Mass Spectrometer for Rare Isotopes	58
5.1	SIPT Concept and Requirements	58
5.2	The SIPT Beamline	62
5.3	The SIPT Penning Trap	65
5.3.1	Spectrometer Design	65
5.3.1.1	The SIPT Magnet	65
5.3.1.2	Penning Trap Electrode System	66
5.3.1.3	Cryogenic System	69
5.3.1.4	TOF-ICR Detection	71
5.3.1.5	FT-ICR Detection Circuit Design	72
5.3.2	Controls and Data Acquisition	76
5.4	Offline Commissioning of the Single Ion Penning Trap	78
5.4.1	Room Temperature Commissioning	78
5.4.2	Cryogenic Commissioning	80
5.4.2.1	Cooling to 4 K	80
5.4.2.2	Resonator Circuit Response	83
Chapter 6	Summary and Outlook	88
APPENDICES		90
Appendix A	Characterization of the MiniTrap Magnetometer	91
Appendix B	Evaluation of Systematic Frequency Shifts for SIPT	98
Appendix C	Limiting Case Ratio of ^{68}Co β -Decaying States	104
BIBLIOGRAPHY		109

LIST OF TABLES

Table 1.1: Areas of rare-isotope research and typical precisions required to probe the associated physics using mass measurements.	2
Table 4.1: Comparison of conditions for Run 1 and Run 2.	44
Table 4.2: Measured frequency ratios, $\nu_c/\nu_{c,\text{ref}}$, calculated atomic mass and mass excess (ME) values, and their comparison to the values from 2016 Atomic Mass Evaluation. Differences in the mass excess values, $\Delta\text{ME} = \text{ME}_{\text{LEBIT}} - \text{ME}_{\text{AME2016}}$, are also listed.	48
Table 5.1: Parameters used to estimate the achievable S/N for narrowband FT-ICR measurements with a single ion.	61
Table 5.2: Oxford magnet specifications as provided by the supplier.	66
Table 5.3: SIPT Penning trap dimensions (see Fig. 5.6.)	68
Table 5.4: Vendor specifications for PT415 cryorefrigerator with CP1110 helium compressor from Cryomech, Inc.	70

LIST OF FIGURES

Figure 1.1:	The chart of the nuclides, with each nuclide colored according to its currently known mass precision. Mass precisions come from the most recent Atomic Mass Evaluation (AME2016) [1].	2
Figure 2.1:	Three hyperbolic trap electrodes (two end cap electrodes and one ring electrode) used to create the quadrupolar electrostatic field necessary for axial ion confinement.	10
Figure 2.2:	Illustration of the motion of a charged particle in a Penning trap. This motion is a combination of three distinct eigenmotions: the magnetron motion (green) at frequency ω_- , the modified cyclotron motion (red) at frequency ω_+ , and the axial oscillations (blue) at frequency ω_z . The black path illustrates the combination of these three motions.	12
Figure 2.3:	Applied RF geometries used to obtain dipole (left) and quadrupole (right) excitations of the ions' motion in the Penning trap. At LEBIT, the ring electrode is segmented to achieve these geometries. Red and blue segments represent RF applications of equal frequency and amplitude, 180° out of phase.	13
Figure 2.4:	Conversion between the two radial modes of an ion's motion in a Penning trap. (a) The ion begins with pure magnetron motion (red circle). When a quadrupole RF drive is applied at the true cyclotron frequency ν_c , the modified cyclotron radius grows as seen by the growing black circles, and the magnetron radius decreases as indicated by the blue arrow. (b) When full conversion of magnetron to modified cyclotron motion is complete, the modified cyclotron radius is equal to the initial magnetron radius. . .	14
Figure 2.5:	Ions ejected from the Penning trap move through an axial magnetic field gradient as they travel to the MCP detector. This results in an axial kick proportional to the ions' radial energy, as demonstrated by Eq. (2.10). .	19
Figure 2.6:	Example of a TOF-ICR resonance obtained by scanning the applied RF quadrupole excitation frequency and measuring the ions' time of flight to an MCP detector. The red curve is a theoretical fit, the center of which corresponds the cyclotron frequency ν_c	20
Figure 2.7:	Schematic illustration of narrowband FT-ICR detection.	23

Figure 3.1:	Layout of the NSCL. Rare isotope beams from the A1900 are delivered either directly to fast beam experiments or to the beam stopping facility, from which stopped beams are sent to low-energy experiments including LEBIT or to the re-accelerator facility for intermediate energy experiments. (Adapted from http://nscl.msu.edu/public/virtual-tour.html .)	25
Figure 3.2:	Photo of the ANL gas cell used for beam stopping at the NSCL.	27
Figure 3.3:	Layout of the LEBIT facility. The functions of each major component are described in the text. (Reproduced from https://groups.nsl.msu.edu/lebit/lebitfacility/index.html .)	28
Figure 3.4:	Photo of the Colutron ion source which produces stable and long-lived ions via plasma or surface ionization.	29
Figure 3.5:	Photo of the laser ablation ion source at LEBIT.	30
Figure 3.6:	Photos of the LEBIT cooler/buncher used to prepare cooled ion bunches for delivery to the Penning trap. The pre-cooler and micro-RFQ are shown on the left, and the buncher stage is shown on the right.	31
Figure 3.7:	The 9.4-T superconducting magnet (left) and hyperbolic Penning trap electrode structure (right) used for TOF-ICR measurements at LEBIT.	32
Figure 3.8:	Photo of the recently-commissioned SIPT beamline, used for ion transfer from the cooler/buncher to the 7-T SIPT magnet for FT-ICR measurements. Details on individual components of this beamline are presented in Section 5.2	33
Figure 4.1:	Single-particle shell model energy levels using a harmonic oscillator potential plus an l^2 interaction without spin-orbit interaction (left) and with spin-orbit interaction (right).	35
Figure 4.2:	First-excited 2^+ state energies E_{2^+} (top) and $B(E2; 0^+ \rightarrow 2^+)$ transition strengths (bottom) in the even-even nickel isotopes. All data taken from Ref. [74]. The large E_{2^+} and the small $B(E2)$ values at $N = 40$ suggest a substantial shell gap.	36
Figure 4.3:	Two-neutron separation energy S_{2n} plotted as a function of neutron number N in the region from $Z = 31$ to $Z = 50$. Data are taken from the AME2016 atomic mass evaluation [1].	38

Figure 4.4:	Two-neutron separation energy S_{2n} plotted as a function of neutron number N in the region around ^{68}Ni . Data are taken from the AME2016 atomic mass evaluation [1].	39
Figure 4.5:	Radioactivity observed as a function of the m/q value transmitted through the dipole mass separator for Runs 1 and 2. The effect of CID is seen by comparing the case where there is no bias applied to the gas cell extraction to the case where a -150 V offset is applied. Note that m/q was scanned from high values to low in Run 1 and from low values to high in Run 2, hence the opposite directions of the decay tails.	42
Figure 4.6:	Attempted TOF-ICR resonances of $^{68}\text{Co}^{2+}$ with SWIFT off (left) and SWIFT on (right). A significant amount of unidentified stable contamination from the gas cell arrived at $m/q = 34$, obscuring the resonance before SWIFT was turned on. The use of SWIFT to clean unidentified contaminants made this measurement possible.	45
Figure 4.7:	Schematic overview of the major experimental components used for this work.	46
Figure 4.8:	The β -delayed γ -ray spectrum detected following the decay of ^{68}Co . Dashed vertical lines mark the energies of γ rays known to follow primarily decay from only one of the two β -decaying states of ^{68}Co . γ rays at 478 keV follow decay from the low-spin state and γ rays at 324 and 595 keV follow decay from the high-spin state. The presence of clear peaks at 324 and 595 keV and the lack of a peak at 478 keV suggest that the high-spin β -decaying state of ^{68}Co was measured in this experiment. Other peaks in the spectrum have all been identified from either natural background radiation or ^{68}Co decays common to both β -decaying states.	50
Figure 4.9:	Simplified level scheme showing the relevant β -delayed gamma rays for the two β -decaying states of ^{68}Co . Circled gamma energies are those that signal the presence of one state or the other, but not both. Energies are all given in keV. Based on data from [88, 94, 95].	50
Figure 4.10:	Two-neutron separation energies S_{2n} plotted as a function of neutron number N for isotopes of iron, cobalt, nickel, and copper. Green square points correspond to new cobalt values from this work and black circles correspond to data from AME2016 [1]. Points plotted with an x marker indicate values derived not from purely experimental data in the AME2016.	54

Figure 4.11: Neutron shell gap Δ_N plotted as a function of neutron number N for isotopes of iron, cobalt, nickel, and copper. The green curve corresponds to new cobalt values from this work and the black curves correspond to data from AME2016 [1]. Points plotted with an x marker indicate values derived not from purely experimental data in the AME2016. Inset: Neutron shell gap plotted as a function of proton number Z for isotopes with $N = 40$ neutrons.	56
Figure 4.12: Two-neutron separation energies S_{2n} plotted as a function of neutron number N for the nickel isotopic chain. The solid black data are taken from AME2016, and the dashed lines correspond to IM-SRG theoretical calculations. Blue triangles use a ^{40}Ca core for $N \leq 40$ (pf neutron valence space) and a ^{60}Ca core for $N > 40$ (sdg neutron valence space). Red squares use a $pf_{5/2}g_{9/2}$ valence space for protons and neutrons for the entire chain starting from a ^{56}Ni core.	57
Figure 5.1: Frequency domain fit precision as a function of signal-to-noise ratio for simulated single ion signals from $^{78}\text{Ni}^+$ and $^{100}\text{Sn}^+$	61
Figure 5.2: Layout of the major components of the new SIPT beamline.	62
Figure 5.3: 115° cylindrical bender, with integrated electrostatic quadrupole doublets on each end and a quadrupole singlet in the middle for transverse beam focusing.	63
Figure 5.4: Simulated ion trajectories through the SIPT beamline, from the kicker to the 7-T SIPT magnet.	64
Figure 5.5: Design drawing and photograph of the drift tube assembly used for ion injection/ejection to/from the SIPT Penning trap.	65
Figure 5.6: Design drawing of the SIPT Penning trap corrected hyperbolic electrode system. Trap dimensions given in Table 5.3.	68
Figure 5.7: SIPT Penning trap electrodes before assembly (left), partway through assembly (middle) and after assembly (right).	68
Figure 5.8: Overview of the SIPT cryogenic system components.	71
Figure 5.9: Conceptual overview of reverse ion extraction for TOF-ICR measurements with SIPT.	72
Figure 5.10: Schematic circuit diagram of the SIPT cryogenic filtering and detection electronics.	73

Figure 5.11: Flowcharts outlining the SIPT data acquisition process currently used for offline testing (left) and that envisioned for future online experiments (right).	77
Figure 5.12: Screenshots of the Qt-based user interface used for control of SIPT hardware devices including power supplies, AFGs, vacuum pumps, and gate valves.	78
Figure 5.13: 10 ms TOF-ICR resonance of ν_c for $^{39}\text{K}^+$ using reverse ion extraction from the SIPT Penning trap to the SIPT Daly MCP.	79
Figure 5.14: Demonstration of broadband FT-ICR detection with SIPT at room temperature. The ion peak seen in this figure comes from picking up the image current generated by the modified cyclotron motion of many (~ 1000) $^{39}\text{K}^+$ ions. The data presented here is the average of five consecutive shots, each of which used a 256 ms acquisition time.	80
Figure 5.15: SIPT 4 K stage wrapped in Mylar to reduce radiative heating from the surrounding 45 K stage. Two layers of Mylar wrapping were necessary to reach temperatures of ~ 4 K.	81
Figure 5.16: 600 μH NbTi inductor coil (left) and NbTi inductor case (right) used for the high-Q SIPT FT-ICR detection circuit. The inductor coil consists of 194 turns of 250 μm NbTi wire with tubular Teflon coating wrapped around a Teflon core. The windings were then covered by an additional layer of Teflon tape, which provides both mechanical support and some additional amount of thermal conductivity.	82
Figure 5.17: SIPT 4 K chamber with all components mounted and wired (bottom). The design drawing of this region is included for reference (top).	83
Figure 5.18: Resistance across the NbTi inductor coil plotted over time alongside the temperature readings from the Cernox temperature sensors mounted on the cold head and the back of the SIPT Penning trap. Roughly 12 hours after the temperature sensors reached their minimum values, the NbTi coil cooled below its critical temperature and entered a superconducting state, as evidenced by the resistance drop to nearly 0 Ω .	84
Figure 5.19: Frequency domain response of the SIPT narrowband FT-ICR cryogenic detection circuit operating at ~ 5.2 K. This very narrow frequency response corresponds to a circuit Q factor of 2785, which is greater than what is required for single ion detection.	87

Figure A.1: A LabVIEW screenshot of FFT resonances of both modified cyclotron motion (left) and true cyclotron motion (right) of H_3O^+ ions measured with the MiniTrap magnetometer using a broadband FT-ICR quadrupole detection configuration.	93
Figure A.2: Results of the dipole cleaning scan used to determine the modified cyclotron frequency ν_+ of ionized background gas molecules in the MiniTrap magnetometer after it was moved to its current location in the 9.4-T LEBIT magnet.	94
Figure A.3: MiniTrap tuning scans used to determine the optimal ratio between the endcap and ring potentials. The trap depth was held constant at 10.4 V. A ratio of 9.15 to -1.25 between the end cap and ring potentials was found to produce the best approximation of a quadrupolar electrostatic potential because, at these settings, the measured ion frequency varied the least as the ions were driven to increasingly large radii.	94
Figure A.4: Amplitude (top) and center frequency (bottom) of the ν_+ peak in the FFT spectrum as a function of the applied RF excitation frequency. The plots on the left were obtained with a 200 mVpp RF excitation and the plots on the right were obtained with a 150 mVpp RF excitation. The observed behavior is discussed in the text.	95
Figure A.5: Frequency domain response of the MiniTrap room temperature resonant circuit used for narrowband FT-ICR detection of the true cyclotron motion of trapped H_3O^+ ions.	96
Figure B.1: Illustration of the misalignment angle θ between the magnetic field and the Penning trap axis.	99
Figure B.2: Frequency ratio shifts due to misalignment between the Penning trap axis and the magnetic field as a function of ion mass, assuming a 6 u mass difference between the ion of interest and the reference ion.	100
Figure B.3: Radar plots of the magnetic field strength in the SIPT magnet determined from NMR measurements after the magnet was energized.	102
Figure B.4: Relative modified cyclotron frequency shifts due to special relativity plotted as a function of modified cyclotron radius ρ_+ for ions of various masses in a 7-T magnetic field.	103

Chapter 1

Introduction

1.1 Importance of Atomic Masses for Nuclear Science

One of the most important concepts governing the properties and processes studied across many areas of nuclear science research is the binding energy which holds protons and neutrons together in an atomic nucleus. Owing to the well-known mass-energy equivalence given by Einstein's famous equation $E = mc^2$, the binding energy of a nucleus is directly reflected in the mass of the nucleus, as the total nuclear mass is the sum of the constituent nucleon masses minus the binding energy. Mass measurements therefore present a critical tool for probing a wide variety of nuclear effects. By comparing atomic mass differences between various isotopes and looking at mass trends across the nuclear chart, much information can be obtained for a number of research applications including nuclear structure, nuclear astrophysics, and fundamental interaction studies.

Fig. 1.1 shows the chart of the nuclides, with each nuclide colored by its currently known mass precision according to the most recent Atomic Mass Evaluation (AME2016) [1]. As seen in this chart, atomic masses are generally known to a very high degree of precision for most stable isotopes. The further one gets from stability, however, the less precisely the mass is generally known, owing to the difficulty of producing and studying such exotic isotopes. Table 1.1 shows typical mass precisions required for different areas of rare-isotope research [2].

Research Area	$\delta m/m$
Nuclear Structure	$\leq 10^{-6}$
Nuclear Astrophysics	$\leq 10^{-7}$
Nuclear Models and Formulae	$\leq 10^{-7}$
Weak Interaction	$\leq 10^{-8}$

Table 1.1: Areas of rare-isotope research and typical precisions required to probe the associated physics using mass measurements.

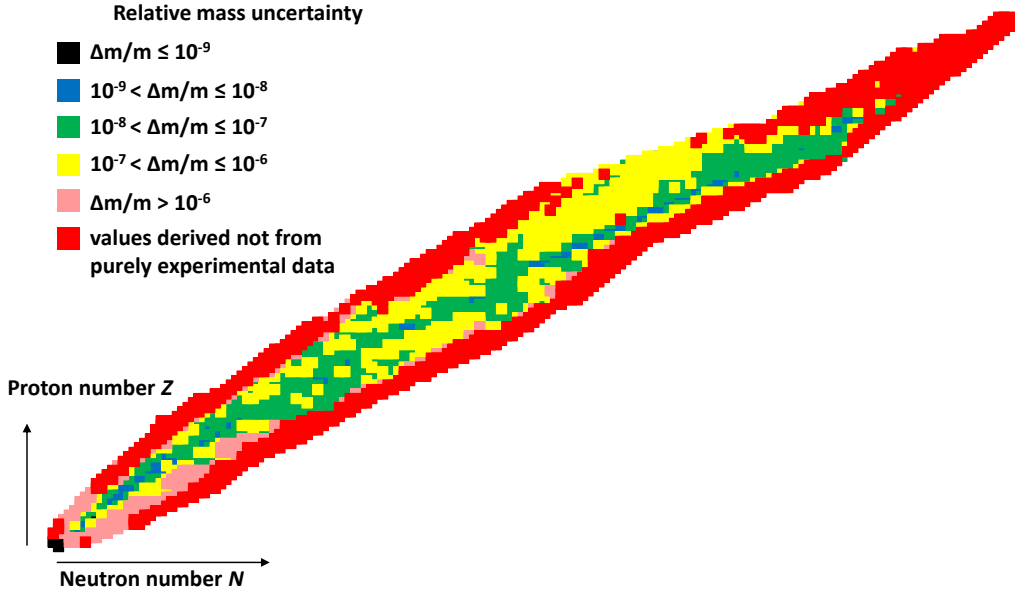


Figure 1.1: The chart of the nuclides, with each nuclide colored according to its currently known mass precision. Mass precisions come from the most recent Atomic Mass Evaluation (AME2016) [1].

Comparing Table 1.1 with Fig. 1.1, it is clear that an abundance of scientific motivation remains to complete precise mass measurements of rare isotopes away from stability.

1.1.1 Evolution of Nuclear Structure Away From Stability

The nuclear shell model plays a central role in understanding nuclear structure. A quantum-mechanical treatment of the protons and neutrons in a nuclear potential reveals the discrete quantum states that a nucleus can occupy. Large energy gaps, known as shell gaps, exist between certain clusters of orbitals, known as shells. These are analogous to the atomic

shells occupied by electrons in an atom. Just as closed-shell atoms (the inert gases) exhibit a high degree of chemical stability, closed-shell nuclei are similarly stable, and the properties of nuclei with nearly closed shells can typically be explained simply by the properties of a few valence nucleons or holes. The total number of nucleons needed to complete a proton or neutron shell is referred to a “magic number,” and nuclei with a magic number of both protons and neutrons are known as “doubly-magic” nuclei. The Nobel Prize was awarded in 1963 to Maria Goeppert-Mayer and J. Hans D. Jensen for their work on the nuclear shell model, demonstrating that the inclusion of a spin-orbit interaction could be used to reproduce the experimentally observed magic numbers [3, 4].

A major area of interest in current nuclear structure research is the evolution of shell structure away from stability. As early as 1960, Talmi and Unna demonstrated that the $N = 8$ shell gap is lost in neutron-rich beryllium isotopes [5]. In 1975, online mass spectrometry experiments suggested that the $N = 20$ neutron shell closure, well-established for stable isotopes around ^{40}Ca , may not persist for unstable isotopes with relatively large N/Z ratios [6]. This was later confirmed by additional experimental studies [7–9].

It is worth emphasizing the significance of this realization that the magic numbers, which provide such an important foundation for our understanding of nuclear structure, are not immutable as was previously believed. This sparked a rush of experimental and theoretical efforts to identify and explain further examples of evolving shell structure away from stability.

Significant progress has been made in this regard over the last few decades. Developments in rare isotope production have vastly expanded the range of exotic nuclei available for study, while developments in detection and measurement techniques have improved the accuracy and sensitivity of experimental studies. On the theoretical side, the effect of tensor [10] and three-body interactions [11–13] are now understood to play an important role in shifting the

relative spacing of shell model energy levels in regions of the nuclear chart far from stability, resulting in the disappearance of some magic numbers and the appearance of new ones.

An area of particular interest over the last few decades is the region around $N = 40$, $Z = 28$ due to experimental signatures suggesting the arrival of a magic number at $N = 40$ in the ${}_{28}\text{Ni}$ chain. This example is explored in Chapter 4, presenting new results from precise mass measurements of ${}_{27}\text{Co}$ isotopes beyond $N = 40$ which expand the understanding of nuclear structure in this region.

1.2 Mass Measurements of Rare Isotopes

The relation between atomic masses and binding energy discussed in Section 1.1 makes masses important probes for investigating nuclear trends away from stability. Mass determinations are generally categorized as either indirect or direct measurements. Indirect measurements rely on nuclear reaction or radioactive decay studies to determine mass differences, known as Q -values, between parent and daughter nuclei. Chains of Q -values can then be used to determine masses of isotopes far from stability. Uncertainties from each Q -value measurement accumulate in the final mass determination, with the result that indirect mass measurements of rare isotopes far from stability frequently come with a relatively high degree of uncertainty.

Direct mass measurements include those based on time-of-flight, frequency, magnetic rigidity, or some combination of these techniques. Time-of-flight measurements with mass spectrometers allow fast and highly sensitive measurements, which are important properties for measuring radioactive isotopes far from stability as such isotopes are often produced at low rates and decay in short timespans. Experiments such as SPEG at GANIL [14], TOFI

at LANL [15], and the S800 spectrograph at the NSCL [16] have successfully employed such methods for direct mass measurements of rare isotopes. At the RIKEN Radioactive Isotope Beam Factory, the time-of-flight magnetic-rigidity technique was used recently to perform the first direct mass measurements of the neutron-rich isotopes $^{55-57}\text{Ca}$ [17].

The obtainable precision of such measurements is limited by the ions' total time-of-flight, so a variety of strategies have been developed to extend the ions' path length and thus the travel time. The CSS2 cyclotron at GANIL [18] and SARA at Grenoble [19] used cyclotrons to send ions along a spiral path. Storage rings including the Experimental Storage Ring (ESR) at GSI [20] and the Heavy Ion Cooler-Storage-Ring (HIRFL-CSR) at Lanzhou [21] use many passes around a large circular ring to extend the path length. Multi-reflection time-of-flight (MR-TOF) devices use electrostatic reflectors to bounce ions back and forth within a small chamber for a set number of passes. MR-TOF devices have become very popular in the last few years because they are relatively compact and inexpensive to build, and can achieve very high mass resolutions when a large number of reflections are used [22–25]. Such devices are often used for beam purification, but have also demonstrated the ability to achieve high precision direct mass measurements of rare isotopes. For instance, the MR-TOF device at ISOLDE was used to explore nuclear structure trends far from stability along the Ca chain out to ^{54}Ca with sub-ppm mass precision [26].

The highest degree of mass precision and accuracy is achieved using Penning traps to measure the cyclotron frequency of ions confined in a strong magnetic field. These techniques are discussed in detail in Chapter 2. Penning trap mass spectrometry (PTMS) has been used to measure stable ions at mass precisions $\delta m/m < 10^{-10}$ [27] and unstable ions at precisions $< 10^{-8}$ [28]. The first demonstration that Penning traps could be implemented for precision mass measurements at a rare isotope facility was ISOLTRAP at the ISOLDE

facility [29]. The success of ISOLTRAP prompted the development of several other PTMS programs at various rare isotope facilities, including JYFLTRAP at Jyväskylä [30], CPT at Argonne National Lab [31], SHIPTRAP at GSI [32], LEBIT at NSCL [33], and TITAN at TRIUMF [34].

Among these facilities, the Low-Energy Beam and Ion Trap (LEBIT) facility at the National Superconducting Cyclotron Laboratory (NSCL) is the first and only Penning trap mass spectrometer coupled to a projectile fragmentation facility, allowing high-precision mass measurements of rare isotopes that are unavailable at other Penning trap facilities. Since its commissioning in 2005, LEBIT has successfully measured the masses of more than 65 different species, achieving mass precisions as low as ~ 2 ppb [28] and measuring species with half-lives below 100 ms [35]. The work discussed in this thesis was carried out at LEBIT, and the LEBIT facility is discussed in detail in Chapter 3.

1.3 Motivation for a Non-Destructive Mass Measurement Technique

One of the most significant difficulties associated with Penning trap mass measurements of isotopes far from stability is the extremely low production rates for such species. Much of the most groundbreaking rare-isotope research occurs at the edges of the nuclear chart, exploring the limits of nuclear binding and the changes in nuclear interactions that occur in such exotic nuclei. Rare-isotope-beam facilities are beginning to achieve the ability to produce these nuclei, however production rates are often extremely low.

The PTMS techniques currently used for rare isotope measurements are destructive techniques, meaning that the ions being measured are lost during the measurement process. As a

result, ions must be continuously re-loaded into the Penning trap. A complete mass determination requires a minimum of ~ 100 detected ions with such destructive techniques (details on PTMS techniques are presented in Chapter 2). For extremely exotic isotopes far from stability, where production rates may be \sim a few per day or less, it is therefore impossible to use a destructive technique to complete a Penning trap mass measurement simply because the time required to detect ~ 100 ions far exceeds the time available for typical online beam experiment (typically a week or two).

A different, non-destructive PTMS technique known as narrowband Fourier Transform Ion Cyclotron Resonance (FT-ICR) has been used for extremely high-precision mass measurements of stable ions with single-ion sensitivity. In an effort to extend this technique to short-lived radioisotopes far from stability, a new Penning trap known as the Single Ion Penning Trap (SIPT) has recently been developed at LEBIT. The design and offline commissioning of SIPT are presented in detail in Chapter 5. Using the non-destructive narrowband FT-ICR technique, SIPT will allow complete mass determinations with a single trapped ion, thereby extending LEBIT's reach to the far limits of the nuclear chart where production rates are extremely low.

In general, short half-lives present an additional difficulty for measuring nuclei far from stability. SIPT is expected to require half-lives similar to those currently measurable at LEBIT (\sim tens of ms or longer). However, the additional stability offered by shell closures means that isotopes in the vicinity of magic or doubly-magic nuclei often have surprisingly long half-lives, even far from stability. These are the regions of most interest for study with SIPT.

For example, the doubly-magic nuclei ^{78}Ni and ^{100}Sn are often considered “holy grails” for nuclear structure studies far from stability. With 28 protons and 50 neutrons, ^{78}Ni is

the most neutron-rich doubly-magic nucleus. On the opposite side of the valley of stability, ^{100}Sn has 50 protons and 50 neutrons and is the heaviest $N = Z$ nucleus. These nuclei and those in their vicinity therefore provide valuable insight into the role of magic numbers far from stability. With half-lives of 122 ms and 1.16 s respectively, ^{78}Ni and ^{100}Sn both live long enough for Penning trap mass measurements. However, current production rates for these two nuclei are only \sim a few per day at the NSCL, so destructive PTMS techniques are not an option for measuring these nuclei. Non-destructive measurements with SIPT will provide a path towards precise mass measurements of these highly-exotic nuclei, allowing careful studies of nuclear binding energy trends far from stability.

A discussion of PTMS, including detailed descriptions of TOF-ICR and FT-ICR detection, is presented in Chapter 2. Chapter 3 describes the LEBIT facility at the NSCL. The precision mass measurements of cobalt isotopes beyond $N = 40$, introduced at the end of Section 1.1, are presented in detail in Chapter 4. Finally, the development and the first commissioning tests of SIPT are discussed in Chapter 5.

Chapter 2

Penning Trap Mass Spectrometry

2.1 Penning Trap Basic Concepts

2.1.1 Trapping Fields

A Penning trap is an ion storage device which uses a combination of a uniform magnetic field and a quadrupolar electrostatic field to capture a charged particle in three dimensions. The magnetic field provides radial confinement, as charged particles in a magnetic field are bound to orbit about the magnetic field lines at the cyclotron frequency

$$\omega_c = 2\pi\nu_c = \frac{qB}{m} \quad (2.1)$$

which depends only on the ions' charge q , mass m , and the magnetic field strength B . A magnetic field alone does not trap ions in the direction along the field axis, so to obtain three-dimensional confinement an electrostatic potential is superposed. At LEBIT, this is accomplished using a system of three hyperbolic trapping electrodes: two endcaps and a ring, as shown in Fig. 2.1. These three electrodes are hyperboloids of revolution defined by

$$z^2 - \rho^2 = \pm z_0^2 \quad (2.2)$$

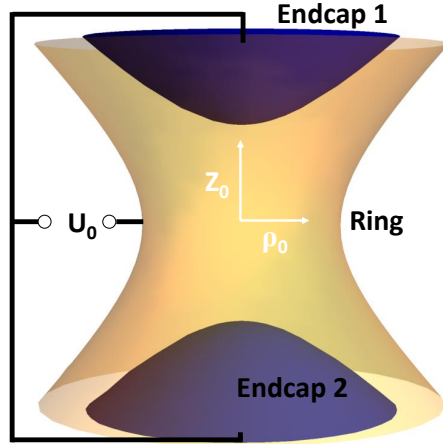


Figure 2.1: Three hyperbolic trap electrodes (two end cap electrodes and one ring electrode) used to create the quadrupolar electrostatic field necessary for axial ion confinement.

and create an electrostatic quadrupole potential which can be given in cylindrical coordinates (ρ, z) by

$$V(\rho, z) = \frac{U_0}{4d^2}(2z^2 - \rho^2), \quad (2.3)$$

where U_0 is the potential difference between the endcap and ring electrodes, and d is a characteristic trap parameter defined as $d = \sqrt{\rho_0^2/4 + z_0^2/2}$. The quantities z_0 and ρ_0 refer to half of the minimum distance between end cap electrodes and the minimum radius of the ring electrode, respectively, as shown in Fig. 2.1. Other Penning trap electrode geometries, such as cylindrical traps, can be used to sufficiently approximate a quadrupolar electric field [36], however such geometries introduce higher-order electric field contributions which must be compensated to minimize uncertainties from frequency shifts if the trap is to be used for high-precision frequency measurements [37].

2.1.2 Ion Motion in a Penning Trap

A derivation of the motion of a charged particle in a Penning trap can be found in Ref. [38], and the relevant results are summarized here. The addition of a quadrupolar electrostatic

field to a uniform magnetic field results in three distinct eigenmotions. In the z -direction, defined as the direction of the uniform magnetic field \vec{B} , ions will undergo simple harmonic motion at the frequency

$$\omega_z = 2\pi\nu_z = \sqrt{\frac{qU_0}{md^2}}. \quad (2.4)$$

In the radial plane, the presence of the quadrupolar electrostatic field \vec{E} splits the true cyclotron motion at frequency ω_c into two distinct radial motions: a slow $\vec{E} \times \vec{B}$ drift known as the magnetron motion at frequency ω_- and a much faster modified cyclotron motion at frequency ω_+ , with the radial frequencies defined as

$$\omega_{\pm} = 2\pi\nu_{\pm} = \frac{\omega_c}{2} \pm \sqrt{\frac{\omega_c^2}{4} - \frac{\omega_z^2}{2}}. \quad (2.5)$$

An illustration of these three eigenmotions is presented in Fig. 2.2. The true cyclotron frequency is simply the sum of the two radial frequencies

$$\omega_c = \omega_+ + \omega_- \quad (2.6)$$

and the three eigenfrequencies are related to the cyclotron frequency by

$$\omega_c = \sqrt{\omega_+^2 + \omega_-^2 + \omega_z^2}. \quad (2.7)$$

In fact, Eq. (2.6) as derived in Ref. [38] only holds true for a perfect Penning trap. The non-trivial demonstration that this relation can still be used for high-precision measurements in a real Penning trap without introducing additional systematic uncertainties can be found in Ref. [39].

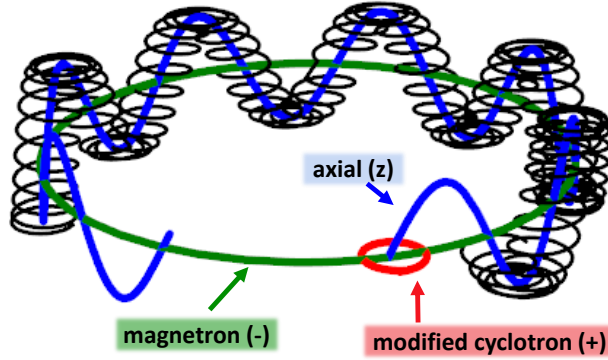


Figure 2.2: Illustration of the motion of a charged particle in a Penning trap. This motion is a combination of three distinct eigenmotions: the magnetron motion (green) at frequency ω_- , the modified cyclotron motion (red) at frequency ω_+ , and the axial oscillations (blue) at frequency ω_z . The black path illustrates the combination of these three motions.

In a typical Penning trap environment with a strong magnetic field ($\sim T$) and a relatively weak electric field ($\sim V/mm$), $\omega_+ \gg \omega_z \gg \omega_-$.

2.1.3 Manipulation of Ion Motion with RF Electric Fields

Once confined in a Penning trap, ions' motion can be manipulated in various ways using multipolar RF electric fields [40]. At LEBIT, these RF fields are applied to the ring electrode, which is segmented into eight equal parts to allow for dipole, quadrupole, or octupole excitations [41], though currently only dipole and quadrupole excitations are regularly employed.

An illustration of the dipole and quadrupole RF configurations is presented in Fig. 2.3. In the dipole configuration, the applied RF field is 180° out of phase between opposite halves of the ring electrode. Dipole excitations applied to the ring electrode can drive either of the two radial motions when applied at their respective frequencies, increasing the radius ρ_+ or ρ_- of the selected motion. Unlike the magnetron frequency, which is weakly mass-dependent,

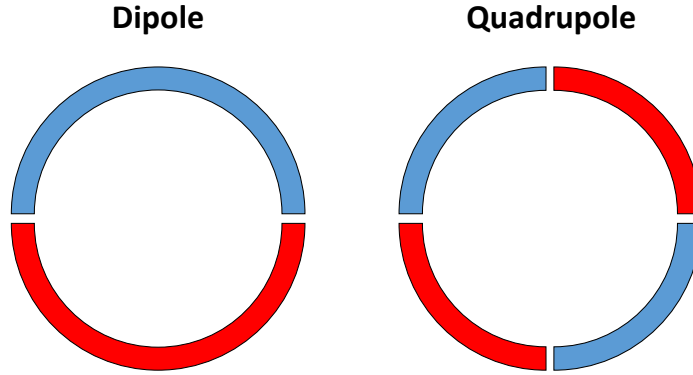


Figure 2.3: Applied RF geometries used to obtain dipole (left) and quadrupole (right) excitations of the ions' motion in the Penning trap. At LEBIT, the ring electrode is segmented to achieve these geometries. Red and blue segments represent RF applications of equal frequency and amplitude, 180° out of phase.

the modified cyclotron frequency is strongly mass-dependent, and dipole excitation at the modified cyclotron frequency is therefore commonly used at LEBIT to remove unwanted ion species from the Penning trap by driving their modified cyclotron motion to a large radius where the ions are lost from the trap. Unknown contaminants in the Penning trap are also identified in this manner by scanning the applied dipole RF frequency and looking for a reduction in the number of ions extracted from the trap.

In the quadrupole RF configuration, the applied RF field is the same on opposite quarters of the ring segment and adjacent quarters are 180° out of phase, as shown in Fig. 2.3. This configuration is used to couple the trapped ions' two radial motions. When a quadrupole RF drive is applied at the true cyclotron frequency $\nu_c = \nu_+ + \nu_-$, a periodic beating occurs between the magnetron and modified cyclotron motions, as demonstrated in Fig. 2.4. Because $\nu_+ \gg \nu_-$, a substantial change in the ions' radial energy occurs during the conversion between radial motions. This change in energy is then detected in a manner discussed in Section 2.3 and used to measure the true cyclotron frequency ν_c of the trapped ions, which

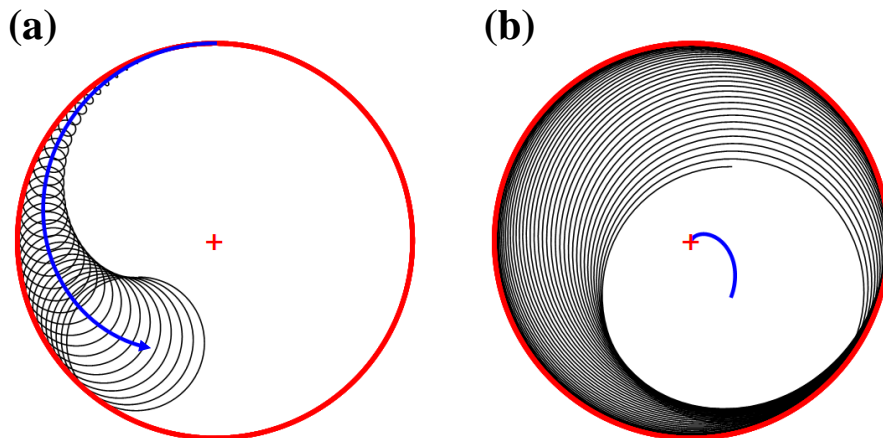


Figure 2.4: Conversion between the two radial modes of an ion's motion in a Penning trap. (a) The ion begins with pure magnetron motion (red circle). When a quadrupole RF drive is applied at the true cyclotron frequency ν_c , the modified cyclotron radius grows as seen by the growing black circles, and the magnetron radius decreases as indicated by the blue arrow. (b) When full conversion of magnetron to modified cyclotron motion is complete, the modified cyclotron radius is equal to the initial magnetron radius.

is then used to determine the ions' mass according to Eq. (2.1).

2.2 Overview of Penning Trap Mass Spectrometry

Penning traps provide an excellent environment for precision studies of charged particles, offering confinement in a small volume, well-controlled electromagnetic fields, and the ability to manipulate particles' motion as described in the previous section. While several areas of active research make use of Penning traps for these reasons, the application of particular interest for this thesis is the use of Penning traps to perform precise mass measurements of charged particles. Two different methods of Penning Trap Mass Spectrometry (PTMS) are now well established and widely used: Time-of-Flight Ion Cyclotron Resonance (TOF-ICR) [40] and Fourier Transform Ion Cyclotron Resonance (FT-ICR) [42] detection. Both

of these methods are now employed at LEBIT. They are discussed in detail in the next two sections and are compared at a high level in this section. A third PTMS technique known as Phase Imaging Ion Cyclotron Resonance (PI-ICR) was pioneered by the SHIP-TRAP experiment at GSI in recent years [43]. Several other mass measurement experiments, including LEBIT, have now taken steps towards incorporating PI-ICR detection as well. A brief discussion of PI-ICR detection is included at the end of this section.

TOF-ICR detection is currently the primary technique used for Penning trap mass measurements of rare isotopes. It is a destructive measurement technique, meaning that ions must be ejected from the trap for detection and new ions loaded into the trap repeatedly to complete a single mass determination, as described in the next section. The mass precision of a TOF-ICR measurement is given approximately by

$$\frac{\delta m}{m} \approx \frac{\gamma}{\nu_c T_{\text{RF}} \sqrt{N}} \quad (2.8)$$

[40], where $\nu_c = qB/2\pi m$ is the cyclotron frequency of an ion with mass-to-charge ratio m/q in a Penning trap with magnetic field strength B , T_{RF} is the measurement time of ions in the Penning trap, N is the total number of ions detected, and γ is a unitless parameter dependent on the particular experimental setup. At LEBIT, the value of γ is ≈ 0.3 [44]. Assuming that radioactive ions can be observed for about one half-life, this means that ions with half-lives on the order of tens of milliseconds can be measured to precisions required for nuclear structure or astrophysics studies (see discussion in Section 1.1) in the timespan of a typical online beam experiment. For example, a singly-charged species of mass 50 u with a half-life of 50 ms could be measured in the LEBIT 9.4-T Penning trap to an expected precision of $\sim 2 \times 10^{-7}$ with only 1000 detected ions. It follows from Eq. (2.8) that even

higher precisions can be reached for longer-lived species. For instance, ^{14}O ($T_{1/2} = 71$ s) was measured at LEBIT to a mass precision of $\sim 2 \times 10^{-9}$ [28]. This measurement used a 250-ms measurement time, and also employed a Ramsey excitation scheme for an additional improvement in precision [45].

TOF-ICR detection also offers the advantage of high versatility. Measuring different ions over a wide mass range requires only a few parameter changes which can be implemented quickly. No major changes in the LEBIT setup are required between measurements, leaving a large amount of flexibility in preparation and scheduling for beam time.

FT-ICR detection is used for a wide variety of PTMS experiments. Broadband FT-ICR detection is widely used in analytical chemistry because it allows for simultaneous identification of numerous species held in the Penning trap. While broadband FT-ICR detection provides excellent resolution for species identification ($\delta m/m \sim 10^{-6}$), high-precision mass measurements for fundamental studies require much higher precision. This is accomplished using narrowband FT-ICR detection, which uses a resonating detection circuit that is tuned to resonate near the frequency of the particular species being measured. Details of this detection technique are discussed in Section 2.4.

As in TOF-ICR detection, the mass precision achievable with FT-ICR detection is inversely related to the observation time. The masses of stable charged particles can therefore be measured to extremely high precisions by observing their motion in the trap for very long time periods. Narrowband FT-ICR detection has been used in this manner for some of the most precise determinations of fundamental physical properties [2,27], including particle/anti-particle symmetries for tests of the CPT theorem [46–48] and electron g-factors for tests of QED and determination of fundamental constants [48,49], reaching fractional precisions below 10^{-10} .

The primary distinction of FT-ICR detection is that it is a non-destructive technique, meaning that ions are not lost during the detection process. The non-destructive nature of FT-ICR detection is central to the SIPT project introduced in Chapter 1 and discussed in detail in Chapter 5, as this will enable complete mass determinations with a single detected ion. SIPT will be used for radioactive ion measurements, limiting the observation time and therefore the precision. However, as shown in Section 5.1, precisions comparable to those obtained with TOF-ICR detection are expected with a well-designed detection circuit. This comes in exchange for the versatility offered by TOF-ICR detection, however, as a given resonator circuit will only be usable over a small mass range.

PI-ICR detection uses a position-sensitive microchannel plate (MCP) detector. Ions ejected from the Penning trap at different points along their orbit will therefore show up at different locations on the position-sensitive detector. By varying the time for which ions are held in the trap and then tracking the change in location on the MCP, the frequency of the ions' motion can be determined from the accumulated phase. In contrast to the TOF-ICR technique, the resolution of a PI-ICR measurement therefore depends not only on the measurement time but also on the resolution of the phase imaging. This inclusion of phase information has been shown to allow a factor of 40 improvement in mass resolution over TOF-ICR detection [43]. At LEBIT, a position-sensitive MCP has been purchased and first steps have been made to adapt the ion ejection optics to allow for commissioning of PI-ICR detection.

2.3 TOF-ICR Technique

TOF-ICR detection is a technique for measuring the cyclotron frequency of charged particles in a Penning trap by detecting the energy gained when magnetron motion is converted into modified cyclotron motion. As discussed in Section 2.1.3, this conversion can be achieved by applying a quadrupolar RF field at a frequency ν_{RF} that matches the trapped ions' true cyclotron frequency ν_c .

Because $\omega_+ \gg \omega_-$, maximum energy gain is achieved with a full conversion from pure magnetron motion to pure modified cyclotron motion. To prepare the ions in an initial state of magnetron motion, LEBIT pioneered the use of a Lorentz steerer [50], which uses a transverse electric field immediately before injection into the Penning trap in conjunction with the 9.4-T magnetic field to create an $\vec{E} \times \vec{B}$ force, steering the ions slightly off of the central beam axis as they enter the Penning trap. Before a measurement, the electric field of the Lorentz steerer is scanned to determine how far off-axis the ions can be driven without reducing efficiency. The further off-axis the ions are injected, the larger their initial magnetron radius ρ and thus the greater the radial energy gain when the magnetron motion is converted to modified cyclotron motion. This can be seen simply from the difference in rotational kinetic energy

$$\Delta E_r = \frac{1}{2}m(\omega_+^2 - \omega_-^2)\rho^2. \quad (2.9)$$

Complete conversion from magnetron to modified cyclotron motion using a quadrupolar RF excitation requires the proper product of RF duration and amplitude, known as a π -pulse [40]. At LEBIT, the amplitude required for a π -pulse at a given RF duration has been calibrated by scanning the RF amplitude for a particular RF duration to find the maximum kinetic energy gain. This calibration is stored in the control system, so the user

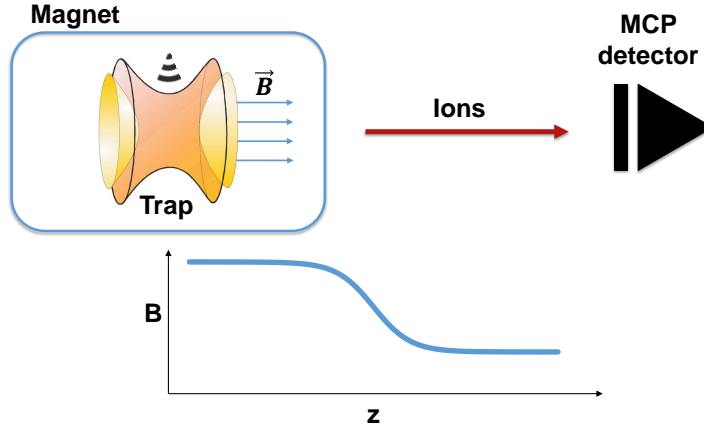


Figure 2.5: Ions ejected from the Penning trap move through an axial magnetic field gradient as they travel to the MCP detector. This results in an axial kick proportional to the ions' radial energy, as demonstrated by Eq. (2.10).

can now set the desired RF duration (based on considerations such as ion half-life and desired precision), and the control system uses the stored calibration to automatically calculate the RF amplitude needed for a π -pulse.

To detect the change in radial energy, ions are ejected from the Penning trap and travel to an MCP detector just outside of the magnetic field. As shown in Fig. 2.5, ions moving from the strong magnetic field at the center of the magnet to the MCP outside the magnet will encounter a negative magnetic field gradient in the axial direction. A charged particle orbiting in the radial plane will therefore experience a force in the axial direction given by

$$F_z = -\mu \left(\frac{\partial B}{\partial z} \right) = -\frac{E_r}{B_0} \left(\frac{\partial B}{\partial z} \right), \quad (2.10)$$

where μ is the dipole moment of the orbiting charged particle with radial energy E_r in a central magnetic field strength B_0 [2]. This axial force causes ions with more radial energy to reach the MCP in less time, so the gain in radial energy is ultimately detected as a reduction in time of flight from the Penning trap to the MCP.

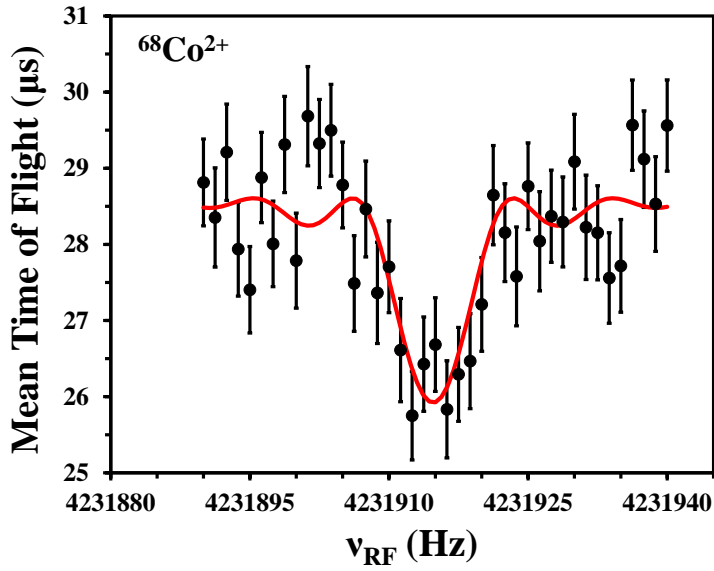


Figure 2.6: Example of a TOF-ICR resonance obtained by scanning the applied RF quadrupole excitation frequency and measuring the ions’ time of flight to an MCP detector. The red curve is a theoretical fit, the center of which corresponds the cyclotron frequency ν_c .

To determine the cyclotron frequency of a charged particle in a Penning trap, the frequency ν_{RF} of the applied quadrupole RF electric field is scanned around the ions’ expected cyclotron frequency ν_c . After each RF excitation is applied, ions are ejected from the Penning trap and the time of flight to the MCP is measured. Then another ion or small bunch of ions is injected into the trap and the next ν_{RF} step is applied. When $\nu_{\text{RF}} = \nu_c$, the initial magnetron motion will be converted to modified cyclotron motion, and this gain in energy will be detected as a reduction in the time of flight. Plotting time of flight as a function of the applied ν_{RF} then reveals a substantial dip at ν_c , which is fit with a theoretical line shape [40] to determine the center. An example of such a resonance plot is shown in Fig 2.6.

As seen in Eq. (2.1), the cyclotron frequency depends only on the ions’ mass, charge state, and the strength of the magnetic field. The charge state of the ions is known prior to trapping, however the magnetic field at LEBIT is known to decay over time at a rate of ~ 10

ppb/hr. To monitor the strength of the magnetic field at a high level of precision, each ion of interest measurement is immediately preceded and followed by measurements of a reference ion with a well-known mass. The reference ion frequencies are then linearly interpolated to determine the cyclotron frequency $\nu_{c,\text{ref}}$ of the reference ion at the time the ion of interest was measured. The magnetic field strength then cancels out when taking the ratio of the reference ion and ion of interest frequencies, and the mass of the ion of interest is determined from this ratio as

$$m = m_{\text{ref}} \left(\frac{\nu_{c,\text{ref}}}{\nu_c} \right) \left(\frac{q}{q_{\text{ref}}} \right). \quad (2.11)$$

Note that the masses in Eq. (2.12) refer to the masses of the measured ions; to determine the atomic mass of the ion of interest, the mass of missing electrons must be accounted for. In very high-precision measurements, the electron binding energies must also be accounted for, though these are typically only ~ 10 eV and can therefore often be neglected.

2.4 FT-ICR Technique

The FT-ICR technique relies on picking up the image current created when ions oscillate inside a Penning trap, generating some time-varying image charge on the trap electrodes [42]. While the time-domain signal generated in this manner may look quite complicated, particularly if multiple ion species are present or if there is a substantial amount of noise, this signal can be converted to a frequency-domain spectrum via Fast Fourier Transform (FFT) [51]. In the frequency domain, the detected ion frequencies will be plainly visible as distinct peaks, which can be fit to determine the frequency of the ions' motion.

For precision measurements, the number of ions in the trap typically must be limited to a few at a time or less in order to avoid systematic frequency shifts from ion interactions [52].

Also, while it is desirable to excite the ions' motion to large radii to increase the image charge detected on the trap electrodes, ions become more sensitive to field imperfections as they get closer to the trap electrodes, which will lead to frequency shifts as well and therefore limits how close the ions can get to the electrodes [2, 38, 53]. This means that precision measurements with FT-ICR detection require a high degree of sensitivity so that the image charge from very few (or even single) ions can be detected.

The needed gain in sensitivity for precision measurements is accomplished using what is known as narrowband FT-ICR detection [2]. The principle of narrowband FT-ICR detection is illustrated in Fig. 2.7. The Penning trap electrodes used for image current pickup are connected in parallel with an inductor of inductance L to create an RLC resonator circuit, where the resistance R is the effective parallel resistance of the circuit and the capacitance C is a combination of the capacitance between the pickup electrodes and other parasitic capacitances from the wires, amplifier, etc. This RLC circuit will resonate at a frequency

$$\nu_{circ} = \frac{1}{2\pi\sqrt{LC}}, \quad (2.12)$$

so by choosing proper values of L and C the circuit can be tuned so that ν_{circ} is approximately equal to the frequency of the ions' motion to be detected. This tuned resonance circuit will enhance the ion signal, which is then further amplified and processed with an FFT algorithm for analysis.

The detected ion motion depends on the multipolar configuration of the pickup electrodes in the same way as the driven ion motions described in Section 2.1.3. Dipole pickup, which is to say, differential image current pickup between opposite halves of the ring electrode, is shown in Fig. 2.7 and is used to detect the magnetron and modified cyclotron motions.

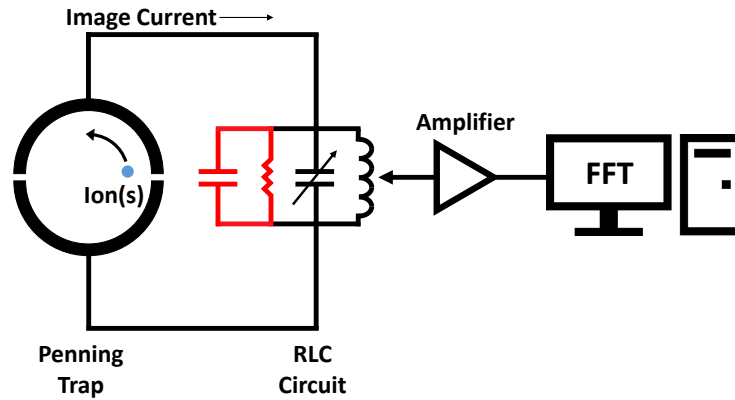


Figure 2.7: Schematic illustration of narrowband FT-ICR detection.

Quadrupole pickup between adjacent quarters of the ring electrode is used to detect the sum frequency $\nu_c = \nu_+ + \nu_-$ when the ions' motion is a mixed state of modified cyclotron and magnetron motions. In realistic cases, such pure multipole configurations are often only approximated, for instance if some ring segment electrodes are needed to drive the ions' motion rather than for image current pickup or if an imperfect trap geometry is used. This means that the total image current signal may be divided between multiple frequency peaks including components from different multipolarities. An example of a single frequency spectrum including peaks at ν_+ and ν_c is presented with the discussion in Appendix A on characterizing the MiniTrap magnetometer developed at LEBIT.

Chapter 3

The LEBIT Mass Spectrometer

Facility at the NSCL

The National Superconducting Cyclotron Laboratory (NSCL) is a world-class facility for rare isotope research located on the campus of Michigan State University (MSU). Rare isotope beams at the NSCL are produced by projectile fragmentation. Naturally abundant heavy ion primary beams are accelerated by two coupled superconducting cyclotrons to energies on the order of 100 MeV per nucleon. These fast primary beams are then impinged on a light, thin ^9Be target. Protons and neutrons are knocked off of the primary beam nuclei in the resulting nuclear collisions, producing a cocktail beam containing a variety of different nuclides. The desired rare isotope species is then selected in-flight using the A1900 fragment separator [54], which uses a system of magnets and degraders to filter out the unwanted species.

The projectile fragmentation method has a few important advantages compared to other rare isotope production methods. One such advantage is that this is a universal technique, equally applicable across the nuclear chart. Another advantage of projectile fragmentation is that it is a very fast process. Because a fast, heavy primary beam is used with a light, thin production target, the reaction products retain nearly all of their initial forward momentum. Beam purification is then performed in-flight, and as a result rare isotopes can be delivered

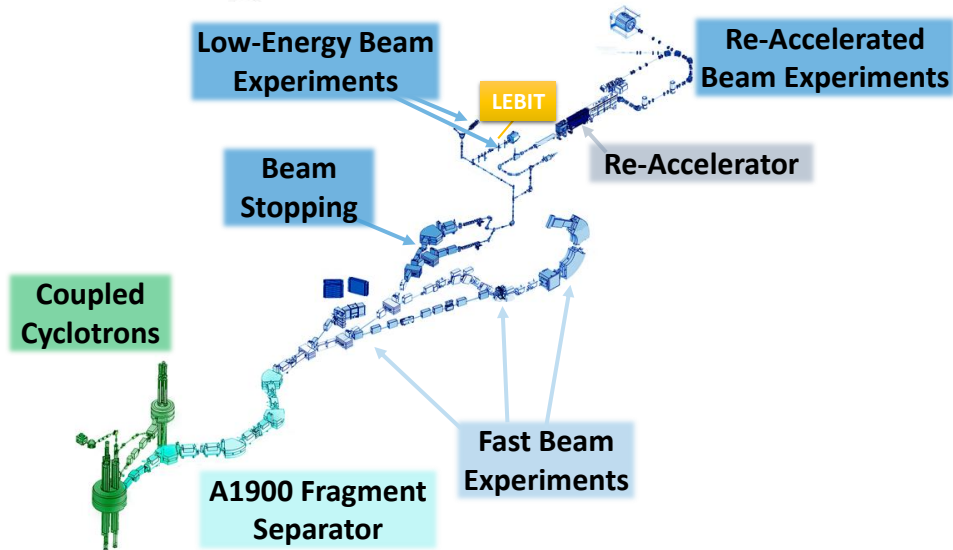


Figure 3.1: Layout of the NSCL. Rare isotope beams from the A1900 are delivered either directly to fast beam experiments or to the beam stopping facility, from which stopped beams are sent to low-energy experiments including LEBIT or to the re-accelerator facility for intermediate energy experiments. (Adapted from <http://nscl.msu.edu/public/virtual-tour.html>.)

to experimental areas promptly from the time they are produced.

Fast beams are excellent for studies of very short-lived nuclei or for many reaction studies, however they are not ideal for all experiments. Precision measurements such as collinear laser spectroscopy at BECOLA [55] or Penning trap mass measurements at LEBIT require stopped beams, and many reaction studies relevant for nuclear astrophysics or structure require rare isotope beams at low or intermediate energies. These energy regimes are also available at the NSCL thanks to the beam stopping facility described in the next section, which slows the fast beams delivered from the A1900 to thermal energies. These stopped beams can then either be delivered to the low-energy area including LEBIT and BECOLA or to the re-accelerator facility ReA3 [56], which accelerates beams to intermediate energies. The layout of the NSCL, including fast beam, stopped beam, and re-accelerated beam experiments, is presented in Fig. 3.1.

The next-generation upgrade for rare isotope production at MSU, known as the Facility for Rare Isotope Beams (FRIB), is now well on its way to completion. FRIB will provide an enormous gain in beam power, increasing production rates across the nuclear chart and allowing access to a large number of rare isotopes far from stability that are currently unavailable anywhere else in the world. This will present the opportunity for groundbreaking new rare isotope research and new discoveries. The current experimental areas at the NSCL, including LEBIT, will remain in use when FRIB comes online, simply taking beam from the new FRIB accelerator rather than from the current cyclotron facility. Thus all of the past and current developments that have made LEBIT a world-class facility for precise, accurate mass measurements of rare isotopes will make LEBIT well-prepared to take full advantage of the new scientific opportunities presented by FRIB.

3.1 Beam Stopping at the NSCL

In order to perform Penning trap mass measurements of rare isotopes from projectile fragmentation, the fast rare isotope beams delivered from the A1900 must first be stopped so that the ions can be captured in the Penning trap. Most of the beam energy is initially lost by sending the beam through a system of solid degraders. The remaining energy is lost through collisions with neutral helium atoms in a helium-filled gas chamber developed at Argonne National Laboratory (ANL) and commissioned at the NSCL in 2014 [57]. A picture of the ANL gas cell is presented in Fig. 3.2. Radiofrequency electric fields are used to repel ions from the walls of the gas chamber, and a combination of DC electric fields and gas flow are used to transport the ions through the gas cell. The low-energy rare isotope beam is then extracted through a radiofrequency quadrupole (RFQ) ion guide and delivered either

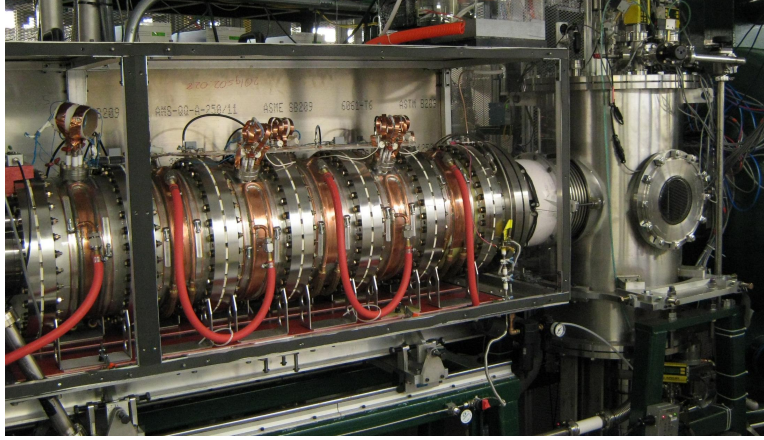


Figure 3.2: Photo of the ANL gas cell used for beam stopping at the NSCL.

to low-energy experiments such as LEBIT or to ReA3 for intermediate-energy experiments.

Two major projects are currently underway to expand beam stopping capabilities at the NSCL. The Advanced Cryogenic Gas Stopper (ACGS) will operate at cryogenic temperatures of ~ 40 K in order to freeze out much of the stable contamination present in the gas cell. This will provide much purer low-energy beams, alleviating much of the current difficulty associated with chemistry in the gas cell as discussed in Section 4.2.1. The ACGS is also designed to optimize efficiency even with very high incoming rates, in preparation for the high beam rates expected when FRIB comes online. ACGS is currently being commissioned and is expected to be operational for online beam experiments in the near future.

The other major beam stopping project currently underway at the NSCL is the cyclotron gas stopper [58]. The cyclotron gas stopper also operates at cryogenic temperatures, but unlike the ACGS, ions in the cyclotron gas stopper move along a circular trajectory, spiraling inwards as they lose energy via collisions with neutral helium atoms. This spiral path provides an extended stopping distance, which will be especially useful for efficiently stopping light ion species. The cyclotron gas stopper will be installed in the NSCL beamline parallel to the ACGS so that either device may be used depending on which would be optimal for a

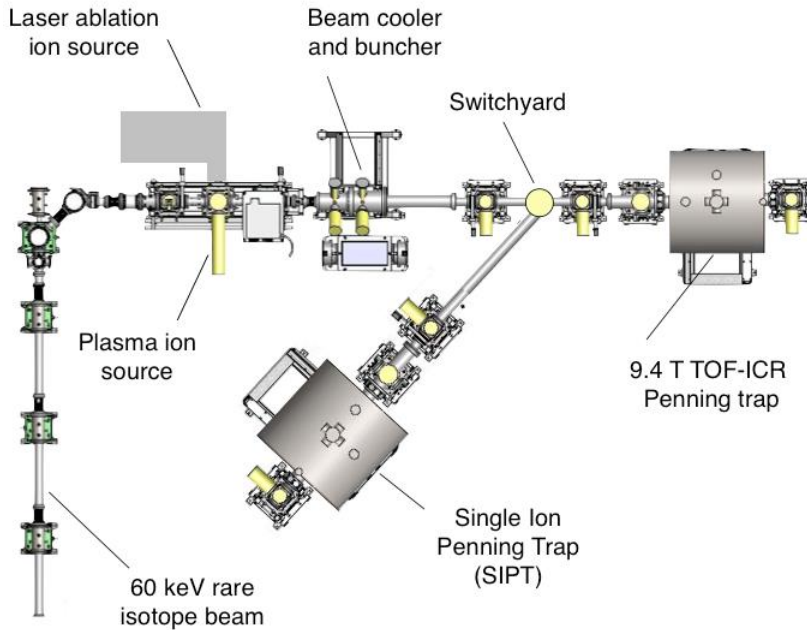


Figure 3.3: Layout of the LEBIT facility. The functions of each major component are described in the text. (Reproduced from <https://groups.nsl.msu.edu/lebit/lebitfacility/index.html>.)

given experiment.

3.2 Major Components of the LEBIT Facility

A schematic overview of the LEBIT facility is presented in Fig. 3.3. Ions are delivered from the beam stopping facility or from either of two offline ion sources. A 90° electrostatic bender is used to direct ions from the desired source to the LEBIT cooler/buncher, which prepares short, low-emittance ion bunches for delivery to one of the Penning traps. Ion bunches are then either sent to the 9.4-T Penning trap for TOF-ICR measurements or to the 7-T Single Ion Penning Trap currently being commissioned for ultra-high sensitivity FT-ICR measurements. Each of the major components is discussed in detail in the following subsections.

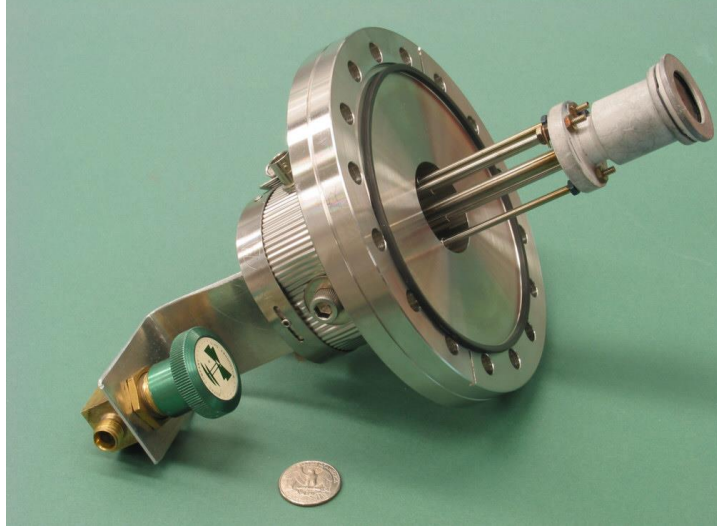


Figure 3.4: Photo of the Colutron ion source which produces stable and long-lived ions via plasma or surface ionization.

3.2.1 Offline Ion Sources

LEBIT has two offline ion sources: a Colutron plasma ion source and a laser ablation source (LAS) [59]. These sources provide stable or very long-lived ions to LEIBIT when rare-isotope beam is not being delivered from the gas stopping facility. In addition to being extremely valuable for system diagnostics and calibrations, these offline sources have also now been used for a number of high-precision offline measurements of scientific importance [60–67].

A picture of the Colutron ion source is presented in Fig. 3.4. A tungsten filament is heated to produce electrons and is negatively biased to spark a discharge, ionizing gas atoms of the desired species which are introduced to the chamber with a leak valve. The filament can also be positively biased to provide alkali metal ions via surface ionization from impurities in the filament.

A picture of the LAS is presented in Fig. 3.5. The laser ablation source uses a pulsed Nd:YAG Quantel Brilliant laser to produce 4 ns light pulses, which are then guided to a solid target of the desired source material. The laser irradiation results in the emission of

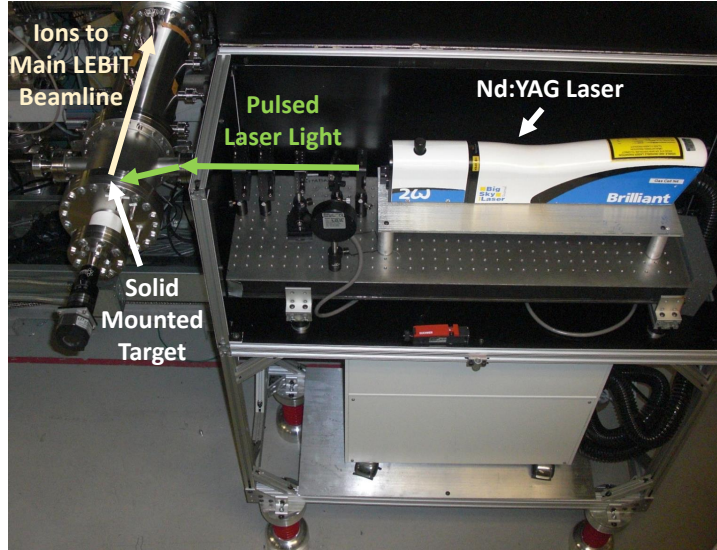


Figure 3.5: Photo of the laser ablation ion source at LEBIT.

positive ions from the surface of the target, which are then electrostatically transported to the main LEBIT beamline.

3.2.2 Cooler/buncher and Fast Electrostatic Kicker

The LEBIT cooler/buncher is a 3-stage linear Paul trap used for final beam preparation before delivery to the Penning trap. Details can be found in [68], and a picture is presented in Fig. 3.6. In all three stages, radiofrequency quadrupole (RFQ) electric fields are used to confine ions in the transverse directions, and a buffer gas (typically helium) is used to cool the ions to thermal equilibrium with the gas. Some amount of a heavier gas, such as neon, is sometimes introduced through a separate leak valve to promote collision-induced dissociation of molecules to improve beam purity [69]. The first stage, the pre-cooler, has the highest buffer gas pressure (~ 0.03 mbar) for fast ion cooling and uses an axial DC field to guide ions through. The second stage is referred to as the micro-RFQ and acts as a barrier between the first and third stages to allow differential pumping. This is a small-scale version

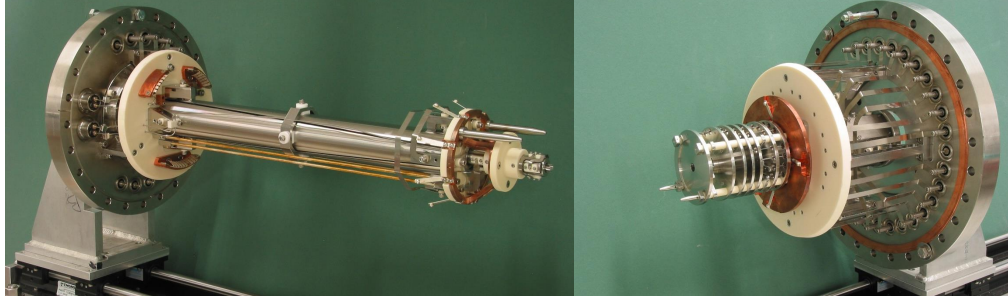


Figure 3.6: Photos of the LEBIT cooler/buncher used to prepare cooled ion bunches for delivery to the Penning trap. The pre-cooler and micro-RFQ are shown on the left, and the buncher stage is shown on the right.

of the pre-cooler and also uses an axial DC field to guide ions through to the next stage. The final stage is the buncher stage. In the buncher stage, a series of electrodes is used to shape the axial potential into a potential well to trap the ions. The continuous incoming beam is collected in the buncher for a set amount of time, and then the confining potential is switched to eject the collected ions in a short, sub- μs pulse. In this manner, the LEBIT cooler/buncher provides short, low-emittance ion bunches to the Penning trap for capture and measurement.

Between the cooler/buncher and the Penning trap, a fast-switching electrostatic kicker is used to separate ions of different masses by their time of flight. Ions are ejected from the cooler/buncher with the same kinetic energy $E_{kin} = \frac{1}{2}mv^2$, so heavier ions will travel at slower speeds and thus will reach a given location at a later time than lighter ions. The kicker is generally held at a high potential to prevent ions from reaching the Penning trap. When ions of the desired mass reach the kicker, the potential is switched for a short period of time to allow these ions to pass, then switches back to high potential. The fast electrostatic kicker has a resolving power $\frac{m}{\Delta m} > 400$, which is sufficient to prevent non-isobaric contaminants from reaching the Penning trap.

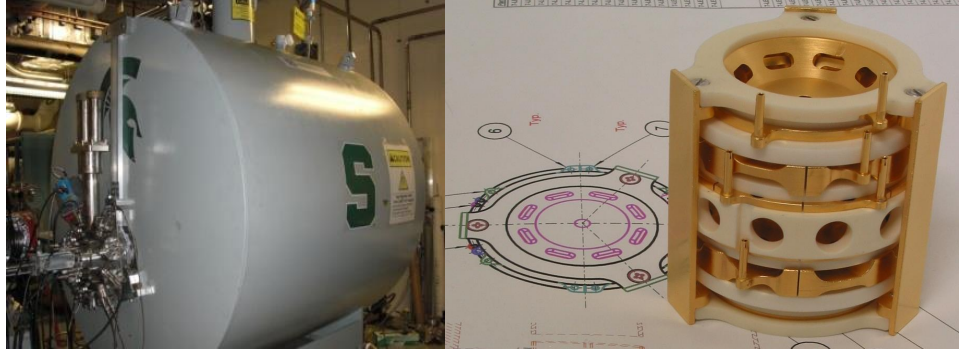


Figure 3.7: The 9.4-T superconducting magnet (left) and hyperbolic Penning trap electrode structure (right) used for TOF-ICR measurements at LEBIT.

3.2.3 TOF-ICR Penning Trap

TOF-ICR mass measurements, discussed in detail in Section 2.3, are carried out in the LEBIT Penning trap, which is housed in a 9.4-T superconducting magnet. Pictures of the TOF-ICR Penning trap electrodes and magnet are presented in Fig. 3.7. A series of drift tubes used for ion injection and ejection are mounted on either side of the Penning trap and sit inside the magnet bore. One of the final injection drift tubes is segmented to form a Lorentz steerer to prepare the ion in an initial state of magnetron motion, as described in Section 2.3.

The LEBIT Penning trap uses a hyperbolic electrode geometry with additional compensation electrodes for ideal approximation of a true quadrupolar electrostatic potential [41]. These compensation electrodes minimize frequency shifts due to the fact that the hyperbolic electrodes are finite in size and that holes in the end cap electrodes are required to allow the ions to enter and exit the Penning trap. The copper trap electrodes are plated with gold to minimize patch effects due to oxidation.

An MCP detector is mounted in a Daly configuration [70] outside the 9.4-T magnet. Ions are guided towards a collector plate and create a cascade of electrons which are then

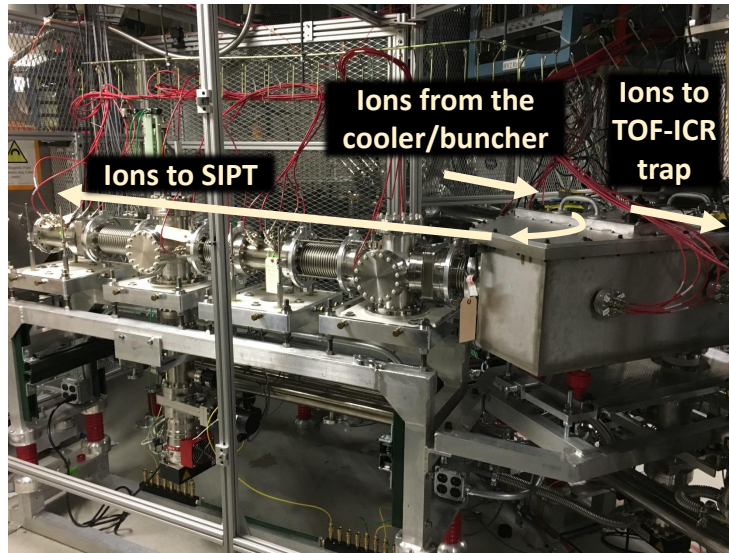


Figure 3.8: Photo of the recently-commissioned SIPT beamline, used for ion transfer from the cooler/buncher to the 7-T SIPT magnet for FT-ICR measurements. Details on individual components of this beamline are presented in Section 5.2

detected on the MCP. A position-sensitive MCP was also recently installed downstream of the Daly configuration to begin testing of PI-ICR detection discussed in Section 2.2.

3.2.4 SIPT

A picture of the recently-added SIPT beamline is presented in Fig. 3.8. This branch of the LEBIT beamline is located after the cooler/buncher so that rare isotopes from the beam stopping facility or stable ions from either of the two offline ion sources can be used with SIPT. Cooled and bunched ions from any of these sources are then directed to either the 9.4-T Penning trap for TOF-ICR measurements or the 7-T SIPT Penning trap for high-sensitivity FT-ICR measurements. The design and commissioning of SIPT are discussed in detail in Chapter 5.

Chapter 4

Mass Measurements of Neutron-Rich Cobalt Isotopes Beyond $N=40$

The results presented in this chapter were recently published in Physical Review C [71]. Portions of the text in this chapter and several of the figures presented here are reproduced from this reference. Additional details and discussion are included here as well.

4.1 Motivation for Mass Measurements of $^{68,69}\text{Co}$

4.1.1 Evidence for a Subshell Closure at $N = 40$

The region of the nuclear chart near $N = 40$, $Z = 28$ has drawn much attention due to experimental signatures suggesting the arrival of a neutron shell closure at $N = 40$ in ^{68}Ni . To understand and evaluate the meaning of these signatures, the quantum states predicted by the shell model in this region must be considered. A harmonic oscillator mean field alone predicts that 40 would be a magic number, completing the first four major harmonic oscillator shells. The inclusion of the spin-orbit interaction splits the energy degeneracy of orbitals within each shell and shifts the spacing between these orbitals. Of particular relevance here is the shifting of the $g_{9/2}$ orbital, the lowest-energy level of the fifth harmonic oscillator shell, which comes down in energy far enough to join the pf -shell. This effect is

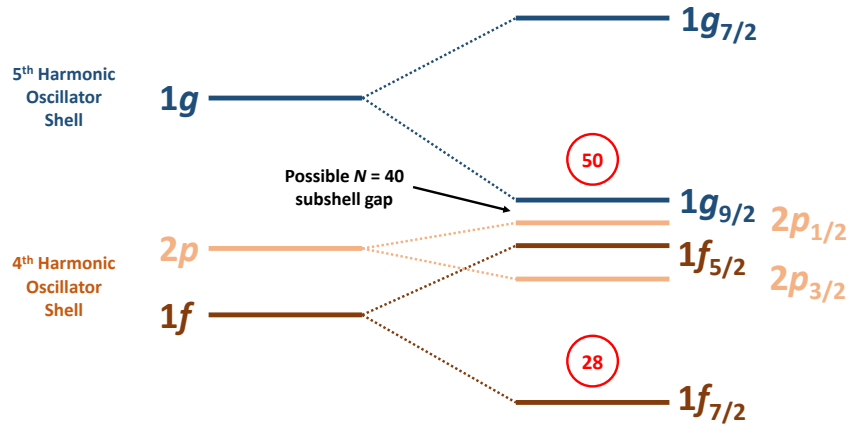


Figure 4.1: Single-particle shell model energy levels using a harmonic oscillator potential plus an l^2 interaction without spin-orbit interaction (left) and with spin-orbit interaction (right).

depicted in Fig. 4.1. The additional 10 particles accommodated by the $g_{9/2}$ orbital explains why 50, not 40, is the well-established magic number. The question of a potential shell or subshell closure at $N = 40$ is therefore a question of the spacing between this $g_{9/2}$ orbital and the pf -shell.

The evidence supporting a shell closure at $N = 40$ in ^{68}Ni is presented in Fig. 4.2. A large first-excited 2^+ state energy E_{2^+} and a small transition strength $B(E2; 0^+ \rightarrow 2^+)$ are clearly apparent at $N = 40$ in the nickel chain [72–74]. These effects quickly disappear when moving away from nickel. Such evidence presents a compelling case for a substantial shell gap at $N = 40$ in ^{68}Ni . However, as Grawe and Lewitowicz have pointed out [75], it is possible to account for the spectroscopic signatures presented in Fig. 4.2 purely because of the change in parity between the pf orbitals and the $g_{9/2}$ orbital, even with no energy gap between them. Furthermore, Langanke *et al.* demonstrated that much of the low-lying $B(E2)$ strength in ^{68}Ni comes from excited states above 4 MeV, and therefore the small $B(E2, 0_{\text{g.s.}}^+ \rightarrow 2_1^+)$ value does not necessarily require a significant energy gap across $N = 40$ [76]. To truly

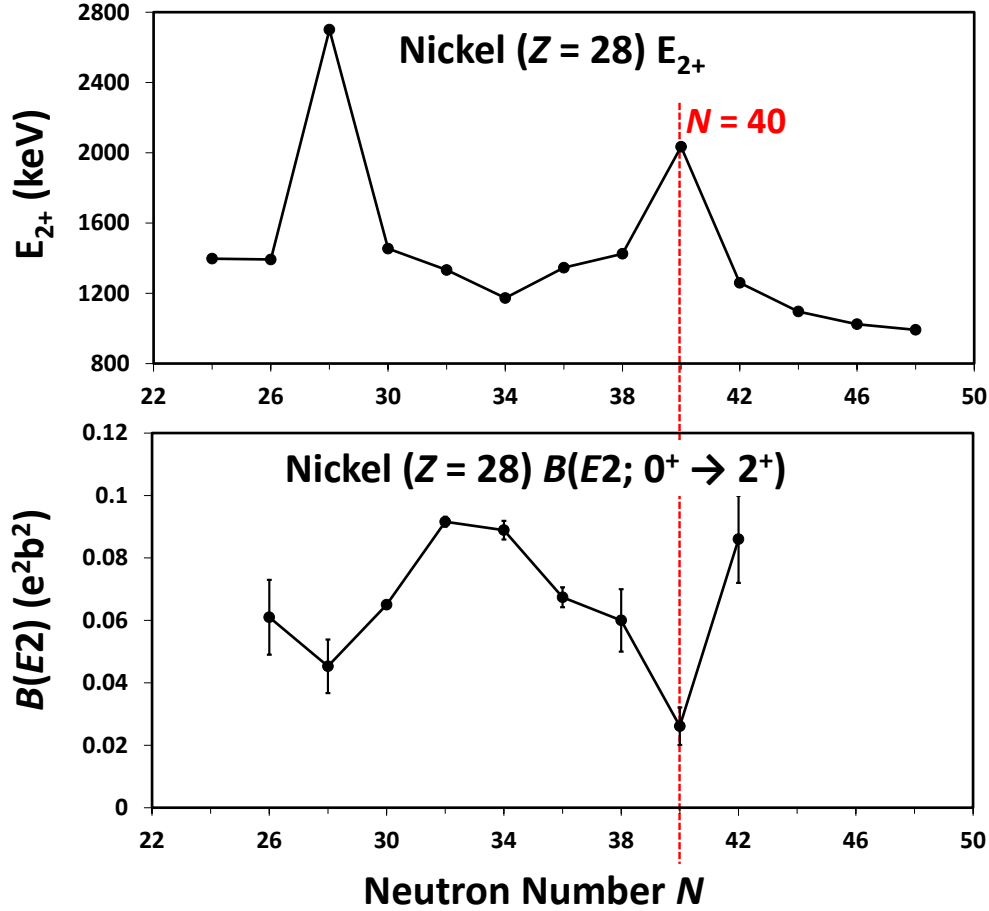


Figure 4.2: First-excited 2^+ state energies E_{2+} (top) and $B(E2; 0^+ \rightarrow 2^+)$ transition strengths (bottom) in the even-even nickel isotopes. All data taken from Ref. [74]. The large E_{2+} and the small $B(E2)$ values at $N = 40$ suggest a substantial shell gap.

examine whether an energy gap does arise at $N = 40$ in the nickel region, the additional probe of mass measurements must be considered.

4.1.2 Mass Measurements Around $N = 40$

For nuclear structure investigations, trends in nuclear binding are studied using proton and neutron separation energies (S_p and S_n) [77], defined as the difference between the binding energies of a given nucleus and the nucleus with one fewer proton or neutron (or, equivalently, the amount of energy required to remove a single proton or a single neutron from a given

nucleus). This is the nuclear analog of ionization energies in atomic science.

To investigate a potential neutron (sub)shell closure at $N = 40$, neutron separation energies must be considered. Nuclear pairing effects [78, 79] create an odd-even staggering when plotting S_n as a function of neutron number, because removing a neutron from a nucleus with an even number of neutrons requires additional energy to break a pair of neutrons before one can be removed. In many cases, this staggering effect obscures the trends being investigated. It is therefore common instead to consider two-neutron separation energies (S_{2n}), eliminating the odd-even staggering.

Two-neutron separation energies can be expressed as a function of atomic masses:

$$S_{2n}(N, Z) = [m(N - 2, Z) - m(N, Z) + 2m_n]c^2, \quad (4.1)$$

where m_n is the mass of a free neutron and c is the speed of light.

A simple liquid-drop model of the nucleus would suggest that, for a given proton number Z , S_{2n} steadily declines as a function of neutron number N . This can be found from the semi-empirical mass formula first presented by von Weizsäcker in 1935 [80]. In reality, this general steady decline encounters numerous deviations, indicating the presence of additional structure effects. For example, the two-neutron separation energies are plotted as a function of neutron number for isotopic chains in the region from $Z = 31$ to $Z = 50$ in Fig. 4.3. In this figure, the neutron shell closure at $N = 50$ can clearly be identified from the fact that the S_{2n} values drop very suddenly at $N = 50$ relative to the general decline. This is a result of the fact that adding neutrons beyond $N = 50$ results in filling a higher-lying neutron shell, from which the energy cost to remove two neutrons is significantly lower than the energy needed to remove neutrons from the lower shell. Other structure effects are visible in

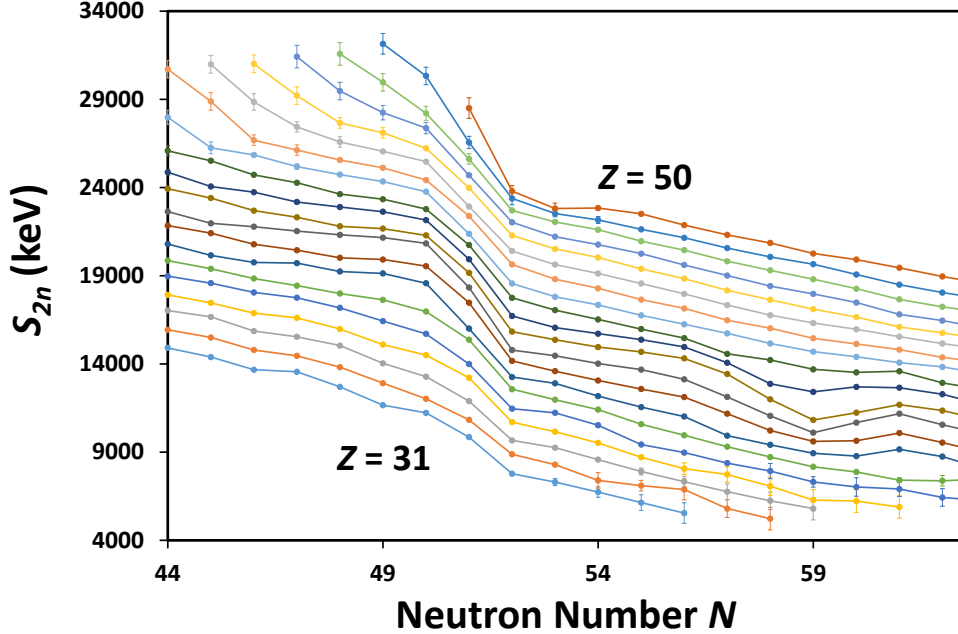


Figure 4.3: Two-neutron separation energy S_{2n} plotted as a function of neutron number N in the region from $Z = 31$ to $Z = 50$. Data are taken from the AME2016 atomic mass evaluation [1].

Fig. 4.3 as well, such as the onset of deformation between $N = 56$ and 61 for the elements Rb ($Z = 37$) to Ru ($Z = 44$) [77].

This tool of separation energies determined from mass measurements serves as an important probe to examine the structure in the region of ^{68}Ni . S_{2n} is plotted as a function of neutron number for the elements iron ($Z = 26$) to copper ($Z = 29$) in the region around $N = 40$ in Fig. 4.4. While an effect as dramatic as the major $N = 50$ shell closure seen in Fig. 4.3 is not expected, a smaller subshell closure at $N = 40$ should be indicated similarly by a sudden drop-off in S_{2n} when crossing $N = 40$. The observation of such an effect requires a relatively high degree of precision, with uncertainties ~ 10 keV or better in this region to ensure that the trends are not obscured by the error bars.

In recent years, online Penning trap mass spectrometry has provided such precise data extending beyond $N = 40$ in the nickel, copper, zinc, and gallium chains ($Z = 28 - 31$),

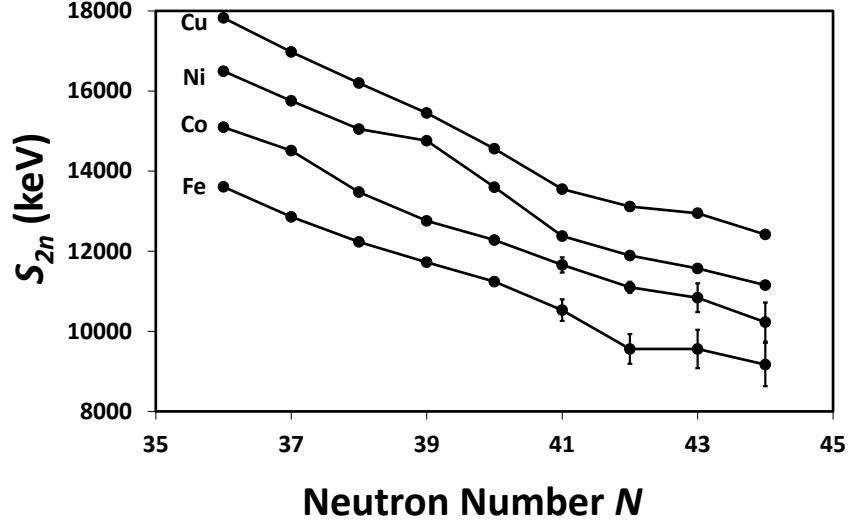


Figure 4.4: Two-neutron separation energy S_{2n} plotted as a function of neutron number N in the region around ^{68}Ni . Data are taken from the AME2016 atomic mass evaluation [1].

revealing no sign of a subshell closure across $N = 40$ [81, 82]. An odd kink is observed in the nickel chain at $N = 39$, which is not currently understood [81]. Measurements south of $Z = 28$ have so far been limited, however, due to the fact that iron ($Z = 26$) and cobalt ($Z = 27$) isotopes in this region are not available from ISOL facilities. As the only Penning trap mass spectrometer coupled to a fragmentation facility, LEBIT presents the unique opportunity to perform precise mass measurements of these elusive isotopes. A previous LEBIT campaign provided high-precision mass measurements of $^{63-66}\text{Fe}$ and $^{64-67}\text{Co}$, extending up to but not beyond $N = 40$ [83]. As can be seen in Fig. 4.4, the relatively large error bars beyond $N = 40$ in the iron and cobalt chains obscure the trends at the critical point of crossing $N = 40$. The first Penning trap mass measurements of $^{68,69}\text{Co}$ were recently completed at LEBIT, substantially reducing the error bars from the AME2016 values and enhancing the understanding of nuclear structure changes across $N = 40$ in the region near ^{68}Ni .

4.2 Experimental Procedure

^{68}Co and ^{69}Co were produced at the NSCL by the fast fragmentation process described in Chapter 3. The coupled cyclotrons were used to accelerate a stable primary beam of ^{76}Ge to an energy of 130 MeV/u, which then impinged on a thin Be target to induce fragmentation. Unwanted fragments were filtered out using the A1900 fragment separator, and the desired cobalt ions were delivered to the beam stopping facility. This experiment was carried out on two separate occasions approximately one year apart (hereafter referred to as “Run 1” and “Run 2”) due to poor efficiency through the gas cell during Run 1 ($< 1\%$ total efficiency), the cause of which was later traced to a floating electrode in the gas cell.

Chemical interactions in the gas cell presented significant challenges which required a large amount of effort to mitigate in order to successfully complete the mass measurements. These challenges and the methods used to work past them are discussed in detail in the following subsection.

4.2.1 Gas Cell Chemistry

High purity helium gas (99.999%) was passed through a Monotorr purifier before use in the gas cell to minimize the amount of stable contamination present. Additionally, all elements inside the gas cell were prepared under ultra-high vacuum standards for this purpose. Still, some level of impurity has always been observed from the gas cell [57], presenting two important challenges for the $^{68,69}\text{Co}$ experiment. First, as the radioactive beam passed through the gas cell, many of the ions of interest chemically bonded to stable contaminants, forming several molecules with different mass-to-charge (m/q) values (known as “molecular sidebands”). Following the gas cell, a dipole magnetic separator was used to select the

desired m/q , so with the desired cobalt isotopes spread over multiple molecular sidebands, a significant portion of the already low beam rate was lost at any selected m/q value.

The second challenge presented by contamination in the gas cell was that stable species at $m/q = 68$ and 69 came at significantly higher rates than the $^{68,69}\text{Co}^+$ ions of interest, arriving at the Penning trap at a ratio of more than 100:1. The dipole cleaning method described in Section 2.1.3 was not sufficient to thoroughly remove contaminants at such high rates, so isobaric contaminants initially overpowered the signal from the cobalt ions. For reasons not currently understood, the stable contaminants identified from the gas cell changed between Run 1 and Run 2. Table 4.1 summarizes the differences between Runs 1 and 2, including the stable contaminants identified in each case.

The molecular sidebands were investigated by measuring radioactivity on a silicon beta-detector immediately after the dipole magnetic separator and scanning the strength of the magnetic field in the separator to determine the presence of radioactive ions as a function of m/q . The results of these scans for both Run 1 and Run 2 while sending ^{68}Co into the gas cell are presented in Fig. 4.5. In an effort to break up stable molecular contaminants, a -150 V offset bias was applied to the gas cell extraction. This is a widely used technique known as collision induced dissociation (CID) [84–86], whereby energetic collisions with a buffer gas are used to induce fragmentation of molecular ions. It is clear from Fig. 4.5 that, during Run 2, a significant amount of $^{68}\text{Co}^{2+}$ was present at higher molecular sidebands which broke up after the bias was applied. The relative amount of $^{68}\text{Co}^{2+}$ extracted in Run 1 was much lower than in Run 2, however a small peak at $m/q = 34$ was apparent after the bias was applied. Though this peak was much smaller than the peak at $m/q = 68$, the amount of stable contamination at $m/q = 34$ was also much less, so the lower rate of $^{68}\text{Co}^{2+}$ was acceptable in exchange for manageable levels of isobaric contamination.

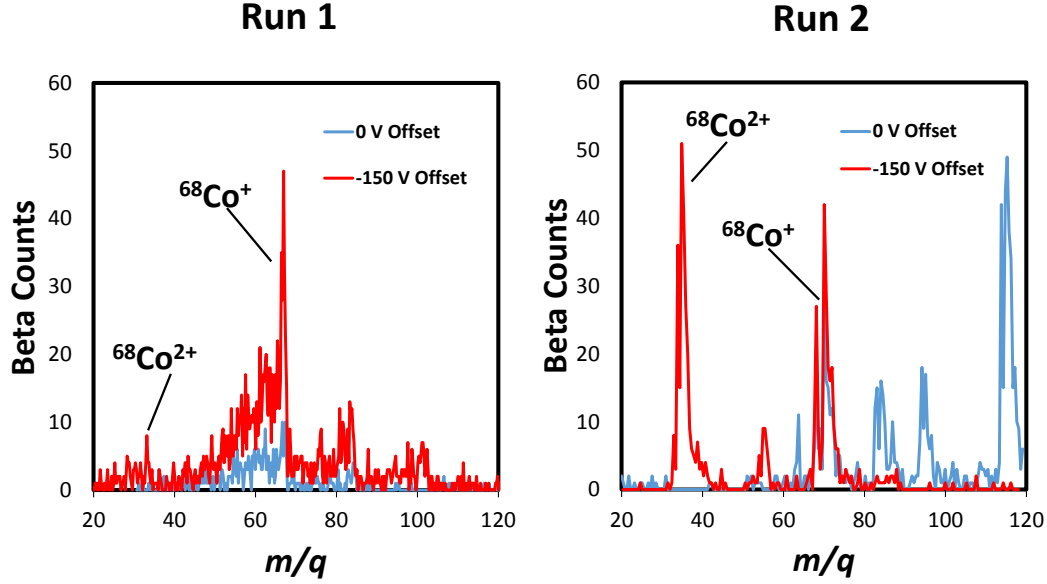


Figure 4.5: Radioactivity observed as a function of the m/q value transmitted through the dipole mass separator for Runs 1 and 2. The effect of CID is seen by comparing the case where there is no bias applied to the gas cell extraction to the case where a -150 V offset is applied. Note that m/q was scanned from high values to low in Run 1 and from low values to high in Run 2, hence the opposite directions of the decay tails.

Though the contamination at $m/q = 34$ was much lower than at $m/q = 68$, some effort was still required to reduce the contamination so that a TOF-ICR resonance of $^{68}\text{Co}^{2+}$ could be achieved. A set of slits was used to cut out a portion of the beam immediately after the dipole magnet. The slit width and position were adjusted while monitoring the radioactivity observed on the silicon beta-detector in order to cut as much of the beam as possible without reducing the amount of $^{68}\text{Co}^{2+}$. The dipole cleaning method described in Section 2.1.3 was used to remove known contaminants from the Penning trap. During Run 1, the additional step of SWIFT cleaning (described in the next subsection) was also required. In combination, these efforts were sufficient to obtain a TOF-ICR resonance of $^{68}\text{Co}^{2+}$.

The chemistry for ^{69}Co was the same as for ^{68}Co , so the dipole magnet was set to $m/q = 34.5$ when ^{69}Co was delivered from the A1900. For odd-mass isotopes like ^{69}Co , measuring

doubly-charged ions is particularly helpful for reducing stable contamination because no singly-charged contaminants will arrive at half-integer mass values. In this measurement, the only contaminant identified in the Penning trap was the doubly-charged daughter $^{69}\text{Ni}^{2+}$, which could easily be cleaned. Though the rate of $^{69}\text{Co}^{2+}$ arriving at the Penning trap was extremely low (< 0.5 ions/s), a $^{69}\text{Co}^{2+}$ TOF-ICR resonance could still be achieved thanks to the low level of contamination.

4.2.2 SWIFT Beam Purification

During Run 1, additional effort was needed to remove isobaric contaminants from the Penning trap in order to obtain a $^{68}\text{Co}^{2+}$ TOF-ICR resonance. Major beam components, such as $^{16}\text{O}^{18}\text{O}^+$, could be identified and removed from the Penning trap with the dipole cleaning method described in Section 2.1.3. However, a number of additional contaminants were present at a level too low to identify in the time allotted. To remove such contaminants, the Stored Waveform Inverse Fourier Transform (SWIFT) technique is used at LEBIT [87]. This technique employs a broadband excitation with a tailored waveform to drive all ions within a user-defined mass band without driving the ion of interest. Unlike the dipole cleaning method, which requires specific identification of each contaminant in order to drive it at the correct frequency ν_+ , SWIFT will clean all contaminants within the set band and does not require identification of each one. The effect of SWIFT cleaning for this experiment is demonstrated in Fig. 4.6.

	Run 1	Run 2
Species Measured	$^{68}\text{Co}^{2+}$, $^{69}\text{Co}^{2+}$	$^{68}\text{Co}^{2+}$
$^{68}\text{Co}^{2+}$ Reference Ion $^{69}\text{Co}^{2+}$ Reference Ion	$^{16}\text{O}^{18}\text{O}^+$ $^{39}\text{K}^+$	$^{34}\text{S}^+$ N/A
$^{68}\text{Co}^{2+}$ Detected Rate on MCP $^{69}\text{Co}^{2+}$ Detected Rate on MCP	0.2 counts/s 0.2 counts/s	0.6 counts/s N/A
Total $^{68}\text{Co}^{2+}$ Ions Detected Total $^{69}\text{Co}^{2+}$ Ions Detected	4779 4275	23129 N/A
CID Used?	Yes	Yes
SWIFT Used?	$^{68}\text{Co}^{2+}$: Yes $^{69}\text{Co}^{2+}$: No	$^{68}\text{Co}^{2+}$: No $^{69}\text{Co}^{2+}$: N/A
Number of $^{68}\text{Co}^{2+}$ Resonances Number of $^{69}\text{Co}^{2+}$ Resonances	7 5	10 N/A
Beam Contaminants	$m/q = 68$: $^{40}\text{Ar}^{12}\text{C}^{16}\text{O}^+$ $^{40}\text{Ar}^{14}\text{N}_2^+$ $^{12}\text{C}_4^1\text{H}_4^{16}\text{O}^+$ $^{12}\text{C}_3^1\text{H}_2^{14}\text{N}^{16}\text{O}^+$ +Unidentified $m/q = 34$: $^{16}\text{O}^{18}\text{O}^+$ +Unidentified $m/q = 69$: Unidentified $m/q = 34.5$: $^{69}\text{Ni}^{2+}$ (daughter)	$m/q = 68$: Unidentified $m/q = 34$: $^{34}\text{S}^+$ $^1\text{H}_2^{32}\text{S}^+$ $^1\text{H}^{33}\text{S}^+$

Table 4.1: Comparison of conditions for Run 1 and Run 2.

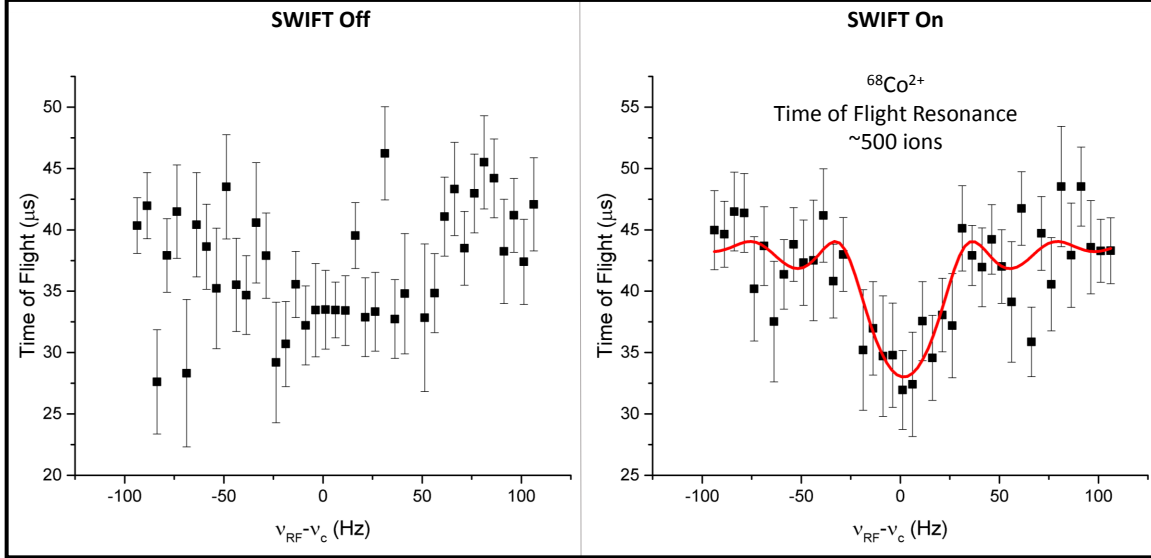


Figure 4.6: Attempted TOF-ICR resonances of $^{68}\text{Co}^{2+}$ with SWIFT off (left) and SWIFT on (right). A significant amount of unidentified stable contamination from the gas cell arrived at $m/q = 34$, obscuring the resonance before SWIFT was turned on. The use of SWIFT to clean unidentified contaminants made this measurement possible.

4.2.3 Isomer Investigations

β -decay experiments have reported the existence of two β -decaying states in ^{68}Co [88] and recently a second β -decaying state in ^{69}Co as well [89]. In the past, LEBIT has on several occasions demonstrated the ability to resolve ground and isomeric states when the states are populated at roughly equal proportions in the fragmentation process [83,90,91]. This is marked by a signature double peak in the TOF-ICR resonance, as seen in Fig. 2 of Ref. [91]. Because only a single peak in the TOF-ICR resonance was observed for both ^{68}Co and ^{69}Co , an additional step was implemented to examine which state was present in the rare isotope beam delivered to LEBIT.

Before the cobalt ions from the gas cell were delivered to LEBIT, they were collected in front of a high-purity germanium (HPGe) detector. A schematic overview of the major experimental components from this experiment, including the HPGe detector, is presented

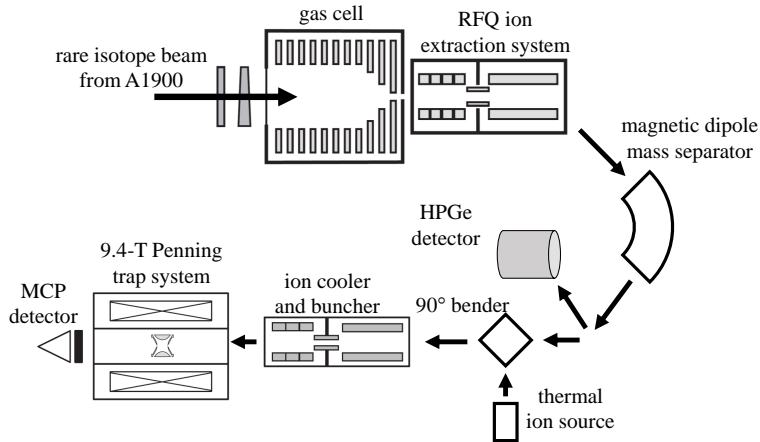


Figure 4.7: Schematic overview of the major experimental components used for this work.

in Fig. 4.7. As the cobalt decayed, β -delayed γ rays were detected with the HPGe detector. The presence or absence of particular γ rays could then provide an indication of which β -decaying state was observed, as discussed in great detail in the analysis section of this chapter. Gamma spectra were attempted in this manner during Run 1, however the rates were too low to observe any of the peaks of interest (see Table 4.1 for rates observed in the Penning trap). The improved rates during Run 2 yielded a useful gamma spectrum for ^{68}Co which is analyzed in Section 4.3.2. ^{69}Co was not re-measured in Run 2 due to limited beam time.

4.3 Results and Discussion

4.3.1 Mass Measurement Results

To account for magnetic field drifts, each cobalt measurement was preceded and followed by a reference measurement of a stable species with a well-known mass. The reference measurement frequencies were then linearly interpolated to determine the reference frequency at the time the ion of interest was measured. The effects of non-linear changes in the magnetic

field were previously studied at LEBIT and shown to contribute to the overall systematic uncertainty only at a level of $\sim 10^{-10}$ [63], which is negligible for this measurement. To minimize systematic frequency shifts, it is best to choose a reference species with a mass-to-charge ratio similar to that of the ion of interest [39]. In Run 1, the stable contaminant $^{16}\text{O}^{18}\text{O}^+$ arriving from the gas cell was used as a reference for $^{68}\text{Co}^{2+}$, and ^{39}K from the offline LEBIT thermal ion source was used as a reference for $^{69}\text{Co}^{2+}$. In Run 2, high levels of sulfur were observed from the gas cell, representing the predominant source of contamination. The origin of this sulfur is unknown. $^{34}\text{S}^+$ was therefore readily available as a reference ion for $^{68}\text{Co}^{2+}$ on that occasion.

After linear interpolation of the reference ion frequencies, the atomic mass of the ion of interest was then calculated from the ratio of the cyclotron frequencies of the two species using the equation

$$m = \left[m_{\text{ref}} - \frac{q_{\text{ref}}}{e} \cdot m_e \right] \times \frac{q}{q_{\text{ref}}} \frac{1}{r} + 2m_e \quad (4.2)$$

where r is the ratio $\frac{\nu_c}{\nu_{c,\text{ref}}}$ and e is the elementary charge. The ionization potentials of all species and the molecular binding of $^{16}\text{O}^{18}\text{O}^+$ are not included in these calculations as they are all < 20 eV and do not contribute at the level of uncertainty for this measurement [92]. In Run 1, seven ^{68}Co frequency ratios containing a total of 4779 $^{68}\text{Co}^{2+}$ ions were recorded with a weighted average $r_1 = 1.000641552(70)$. Two of these seven $^{68}\text{Co}^{2+}$ measurements used a 25 ms RF excitation time, one used a 50 ms RF excitation time, and four used a 100 ms RF excitation time. A near-unity Birge ratio [93] of 0.93(18) indicates that additional statistical effects are unlikely. In Run 2, ten ^{68}Co frequency ratios containing a total of 23129 $^{68}\text{Co}^{2+}$ ions, all excited with a 100 ms RF excitation time, were recorded with a weighted average $r_2 = 0.99987011(12)$. On this occasion the Birge ratio was 1.96(15), so the statistical

Ion	Run Number	Reference	Frequency Ratio	Mass (u)	ME (keV)	AME2016 (keV)	Δ ME (keV)
$^{68}\text{Co}^{2+}$	1	$^{16}\text{O}^{18}\text{O}^+$	1.000 641 552(70)	67.944 559 2(48)	-51 642.8(4.4)		290(190)
	2	$^{34}\text{S}^+$	0.999 870 11(12)	67.944 559 3(82)	-51 642.6(7.6)	-51 930(190)	290(190)
	Average			67.944 559 2(41)	-51 642.7(3.8)		290(190)
$^{69}\text{Co}^{2+}$	1	$^{39}\text{K}^+$	1.130 267 90(24)	68.946 093(15)	-50 214(14)	-50 280(140)	66(140)

Table 4.2: Measured frequency ratios, $\nu_c/\nu_{c,\text{ref}}$, calculated atomic mass and mass excess (ME) values, and their comparison to the values from 2016 Atomic Mass Evaluation. Differences in the mass excess values, $\Delta\text{ME} = \text{ME}_{\text{LEBIT}} - \text{ME}_{\text{AME2016}}$, are also listed.

uncertainty was inflated by multiplication with the Birge ratio. This commonly-used Birge adjustment is valid in the case where all uncertainties are underrated by the same common factor, which is taken to be true for measurements of equal reliability. Five frequency ratios were recorded for ^{69}Co , each using a 50 ms RF excitation time, with a weighted average $r = 1.13026790(24)$ and a Birge ratio of 1.22(21). This statistical uncertainty has also been inflated by multiplication with the Birge ratio. Systematic effects such as minor trap misalignment in the magnetic field and deviations from a purely quadrupole electric potential result in small frequency shifts dependent on the mass-to-charge difference from the reference ion. These shifts have previously been evaluated at LEBIT and contribute only at a level of $2.0 \times 10^{-10}/(q/u)$ [62], which is negligible for all frequency ratios considered here. Taking a weighted average of the results from the two independent measurements of ^{68}Co yields a mass excess of $\text{ME}(^{68}\text{Co}) = -51642.7(3.8)$ keV, and the mass excess of ^{69}Co was determined to be $\text{ME}(^{69}\text{Co}) = -50214(14)$ keV. A summary of these results from LEBIT and comparison with the AME2016 values [1] is presented in Table 4.2.

4.3.2 Level Assignment

Before drawing conclusions from these results, the possible presence of isomers must be considered. As previously discussed in Section 4.2.3, a HPGe detector was used to obtain

a spectrum of β -delayed γ rays from the decay of ^{68}Co during Run 2. This spectrum is presented in Fig. 4.8. The γ rays from this spectrum were then compared with the current literature available for ^{68}Co β decay [88,94,95]. While there is disagreement in the literature regarding the relative gamma intensities, there is agreement that decay from the low-spin state produces a 478 keV gamma ray and any production of 595 keV or 324 keV gamma rays are at very low intensities ($< 1\%$). Decay from the high-spin state of ^{68}Co , on the other hand, is associated with higher intensity production of the 595 keV and 324 keV gammas ($\sim 32\%$ and $\sim 38\%$, respectively) and no production of the 478 keV gamma ray. A simplified level scheme showing the relevant β -delayed gamma rays for the two β -decaying states of ^{68}Co is presented in Fig. 4.9. As shown in Fig. 4.8, the gamma spectrum collected as part of this work shows clear peaks at 595 keV and 324 keV, while no evidence of a peak at 478 keV is present. This demonstrates the presence of the high-spin beta-decaying state in ^{68}Co , and does not support the presence of any of the low-spin beta-decaying state.

It is worth noting that the absolute intensity of the 478 keV gamma in the low-spin state decay ($\sim 6\%$) is substantially lower than the reported intensities of the 595 keV and 324 keV gammas in the high-spin state decay ($\sim 32\%$ and $\sim 38\%$, respectively). Additionally, the high-spin state has a shorter half-life than the low-spin state (0.23(3) s as compared to 1.6(3) s) [88]. Accounting for the size of the peaks in the gamma spectrum, the detector efficiency at each energy, the relative intensities of each peak, and the expected decay losses from the gamma detector to the Penning trap, it was calculated that the low-spin state could have been present at a level just below detectability at the Ge detector and still been the dominating beam component at the Penning trap. These calculations are presented in detail in Appendix C. However, given that there is no positive evidence of a second state in the gamma spectrum or in the TOF-ICR resonance and the gamma spectrum shows compelling

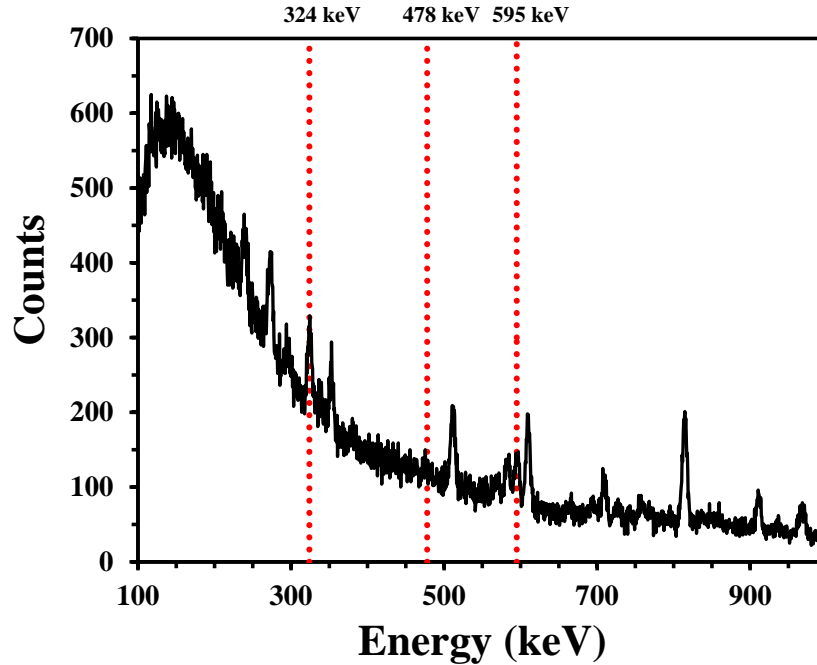


Figure 4.8: The β -delayed γ -ray spectrum detected following the decay of ^{68}Co . Dashed vertical lines mark the energies of γ rays known to follow primarily decay from only one of the two β -decaying states of ^{68}Co . γ rays at 478 keV follow decay from the low-spin state and γ rays at 324 and 595 keV follow decay from the high-spin state. The presence of clear peaks at 324 and 595 keV and the lack of a peak at 478 keV suggest that the high-spin β -decaying state of ^{68}Co was measured in this experiment. Other peaks in the spectrum have all been identified from either natural background radiation or ^{68}Co decays common to both β -decaying states.

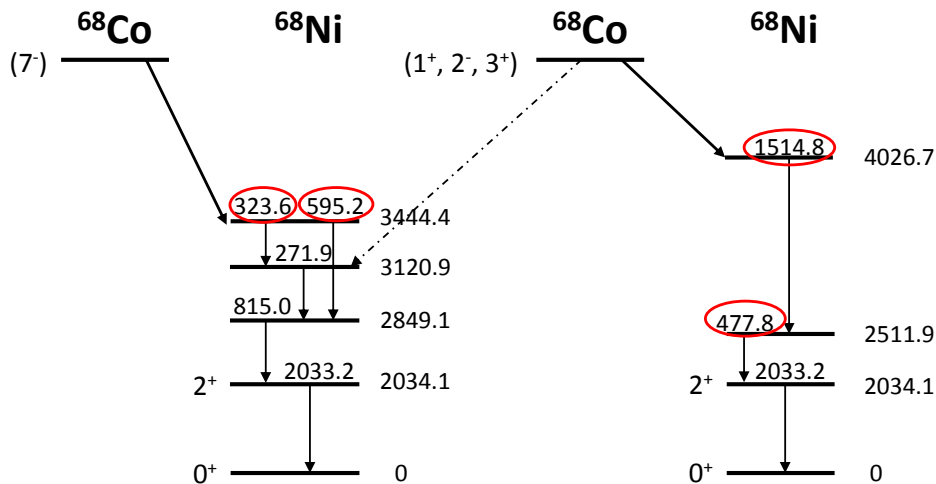


Figure 4.9: Simplified level scheme showing the relevant β -delayed gamma rays for the two β -decaying states of ^{68}Co . Circled gamma energies are those that signal the presence of one state or the other, but not both. Energies are all given in keV. Based on data from [88,94,95].

evidence for the presence of the high-spin state, we assume that this was in fact the state measured in the Penning trap.

No $^{69}\text{Co}^{2+}$ gamma spectra were obtained in this work. However, the $(1/2^-)$ beta-decaying state proposed by Liddick *et al.* [89] was only observed in ^{69}Co when produced by beta decay from ^{69}Fe . In that same experiment, ^{69}Co was also produced directly by projectile fragmentation, and there only the shorter-lived $7/2^-$ state was observed. As ^{69}Co was only produced directly by projectile fragmentation in this work (albeit with a different primary beam) and only one state was observed here as well, we assume that the ^{69}Co mass determination reported here corresponds to the $7/2^-$ state.

With these assumptions, we conclude that, in both ^{68}Co and ^{69}Co the one state measured in the Penning trap was the beta-decaying state with the higher spin. However, in both cases, the ordering of the beta-decaying states is still unknown. Mueller *et al.* proposed spin and parity assignments for the two states in ^{68}Co based on angular momentum coupling of the two beta-decaying configurations in ^{69}Ni with an $f_{7/2}$ proton hole [88], which would suggest a high-spin (7^-) ground state and a low-spin (3^+) isomer. This argument follows the rules for angular momentum coupling of particle-hole configurations in odd-odd nuclei laid out by Brennan and Bernstein [96]. While others have suggested alternate spin and parity assignments for the low-spin state [94,97], none have yet offered any contradiction to this ordering.

In the case of ^{69}Co , one of the beta-decaying states is believed to be $7/2^-$ based on the $\pi f_{7/2}^{-1}$ configuration observed in all other odd- A cobalt isotopes, and the other beta-decaying state proposed by Liddick *et al.* is described as a $(1/2^-)$ prolate-deformed intruder state attributed to proton excitations across the $Z=28$ shell as has been suggested for ^{65}Co and ^{67}Co [98]. The $(1/2^-)$ state approaches the $7/2^-$ ground state near $N=40$ and becomes

isomeric, possibly even crossing the ground state, at ^{69}Co . No comment on the ordering of these two states can be made in [89], but their separation is limited to <467 keV or <661 keV depending on the assumed strength of the unobserved M3 γ -ray transition.

To shed light on the ordering of the β -decaying states in ^{68}Co and ^{69}Co , a team of many-body nuclear structure theorists was consulted to perform *ab initio* calculations using the valence-space in-medium similarity renormalization group (VS-IMSRG) [99–103] framework based on two-nucleon (NN) and three-nucleon (3N) forces from chiral effective field theory [104, 105]. In particular, the SRG-evolved [106] 1.8/2.0 (EM) interaction from Refs. [107, 108] was used, which predicts realistic saturation properties of infinite matter and has been shown to reproduce well ground-state and separation energies from the p -shell to the tin isotopes [109, 110]. The Magnus formulation of the IMSRG [111] was then used to construct an approximate unitary transformation to decouple a given valence space Hamiltonian (and core energy) to be diagonalized with a standard shell-model code [112].

Two different valence space strategies for cobalt isotopes were considered. The first used standard $0\hbar\omega$ spaces for both protons and neutrons: for protons, the pf shell; for neutrons, the pf shell above a ^{40}Ca core for $N < 40$, and the sdg shell above a ^{60}Ca core for $N > 40$. These spaces allow for no neutron excitations at $N = 40$, so we know *a priori* that calculations in this vicinity will be unreliable. Since this is also the region of interest for the current measurements, a cross-shell $p_{1/2}f_{5/2}g_{9/2}$ neutron space was also decoupled using a ^{52}Ca core.

With the $p_{1/2}f_{5/2}g_{9/2}$ space, the ground state in ^{68}Co was found to be a 2^- , which agrees with the spin-parity of the low-spin beta-decaying state suggested by Flavigny *et al.* [94], though Flavigny *et al.* make no comment on whether this is the ground state. The calculations predict a large number of states below 1 MeV, so a definitive prediction of the

ground-state is not possible given present theoretical uncertainties. In the case of ^{69}Co , the ground state was calculated to be $7/2^-$, consistent with the surrounding odd-mass cobalt isotopes.

It is clear that additional work is needed to clarify the orderings of the two beta-decaying states in ^{68}Co . Mueller *et al.* suggest a high-spin ground state [88] while the VS-IMSRG calculations suggest a low-spin ground state, as is the case for the two odd- N cobalt isotopes just below $N = 40$. However, with the large number of close lying states, neither proposal is presented with a high degree of confidence. For the purpose of examining mass surfaces in the regions of ^{68}Ni , the high-spin state of ^{68}Co measured in this work is treated as the ground state. Should future work challenge this assignment, it is worth noting that the results presented in this work will still be valuable for a precise determination of the ground-state mass if the excitation energy of the isomeric state has been measured.

4.3.3 Evaluation of Two-Neutron Separation Energy Trends

The trends in S_{2n} are presented in Fig. 4.10, showing the AME2016 data and results from this work. While the AME2016 data shows a fairly linear trend along the cobalt chain from $N=39$ to $N=42$, the new LEBIT data demonstrates a substantial (287 keV) reduction in binding at $N=41$, creating a small kink in the S_{2n} chain which might suggest a minor subshell closure at $N = 40$. If the uncertain IMSRG prediction of a low-spin ground state is later proven to be accurate, suggesting the high-spin state measured in this work is the isomeric state, this kink will be reduced and the true S_{2n} values will return towards the AME2016 values. The S_{2n} value for ^{70}Co ($N=43$) increases due to the decrease at $N=41$, however the mass of ^{70}Co itself is still unmeasured, leaving a relatively large uncertainty on this point.

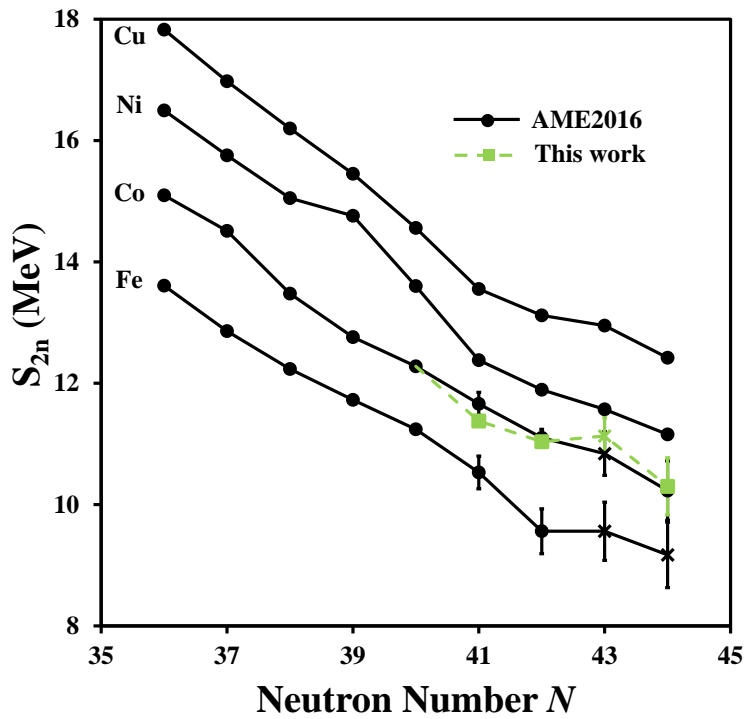


Figure 4.10: Two-neutron separation energies S_{2n} plotted as a function of neutron number N for isotopes of iron, cobalt, nickel, and copper. Green square points correspond to new cobalt values from this work and black circles correspond to data from AME2016 [1]. Points plotted with an x marker indicate values derived not from purely experimental data in the AME2016.

To examine the $N = 40$ kink more quantitatively, the neutron shell gap parameter has also been calculated, defined as

$$\Delta_N(N, Z) = S_{2n}(N, Z) - S_{2n}(N + 2, Z). \quad (4.3)$$

Δ_N is plotted as a function of neutron number for iron, cobalt, nickel, and copper in Fig. 4.11 in the region of $N = 40$. While the new measurement of ^{68}Co greatly reduces Δ_N at $N=41$ in the cobalt chain, it also increases Δ_N at $N = 39$ such that no relative peak is observed at $N = 40$. However, the high precision of the LEBIT results reveals a small but significant enhancement of Δ_N at $N=39$, somewhat smaller than what can already be seen at $N=39$ in the copper chain and significantly smaller than the peak at $N=39$ seen in the nickel chain. While it does not make any sense from a shell model perspective to consider this a sign of a shell or subshell closure, this does seem to suggest some as yet unexplained behavior resulting in additional stability at $N=39$ in this region.

Interestingly, the IMSRG calculations discussed previously capture this surprisingly large binding at $N = 39$ in the nickel chain. A comparison of the IMSRG calculations and the AME2016 data for the nickel chain in this region is presented in Fig. 4.12. IMSRG calculations performed within a single harmonic oscillator shell (using only pf shell for $N \leq 40$ and sdg shell for $N > 40$) demonstrate significant underbinding and result in an unphysical discontinuity crossing $N = 40$. As mentioned above, this discontinuity is well understood to be due to the lack of allowed neutron excitations near $N = 40$, which is an artifact of this particular choice of valence space; indeed the binding is significantly improved for $N < 40$, and the discontinuity across $N = 40$ disappears when a $pf_{5/2}g_{9/2}$ neutron space is used instead. Both cases capture the large binding at $N = 39$ observed in the AME2016 data.

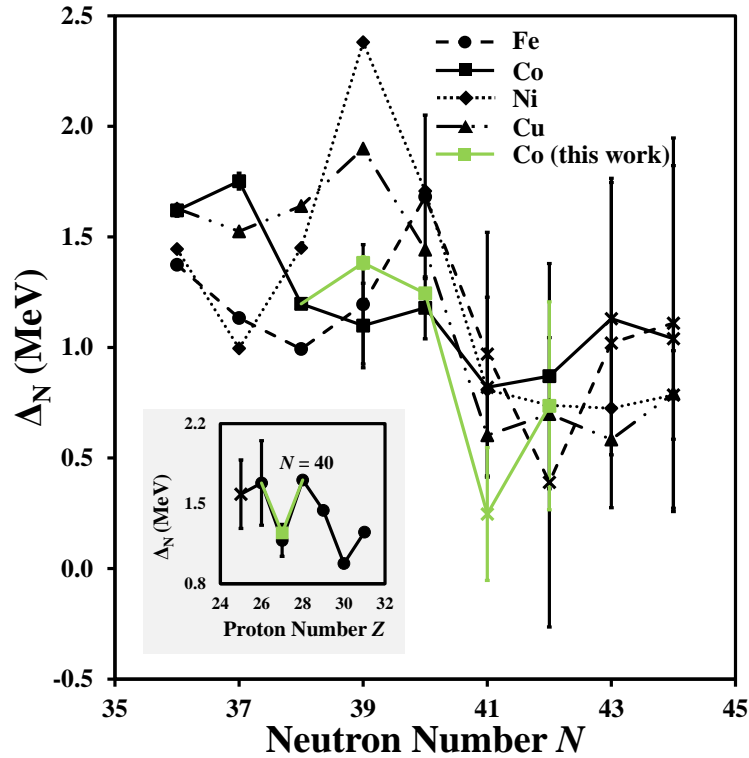


Figure 4.11: Neutron shell gap Δ_N plotted as a function of neutron number N for isotopes of iron, cobalt, nickel, and copper. The green curve corresponds to new cobalt values from this work and the black curves correspond to data from AME2016 [1]. Points plotted with an x marker indicate values derived not from purely experimental data in the AME2016. Inset: Neutron shell gap plotted as a function of proton number Z for isotopes with $N = 40$ neutrons.

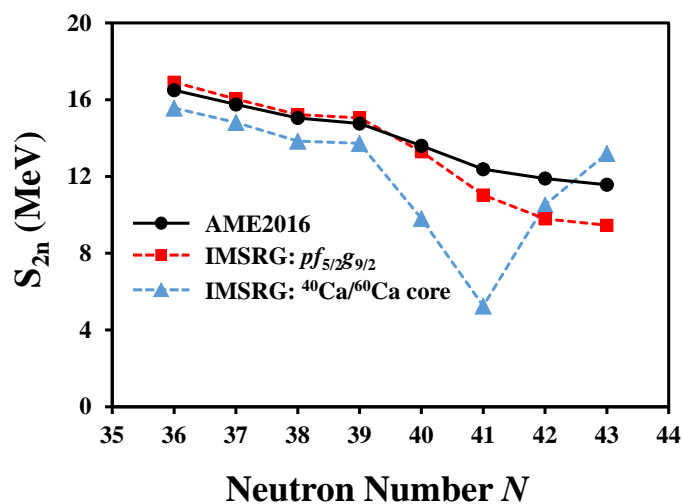


Figure 4.12: Two-neutron separation energies S_{2n} plotted as a function of neutron number N for the nickel isotopic chain. The solid black data are taken from AME2016, and the dashed lines correspond to IM-SRG theoretical calculations. Blue triangles use a ^{40}Ca core for $N \leq 40$ (pf neutron valence space) and a ^{60}Ca core for $N > 40$ (sdg neutron valence space). Red squares use a $pf_{5/2}g_{9/2}$ valence space for protons and neutrons for the entire chain starting from a ^{56}Ni core.

Chapter 5

Development of a Single Ion Penning Trap Mass Spectrometer for Rare Isotopes

5.1 SIPT Concept and Requirements

The Single Ion Penning Trap (SIPT) relies fundamentally on the non-destructive narrowband FT-ICR technique discussed in Section 2.2, in which the cyclotron frequency of an ion in a Penning trap is determined by using a tuned resonator circuit to detect the image charge induced on the trap electrodes. However, the extension of this technique to a single radioactive ion presents a number of technical challenges which must be met to successfully achieve a complete mass determination.

First, all of the technical requirements previously discussed for production and trapping of a radioactive ion are still applicable. This makes LEBIT an excellent location to house such a project, as it is already set up to take full advantage of the world-class beam production, isotope selection, and beam stopping facilities at the NSCL. By redirecting the ions to SIPT just before the 9.4-T TOF-ICR magnet, SIPT can also utilize the existing LEBIT cooler/buncher and offline ion sources. Still, the addition of SIPT to the LEBIT facility

required the assembly of a new stretch of beamline and a new superconducting magnet within the limited space of the LEBIT room. Among other considerations, these space requirements mean that the beam must be directed around a 115° bend to reach the SIPT magnet. A discussion of the new SIPT beam transport system is presented in Section 5.2.

Once the ions reach the Penning trap, a highly sensitive detection system is required to reliably detect the image charge created by a single, singly-charged ion. The relevant figure which must be optimized to achieve this goal is the signal-to-noise ratio S/N , which is the ratio of the root mean square (RMS) voltage signal generated in a narrowband FT-ICR detection circuit to the RMS Johnson-Nyquist noise [113]. This ratio is given approximately by

$$S/N \sim Nq \left(\frac{\rho}{\rho_0} \right) \sqrt{\frac{\nu}{\Delta\nu}} \sqrt{\frac{Q}{k_B T C}}, \quad (5.1)$$

where N is the number of ions, q is the ion charge, $\frac{\rho}{\rho_0}$ is the radius of the ions' orbit relative to the trap radius, $\frac{\nu}{\Delta\nu}$ is the ratio of the ion frequency and the spectral width, k_B is the Boltzmann constant, and Q , T , and C are the quality factor, temperature, and capacitance of the detection circuit, respectively [2, 53]. The goal of SIPT is to obtain measurements with a single, singly-charged ion, thus fixing N and q . The ion and trap radii are chosen to maximize the induced image charge while keeping frequency shifts due to field imperfections and special relativity within acceptable limits; a detailed discussion of these considerations is presented in Section 5.3.1.2.

The key to reaching adequate S/N for a single radioactive isotope therefore lies in optimizing the RLC detection circuit. In particular, the circuit quality factor Q , defined as

$$Q = \frac{\nu_{circ}}{\Delta\nu_{circ}} \quad (5.2)$$

must be ~ 1000 or greater. Achieving such a narrow circuit resonance requires a superconducting inductor coil, so SIPT must be operated at cryogenic temperatures to keep the inductor coil below its critical temperature. Cryogenic operation provides the additional benefit of very low thermal noise, further improving S/N as demonstrated by the factor of $\frac{1}{\sqrt{T}}$ in Eq. (5.1).

To test the feasibility of performing meaningful scientific measurements with SIPT, simulated data was generated in the time domain, Fourier transformed, and then fit with a Lorentzian function in the frequency domain. The achievable S/N for ^{100}Sn ($t_{1/2} \sim 1$ s) and ^{78}Ni ($t_{1/2} \sim 0.1$ s) was estimated using Eq. (5.1) with estimates for SIPT parameters shown in Table 5.1 and assuming an observation time of one half-life for each ion. Numerical pre-factors needed for Eq. (5.1) for a hyperbolic trap were taken from Ref. [53], which used the relaxation method to calculate the electric potential in this trap geometry. The simulated data consisted of sine waves of random phase with random noise generated at the relative amplitude required to obtain the expected S/N . The center frequency uncertainty of the Lorentzian fits was then used to determine the obtainable precision for a given S/N . The results of these simulations are presented in Fig. 5.1. Based on Eq. (5.1), the estimated S/N is around 1.5 in the time domain. While this number may sound low, the time domain S/N may be very small and still reveal a clear peak in the frequency domain provided the signal is sampled for a large number of periods. Using one half-life for the sample time, the simulated data produced clear, easily fit peaks in the FFT with S/N well below 0.1. As seen in Fig. 5.1, the obtainable precision is expected to be around 10^{-7} or better, which is more than sufficient for nuclear structure and nuclear astrophysics studies.

ρ/ρ_0	0.5
Q	2000
T	5 K
C	30 pF

Table 5.1: Parameters used to estimate the achievable S/N for narrowband FT-ICR measurements with a single ion.

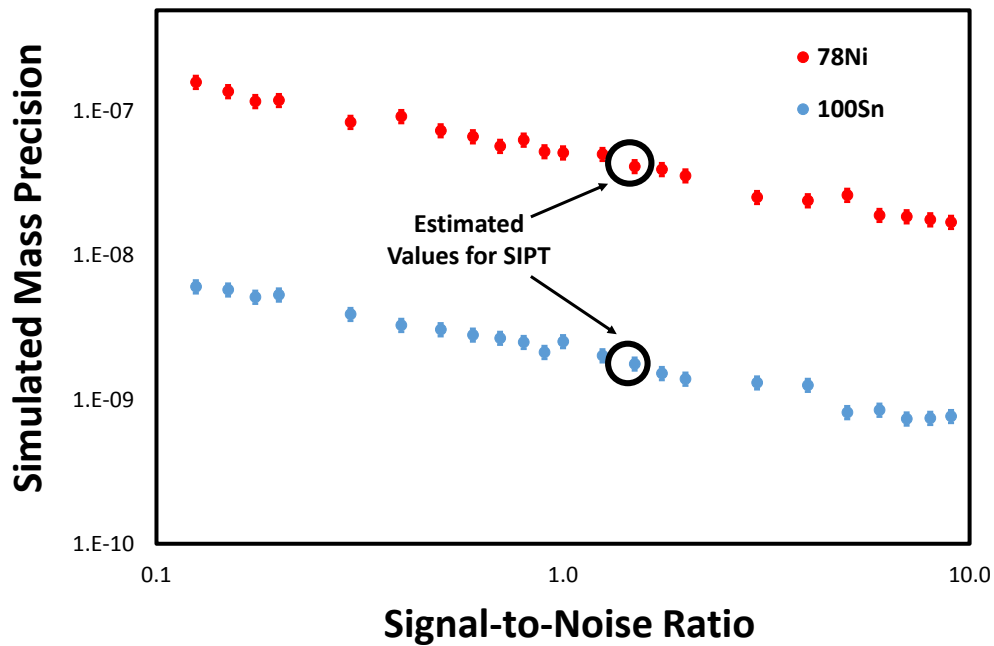


Figure 5.1: Frequency domain fit precision as a function of signal-to-noise ratio for simulated single ion signals from $^{78}\text{Ni}^+$ and $^{100}\text{Sn}^+$

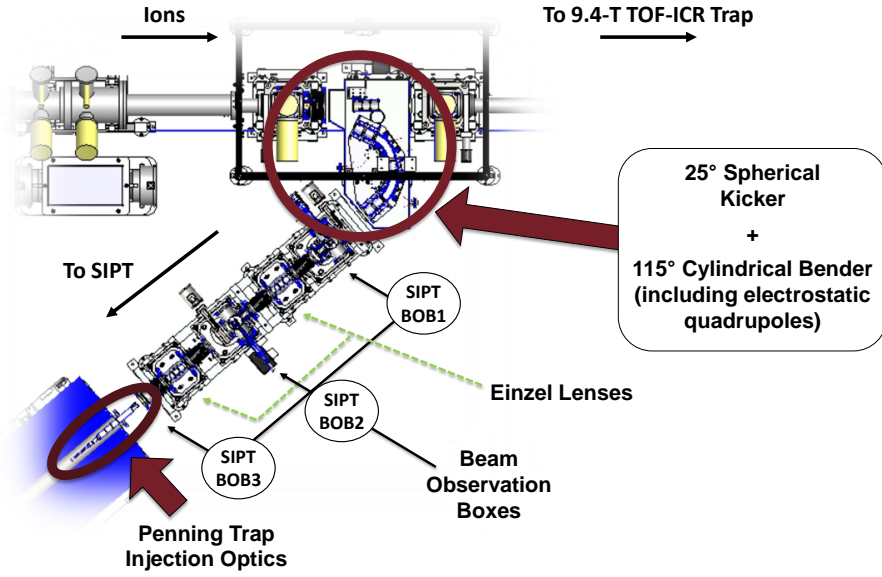


Figure 5.2: Layout of the major components of the new SIPT beamline.

5.2 The SIPT Beamline

A new section of beamline was built in order to transport ions to the SIPT Penning trap. It is important to recognize that this beamline was built in addition to, not in place of, the existing LEBIT beamline. In the new setup, ions will either be transported to the 9.4-T magnet for TOF-ICR measurements if rates are sufficiently high, or to the 7-T SIPT magnet for FT-ICR measurements when single ion sensitivity is required. The layout of the new SIPT beamline is presented in Fig. 5.2.

To deliver ions to SIPT, a 25° spherical kicker diverts ions ejected from the LEBIT cooler/buncher to the SIPT beamline. Ions then follow a 115° cylindrical bender, which includes an electrostatic quadrupole doublet at each end and an additional electrostatic quadrupole singlet in the middle for transverse focusing. A picture of the bender with electrostatic quadrupoles is presented in Fig. 5.3. Following the 115° bend, ions follow a straightaway path to the 7-T magnet, which includes three Beam Observation Boxes (BOBs)



Figure 5.3: 115° cylindrical bender, with integrated electrostatic quadrupole doublets on each end and a quadrupole singlet in the middle for transverse beam focusing.

for diagnostics and two einzel lenses for additional focusing. Beam trajectories from the kicker to the magnet were simulated in SIMION [114] to optimize the relative distances of these ion optical elements and to estimate the best focusing potentials. The simulated ion trajectories are presented in Fig. 5.4.

The three BOBs along the straightaway section of the SIPT beamline are equipped with Faraday cups, MCP detectors, and phosphorus screens with viewing cameras to characterize the beam at each location. SIPT BOB1 immediately follows the 115° bender, SIPT BOB2 sits between the two einzel lenses, and SIPT BOB3 is located just before the 7-T magnet. The MCP at SIPT BOB3 is situated in a Daly configuration to allow for TOF-ICR measurements with SIPT, as described in Section 5.3.1.4.

A series of drift tubes are then used to guide the ions inside the magnet to the Penning trap. These injection/ejection optics were designed both to inject ions from the SIPT beamline into the trap and to allow for reverse extraction to the Daly MCP for TOF-ICR measurements. The design for these drift tubes was based on the optics used for extraction from the 9.4-T Penning trap, with modifications to fit in the allowed space and to provide the focusing necessary for the MCP and deceleration for injection on the same voltage settings.

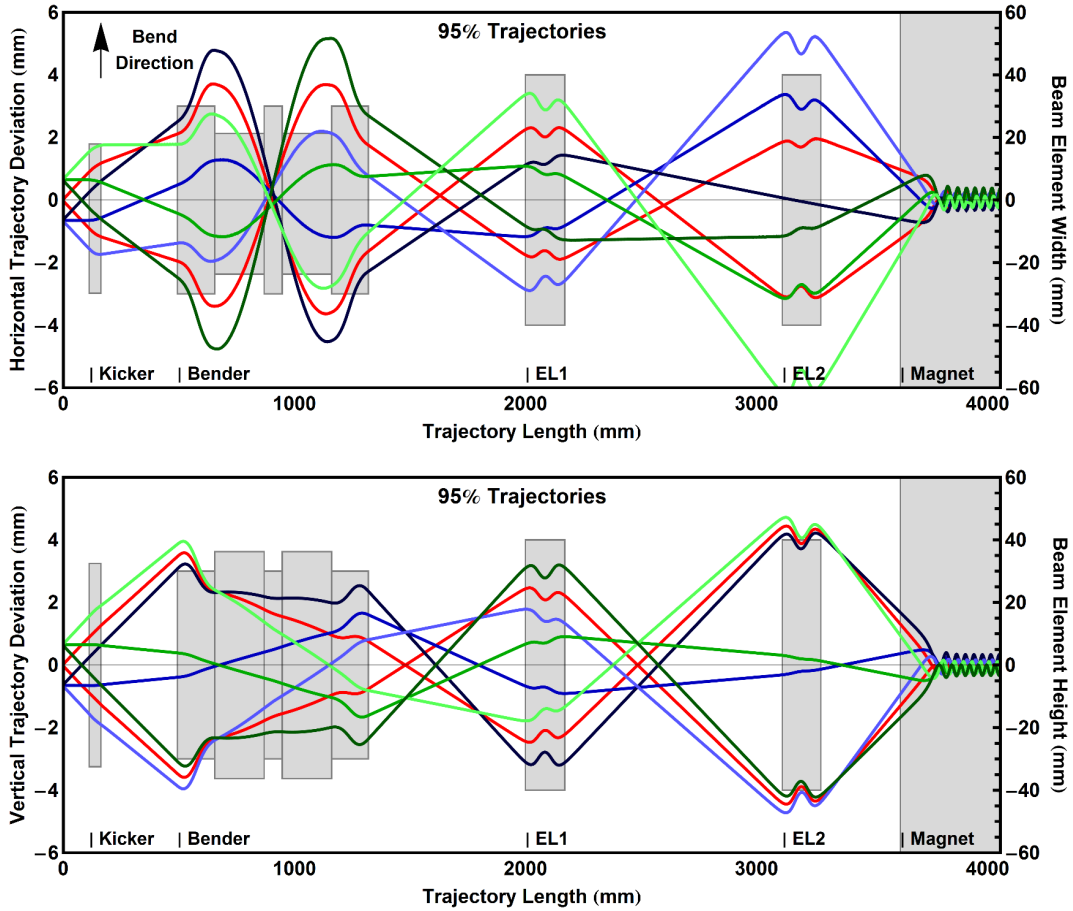


Figure 5.4: Simulated ion trajectories through the SIPT beamline, from the kicker to the 7-T SIPT magnet.

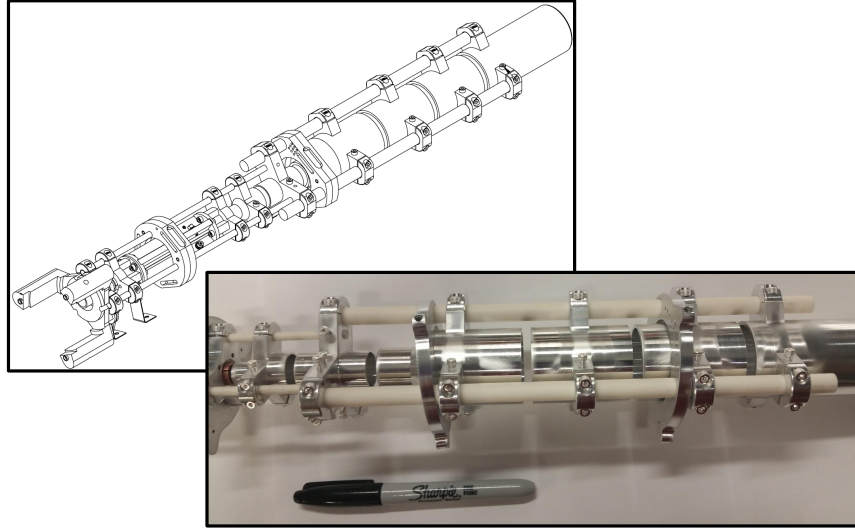


Figure 5.5: Design drawing and photograph of the drift tube assembly used for ion injection/ejection to/from the SIPT Penning trap.

The design drawings and a photograph of the injection/ejection optics are presented side-by-side in Fig. 5.5. The second-to-last drift tube before the Penning trap (DT7) is subdivided longitudinally into four cylindrical arc segments centered on the x - and y - axes to create a Lorentz steerer [50] to control the initial magnetron radius of the ions in the Penning trap.

5.3 The SIPT Penning Trap

5.3.1 Spectrometer Design

5.3.1.1 The SIPT Magnet

SIPT uses a 7-T superconducting solenoid magnet from Oxford Instruments. Magnet specifications as provided by the supplier are presented in Table 5.2. The magnetic field is created by running a nominal current of 205 amperes through niobium-titanium superconducting windings and operates at 4.2 K in liquid helium. Active shielding is employed to reduce the fringe field outside of the magnet. A 95 mm horizontal room-temperature bore provides

Central Field	7.0 Tesla at 4.2 K
Magnet Operating Current	205 Amperes (Nominal)
Field Decay (72 Hrs Measurement)	≤ 50 ppb/hr
LHe Refill Volume	122 ± 10 L
LHe Hold Time	≥ 90 days
LN2 Refill Volume	84 ± 5 L
LN2 Hold Time (Designed)	≥ 14 days
LN2 Hold Time (Guaranteed)	≥ 10 days
Bore Diameter	95 mm (+2 mm/-0 mm)
Overall Length	985 mm ± 2 mm

Table 5.2: Oxford magnet specifications as provided by the supplier.

experimental access to the central magnetic field.

To slow liquid helium evaporation losses, the helium dewar is shielded from room temperature by a vapor-cooled shield and liquid nitrogen vessel. Liquid nitrogen is refilled weekly, and liquid helium is replenished approximately every two months.

A superconducting switch was used to short-circuit the windings once the magnet was energized so that the magnet operates in true persistent mode. This results in excellent field stability over time, with a field decay of ≤ 50 ppb/hr. ICR frequency shifts due to magnetic field decay can be accounted for by taking occasional measurements of reference ions with well-known mass, as described previously for the current LEBIT system.

Spatial uniformity of the magnetic field was studied to examine potential systematic frequency shifts due to axial trap vibrations caused by the cryocooler or magnetic field misalignment from the bore tube. These studies are presented in detail in Appendix B and show that these frequency shifts should be negligible for SIPT.

5.3.1.2 Penning Trap Electrode System

The electrostatic quadrupole potential required for axial ion confinement is generated by a set of precisely machined hyperbolic trap electrodes. Other Penning trap electrode geome-

tries are possible, however the hyperbolic geometry provides the best approximation of a true quadrupole potential with finite electrodes [38]. This is a particularly important consideration for SIPT, because frequency shifts due to electric field imperfections become more pronounced as ions get closer to the trap electrodes, and image current detection requires that the ions be driven as close to the electrodes as possible.

The design ultimately chosen for the SIPT Penning trap electrode system is based on the Penning trap currently used in the 9.4-T magnet for TOF-ICR measurements at LEBIT, but scaled down to 50% of the size. This reduction of the Penning trap size allows ions to get closer to the electrodes for better image current pickup without driving the ions to an excessively large radius, which would introduce frequency shifts due to special relativity. A study of frequency shifts due to special relativity effects is presented in Appendix B, and indicates that such effects should not be a concern for SIPT with this smaller trap size.

The SIPT Penning trap design is presented in Fig. 5.6, and trap dimensions are presented in Table 5.3. Field imperfections due to the finite size of the end cap and ring electrodes are largely compensated by correction ring electrodes, and additional imperfections due to the small hole in the end cap needed to allow ions to enter and exit the trap are largely compensated by correction tube electrodes [41]. The SIPT ring electrode is segmented into eight identical pieces, allowing flexibility in the configuration of ring segments for driving and picking up the modified cyclotron and true cyclotron components of the ion motion.

The SIPT trap electrodes are made of oxygen-free high thermal conductivity (OFHC) copper to ensure good thermal conductivity at cryogenic temperatures and plated with gold to reduce potential electric field irregularities due to patch effects. Sapphire insulators are used to maintain excellent thermal conductivity across the trap. Pictures of the SIPT electrodes before, during, and after assembly are presented in Fig. 5.7.

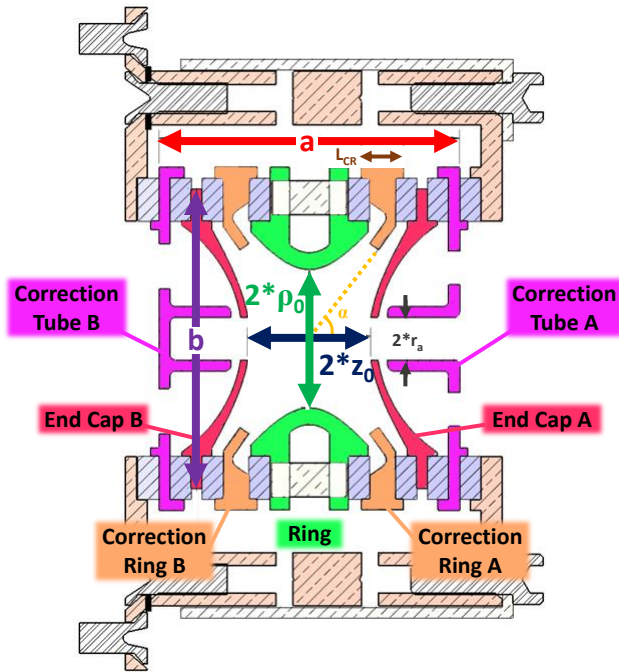


Figure 5.6: Design drawing of the SIPT Penning trap corrected hyperbolic electrode system. Trap dimensions given in Table 5.3.

a (Height Endcap-to-Endcap)	28 mm
b (Radial Width)	28 mm
L_{CR}	3.9 mm
ρ_0	6.485 mm
z_0	5.59 mm
r_a	2 mm
α	54.74°

Table 5.3: SIPT Penning trap dimensions (see Fig. 5.6.)



Figure 5.7: SIPT Penning trap electrodes before assembly (left), partway through assembly (middle) and after assembly (right).

5.3.1.3 Cryogenic System

As discussed in Section 5.1, the SIPT detection system must operate at cryogenic temperatures in order to achieve single ion sensitivity. The niobium-titanium superconducting wire used for the SIPT inductor coil has a critical temperature of around 10 K, however this critical temperature decreases in strong magnetic fields. The expected critical temperature in the SIPT magnet is around 6 K. To reach this low temperature for the SIPT detection system, a series of studies were performed to determine the cooling power requirements considering radiative heat losses and conductive losses through wire leads to room temperature [115]. Allowing for some uncertainty in these studies and possible provisions for future system changes, it was determined that 1.5 W of cooling power at 4 K should be more than sufficient.

These cooling requirements are met by the PT415 cryorefrigerator with CP1110 helium compressor from Cryomech, Inc. Vendor specifications for this model are summarized in Table 5.4. This is a pulse-tube cryocooler, which has the highly important feature of no moving parts in the low temperature section of the device, resulting in very low vibrations, high reliability, and low cost of operation and maintenance compared to other cryocoolers. This model also has a remote motor option, which is important because the entire LEBIT system is biased to 30 kV during online experiments. The remote motor option allows the compressor package to remain at ground outside the LEBIT room, connected by transfer lines with a high-voltage insulating break to the cold head which is mounted to the SIPT magnet at 30 kV.

The SIPT cryocooler includes two temperature stages. The first stage reaches temperatures around 45 K and is thermally coupled to a copper shield which surrounds the lower

Cold Head	
Cooling Capacity	1.5 W @ 4.2 K with 40 W @ 45 K
Lowest Temperature	2.8 K with no load
Cool Down Time	60 minutes to 4 K with no load
Weight	55 lb (25 kg)
Compressor Package	
Weight	420 lb (190.5 kg)
Dimensions (L x W x H)	24 x 24 x 31 in (61 x 61 x 79 cm)
Power Consumption @ Steady State	10.7 kW

Table 5.4: Vendor specifications for PT415 cryorefrigerator with CP1110 helium compressor from Cryomech, Inc.

temperature stage, blocking the sightline to the room temperature surroundings to reduce radiative heating. The second stage operates around 4.2 K, though it can reach as low as 2.8 K with no load. This stage is thermally coupled to the key SIPT cryogenic components including the superconducting resonator circuit, cryogenic amplifier, and Penning trap electrodes.

A diagram of the cryogenic stages of SIPT is presented in Fig. 5.8. The cold head sits inside the SIPT detection box, which mounts on the back end of the SIPT magnet. A long copper arm connects to the cold head and extends into the magnet bore to the cryogenic electronics, resonator circuit, and Penning trap. Inside the SIPT detection box, a copper box connects to the 45 K stage and surrounds the cold head, blocking the sightline from the 4.2 K stage to the room temperature surroundings. The 45 K stage also connects to a long hollow copper tube with a removable lid. This tube extends through the magnet bore and acts as both a 45 K shield and a bench to hold all of the experimental components that sit inside the magnet, including the cryogenic detection electronics, Penning trap electrode system, and the ion injection optics.

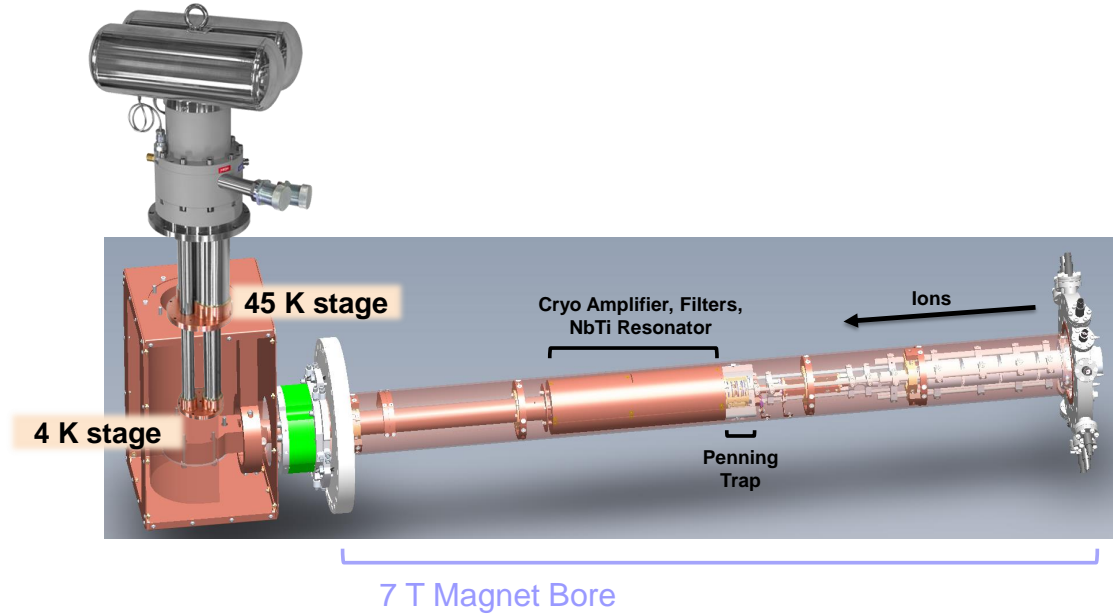


Figure 5.8: Overview of the SIPT cryogenic system components.

5.3.1.4 TOF-ICR Detection

SIPT was designed to allow standard TOF-ICR detection in addition to FT-ICR for measurements and optimization. Central to this flexible, multi-use design is the execution of reverse ion extraction. As in the 9.4-T Penning trap, ions delivered to SIPT pass through a set of injection optics including a Lorentz steerer [50], which prepares the ions in an initial magnetron motion in the Penning trap. A quadrupole RF drive is then applied to convert the slow magnetron motion into fast modified cyclotron motion. Unlike the 9.4-T system, however, ions in the SIPT trap cannot be ejected out the opposite side of the trap from which they were injected. Instead, when TOF-ICR detection is desired, the ions must be extracted in the same direction from which they entered the trap and pass through the same injection optics in the opposite direction, before they are detected on an MCP detector in a Daly configuration just outside the magnet bore at SIPT BOB3.

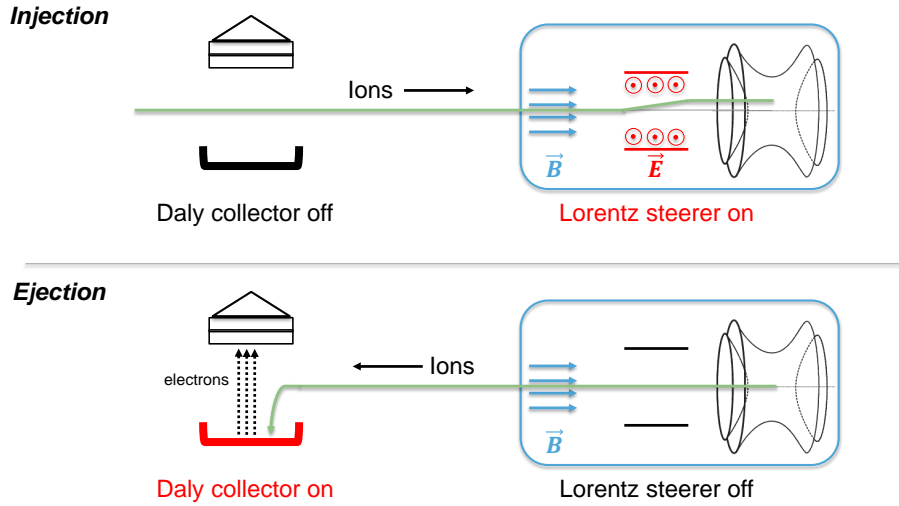


Figure 5.9: Conceptual overview of reverse ion extraction for TOF-ICR measurements with SIPT.

The concept of TOF-ICR detection with reverse extraction is presented in Fig. 5.9. The key difference from the 9.4-T TOF-ICR setup, aside from changing the direction of the ions' motion after trapping, is that the Lorentz steerer voltages and the Daly collector voltage must be switched when the ions are ejected from the trap. On injection into the Penning trap, the Lorentz steerer should steer the ions off-center to prepare the initial magnetron motion. On ejection from the Penning trap, the Lorentz steerer must be switched to allow the ions to pass by without changing course. Conversely, the Daly collector should be set to allow ions to pass by unimpeded on injection, but must be switched to a more negative voltage on ejection from the Penning trap so that the ions are collected there for detection.

5.3.1.5 FT-ICR Detection Circuit Design

Single-ion FT-ICR detection requires careful circuit design consideration to create as strong of a signal as possible while minimizing noise. Certain stages of the circuit must also operate inside the 7-T SIPT magnet and at cryogenic temperatures, requiring additional design

4K

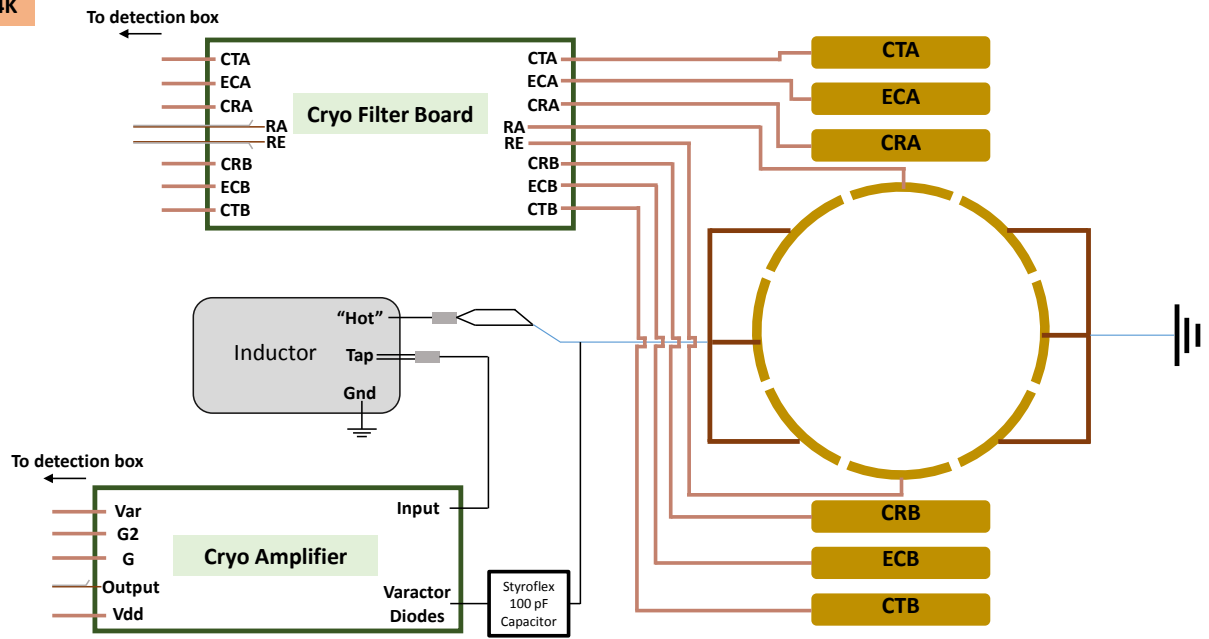


Figure 5.10: Schematic circuit diagram of the SIPT cryogenic filtering and detection electronics.

considerations to ensure performance does not degrade in this extreme environment. The detection electronics were purchased from Stahl Electronics due to their experience and expertise in electronics design and manufacturing for similar ion trap projects.

A schematic of the SIPT cryogenic detection circuit is presented in Fig. 5.10. The image current detection scheme is determined by the wiring of the eight ring electrode segments (see the discussion of multipolar FT-ICR detection schemes in Section 2.4). For first tests of FT-ICR detection with SIPT, the trap has been wired for dipole pickup of ν_+ . Three adjacent ring segments were jumped together to provide ample electrode surface area for image current pickup. The three adjacent segments opposite the pickup segments were grounded for signal reference. In principle, a stronger ν_+ signal could be obtained by using these segments for signal pickup as well and connecting the opposite sides of the trap to a differential amplifier, as is done for room-temperature FT-ICR pickup with MiniTrap. However, Stahl Electronics

has found from past experience that the single-input cryogenic amplifier they provided for SIPT performs far better than their differential amplifiers, so only a single section of the trap ring is used for signal pickup. The remaining two ring segments are used for the RF signals needed to drive the ions' motion.

A tunable superconducting RLC resonator circuit is then used to improve the quality of the image current signal. The general form of Ohm's law in an AC circuit is

$$V = I * |Z|, \quad (5.3)$$

from which it clearly follows that even a very small current source can generate a substantial voltage signal if the overall circuit impedance is sufficient. In a parallel RLC circuit, the absolute value of the impedance is given by

$$|Z(\omega)| = \frac{Q\omega L}{\sqrt{1 + Q^2 \left(\frac{\omega^2}{\omega_{circ}^2} - 1 \right)^2}}. \quad (5.4)$$

We can see from this equation that the maximum $|Z|$, and therefore the maximum voltage signal, is achieved when $\omega = \omega_{circ} = 1/\sqrt{LC}$. At this value, the impedances due to the circuit capacitance and inductance cancel each other out the only remaining impedance is the parallel resistance, given by

$$|Z(\omega = \omega_{circ})| = R_p = Q\omega_{circ}L = \frac{Q}{\omega_{circ}C}. \quad (5.5)$$

Several important circuit design considerations follow from Eq. (5.5). First, when choosing L and C to match ω_{circ} with the expected ICR frequency, it is desirable to make L as large

as possible and C as small as possible. Typically the total capacitance C , which includes the capacitance from the trap electrodes as well as stray capacitances from the wires and amplifier input, can be limited to ~ 20 pF, requiring an inductance on the order of hundreds of μH for typical ν_+ and ν_c values of singly-charged ions in a 7 T magnetic field.

Eq. (5.5) also demonstrates that it is important to make the circuit quality factor Q as large as possible. To this end, a superconducting NbTi coil is used for the inductor, reducing the series resistance across the coil to zero when cooled below the critical temperature. By definition, a large Q means a narrow frequency response (Eq. 5.2), suppressing all noise outside this narrow band where the FT-ICR signal is expected.

The center frequency of the resonator circuit must also be tunable to match the expected ICR frequency of the ion to be measured. The tunable range of a given resonator must cover several atomic mass units to ensure that a stable reference mass is available for magnetic field calibrations and to allow tuning through the beamline with an isotope closer to stability before switching to the isotope of interest. To achieve this, the cryogenic amplifier from Stahl Electronics is equipped with two gallium-arsenide high-Q varactor diodes in parallel at the input of the amplifier. These varactor diodes have a voltage-dependent capacitance, with a nominal range of 2.4 pF to 14 pF. This provides approximately a $\pm 8\%$ tuning range.

The cryogenic amplifier utilizes state-of-the-art GaAs FET technology to provide low noise amplification at 4.2 K. The nominal linear voltage gain for the cryogenic amplifier is $\sim 11\times$. To minimize noise pickup on the wires, this amplifier is kept as close as possible to the Penning trap. It was tested by the manufacturer at temperatures of 4 K with no magnetic field and in magnetic fields up to 6 T at 10 K and demonstrated no loss of performance in these conditions.

The output from the cryogenic amplifier is delivered by cryogenic coaxial cable to a room

temperature A7-2 amplification module, also provided by Stahl Electronics. The amplification of this module can be set by the user in four discrete steps: 20x, 40x, 100x, or 200x. The A7-2 also provides stable, low-noise DC supply voltages to the cryogenic amplifier and monitors the biasing conditions. An internal PID loop adjusts the supply voltages as needed, and LED indicators provide feedback to the user to analyze possible malfunctions and cabling problems in the cryogenic region.

5.3.2 Controls and Data Acquisition

Initial tests of FT-ICR detection with SIPT used an SR1 audio analyzer from Stanford Research Systems to complete the FTT analysis. The time-domain signal from the room temperature amplifier was first sent to a low-noise frequency mixer, which subtracts a given local oscillator frequency from the entire signal. This frequency mixing shifts the ion signal to a much lower frequency, allowing high-resolution signal sampling with less data. The time-domain output of the frequency mixer was then sent to the SR1 for FFT analysis, and the frequency-domain output from the SR1 was saved to a LEBIT computer.

For online beam experiments, it will not be desirable to use the SR1 because the data transfer rates are limited by the hardware and would introduce serious dead time in the measurement process. Instead, the time-domain signal from the room temperature amplifier will be delivered to a PXI-5114 oscilloscope from National Instruments, which currently processes the ion signals used for TOF-ICR detection at LEBIT. A near-term future project will be to write analysis code to process this time-domain signal. As most data in an extremely low-rate beam experiment will be devoid of any ion signal, an important component of this analysis code will be setting thresholds to determine in real time if an acquired signal contains ion signatures. Potentially useful data will be saved, and blank data will be deleted to

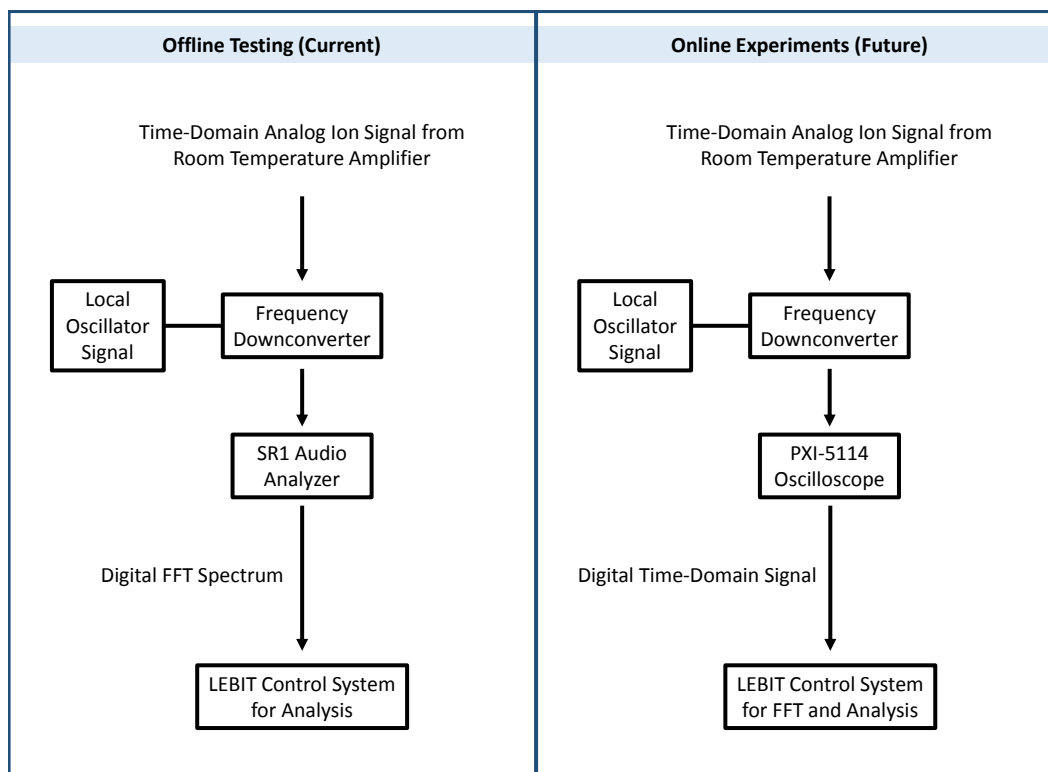


Figure 5.11: Flowcharts outlining the SIPT data acquisition process currently used for offline testing (left) and that envisioned for future online experiments (right).

avoid taking up hard drive space. Ultimately this readback for FT-ICR data will be incorporated into the Mass Measurement software package used for TOF-ICR live data acquisition. A flowchart outlining the data acquisition process currently used for offline testing and that envisioned for future online experiments is presented in Fig. 5.11.

A description of the controls and data acquisition system currently used at LEBIT can be found in the appendices of Ref. [116]. SIPT controls have been incorporated into the LabVIEW-based server used to communicate with LEBIT hardware. This includes all of the beamline components such as power supplies, vacuum pumps, and gate valves, as well as the AFGs used to drive the ions' motion and the AFG used as the local oscillator for the frequency mixer. Screenshots of the Qt-based user interface used for SIPT controls are presented in Fig. 5.12.

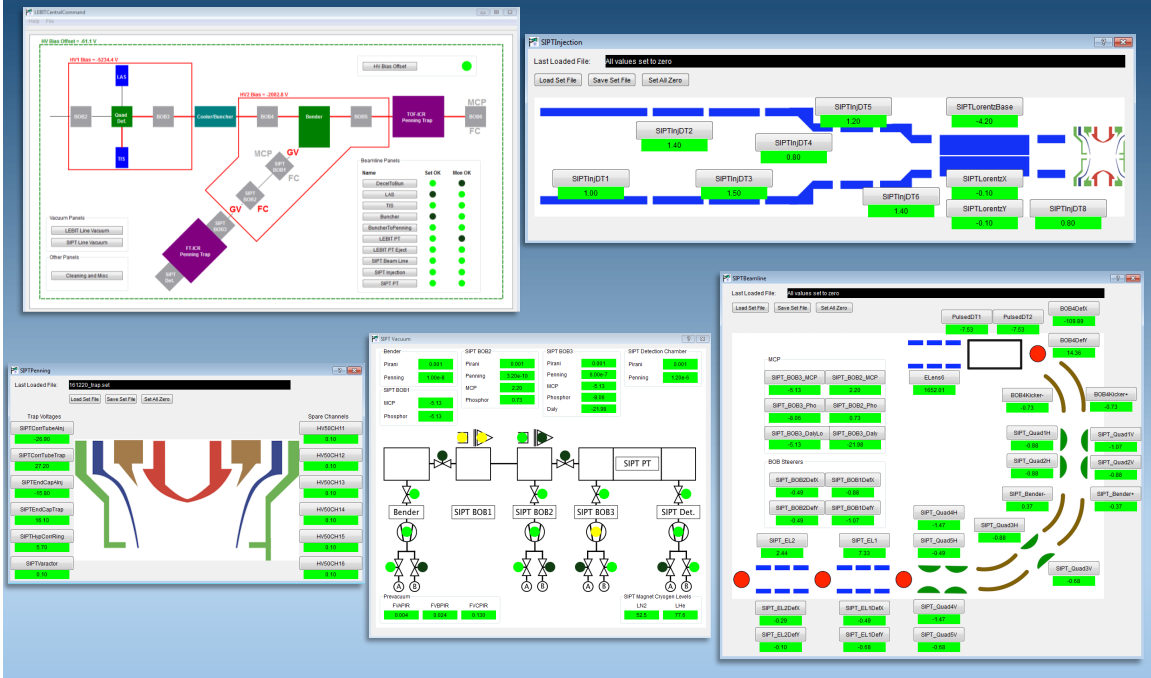


Figure 5.12: Screenshots of the Qt-based user interface used for control of SIPT hardware devices including power supplies, AFGs, vacuum pumps, and gate valves.

5.4 Offline Commissioning of the Single Ion Penning Trap

5.4.1 Room Temperature Commissioning

The first tests of the Single Ion Penning Trap were performed at room temperature, using stable $^{39}\text{K}^+$ ions from the LEBIT thermal ion source to test ion transport, trapping, TOF-ICR detection, and broadband FT-ICR detection with a large number (~ 1000) of trapped ions.

The SIPT beamline components performed well as expected from the beam optics simulations discussed in Section 5.2. $\sim 95\%$ ion transport efficiency was observed around the 115° bend (from BOB4 to SIPT BOB2) with minimal adjustment from the simulated electrode potentials. This transport efficiency was determined by comparing Faraday cup ion current

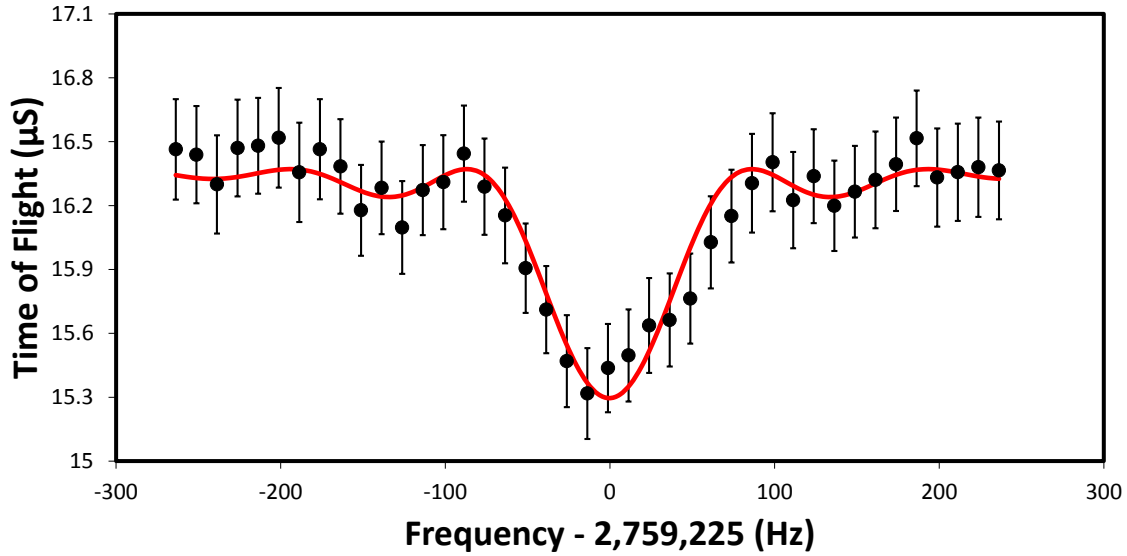


Figure 5.13: 10 ms TOF-ICR resonance of ν_c for $^{39}\text{K}^+$ using reverse ion extraction from the SIPT Penning trap to the SIPT Daly MCP.

measurements.

The first trapped ions with SIPT were observed using the reverse extraction method discussed in Section 5.3.1.4. Ions were injected into the Penning trap, trapped for 40 ms, and then ejected in the same direction they entered and observed on the Daly-configuration MCP at SIPT BOB3. TOF-ICR detection was then demonstrated by applying an RF drive signal to a single ring segment for 10 ms, scanning the RF frequency around ν_c and measuring the time-of-flight to the Daly MCP. The resulting TOF-ICR resonance is presented in Fig. 5.13.

To test FT-ICR detection at room temperature, the narrowband detection circuit was bypassed and the room temperature differential amplifier used for MiniTrap was connected to the trap pickup electrodes. The output of the amplifier was then sent through the frequency mixer and finally the SR1 audio analyzer was used for FFT analysis. A dipole image charge pickup scheme was used to detect the modified cyclotron motion. Once ions were trapped,

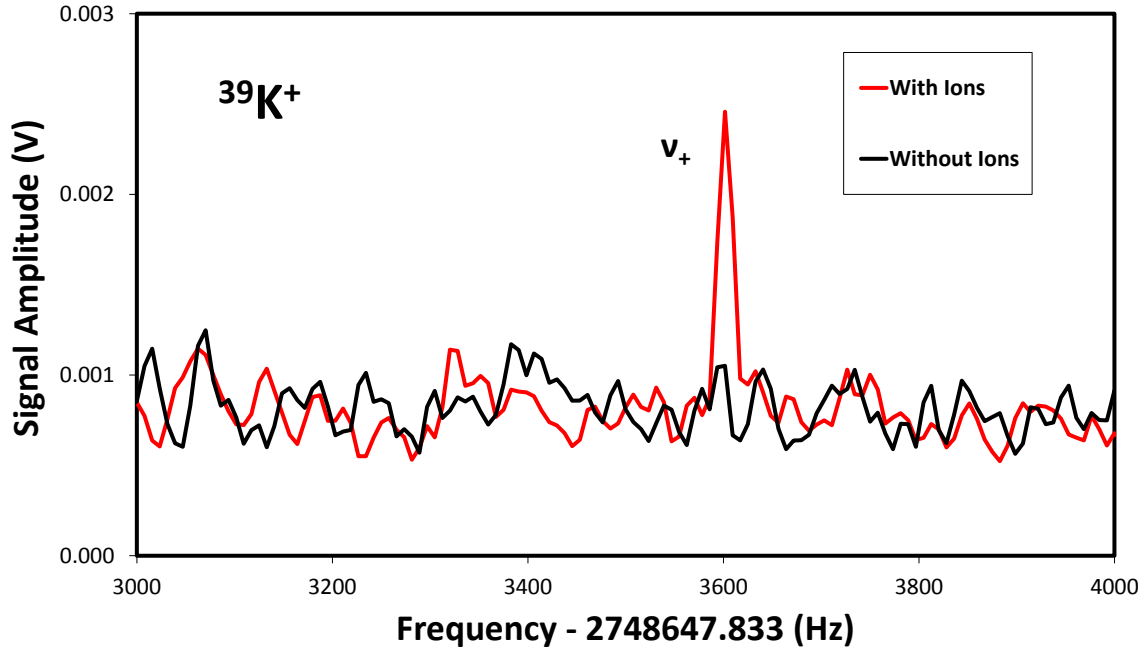


Figure 5.14: Demonstration of broadband FT-ICR detection with SIPT at room temperature. The ion peak seen in this figure comes from picking up the image current generated by the modified cyclotron motion of many (~ 1000) $^{39}\text{K}^+$ ions. The data presented here is the average of five consecutive shots, each of which used a 256 ms acquisition time.

an RF excitation was applied at ν_+ to drive the modified cyclotron motion to a larger radius, pushing the ions closer to the trap electrodes to increase the image charge pickup. In this manner, a strong ν_+ signal was observed in the frequency spectrum on the SR1. An example of the room temperature FT-ICR resonances obtained in this manner is presented in Fig. 5.14.

5.4.2 Cryogenic Commissioning

5.4.2.1 Cooling to 4 K

Once room temperature detection was successfully completed, the next step was to incorporate the cryogenic system required for single ion detection. As discussed in Section 5.3.1.3, the SIPT cryogenic system requires good thermal conductivity across the 4 K stage and

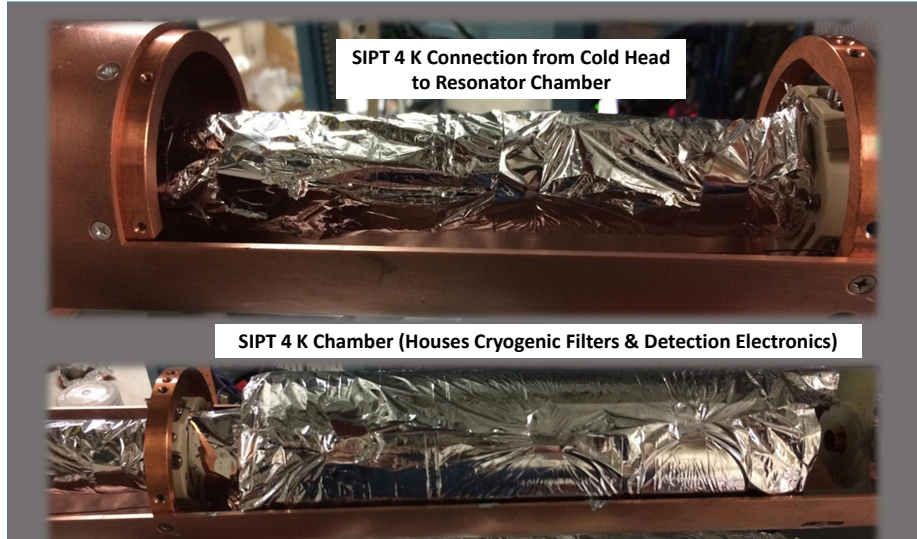


Figure 5.15: SIPT 4 K stage wrapped in Mylar to reduce radiative heating from the surrounding 45 K stage. Two layers of Mylar wrapping were necessary to reach temperatures of ~ 4 K.

thermal insulation from room temperature to ensure that the cryogenic components inside the magnet reach and maintain sufficiently low temperature. Particularly important is the NbTi resonator, which must remain below the critical temperature T_c (approximately 6 K in a 7 T magnetic field) to remain in a superconducting state. To test this, Cernox cryogenic temperature sensors were attached at various locations along the SIPT cryogenic stages to monitor the temperature after the cryocooler was turned on.

On the first cool-down trial, the temperature at the center of the magnet (near the trap and resonator circuit) only reached 9.8 K, although the temperature at the cold head got as low as 7.1 K. To improve the thermal conductivity to the center of the magnet, Apiezon N cryogenic high-vacuum grease was applied to the joints where separate copper pieces join. To minimize radiative heating from the outer 45 K stage, the 4 K stage was wrapped in two layers of Mylar, with an insulating mesh layer separating the two layers of Mylar. A picture of the 4 K stage wrapped in Mylar is shown in Fig. 5.15. In combination, these changes were sufficient to allow the region at the center of the magnet to reach ~ 4.5 K.



Figure 5.16: 600 μH NbTi inductor coil (left) and NbTi inductor case (right) used for the high-Q SIPT FT-ICR detection circuit. The inductor coil consists of 194 turns of 250 μm NbTi wire with tubular Teflon coating wrapped around a Teflon core. The windings were then covered by an additional layer of Teflon tape, which provides both mechanical support and some additional amount of thermal conductivity.

The cryogenic detection electronics were then installed. The NbTi inductor quality is diminished by the presence of non-superconducting metals, so the coil is wrapped around a PTFE bobbin and housed within a NbTi case. A PTFE screw is used to mount the bobbin to the resonator case. Apiezon N grease was applied at all junctions to improve thermal conductivity. Pictures of the NbTi inductor coil and case are presented in Fig. 5.16.

The cryogenic amplifier and cryogenic filter board were mounted to copper backings in the region between the Penning trap electrode system and the NbTi resonator case. All of the wire connections from the 4 K stage for DC voltage application use constantan wire to minimize heat transfer from room temperature. These wires were run along 4 K surfaces and then 45 K surfaces before reaching the room temperature feedthroughs to keep the wires as cold as possible. RF signals require better electrical conductivity, so cryogenic coaxial cable (type CC-SR-10) was used for the connections from the output of the cryogenic amplifier and for the RF ion drive signals. A picture of the wired 4 K components is presented in

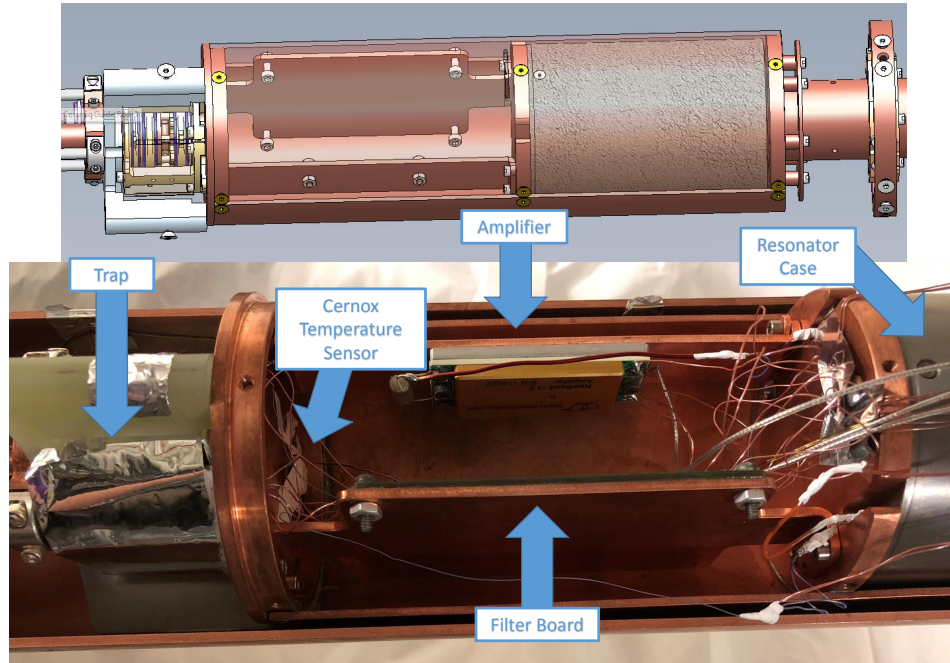


Figure 5.17: SIPT 4 K chamber with all components mounted and wired (bottom). The design drawing of this region is included for reference (top).

Fig. 5.17.

Once all cryogenic components were installed, wires were run to monitor the resistance across the inductor coil as the temperature dropped. As demonstrated in Fig. 5.18, after the trap region of the 4 K stage reached its minimum temperature, it took several more hours for the NbTi coil to cool below its critical temperature. After another 12 hours, however, this threshold was crossed and the resistance dropped to nearly 0Ω . Residual resistance is most likely due to slight differences in the length of constantan wire leads connected to opposite ends of the inductor coil.

5.4.2.2 Resonator Circuit Response

The response of the resonator circuit was then tested at cryogenic temperatures by feeding in 20 mV_{pp} noise over a 2 MHz bandwidth to one of the RF drive segments of the trap's

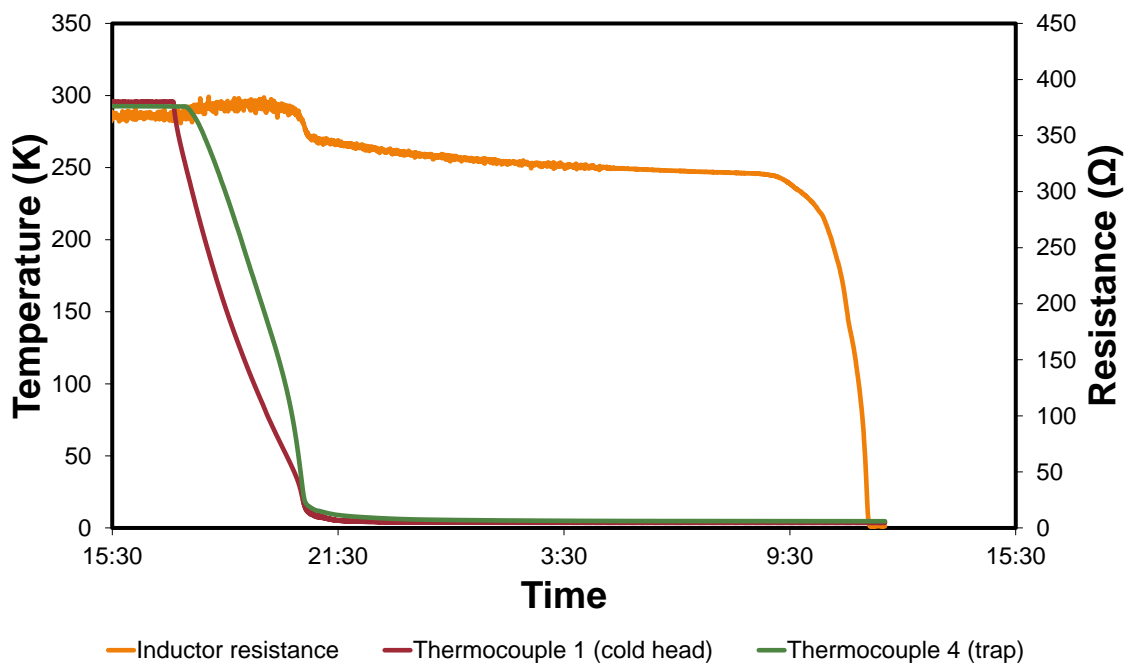


Figure 5.18: Resistance across the NbTi inductor coil plotted over time alongside the temperature readings from the Cernox temperature sensors mounted on the cold head and the back of the SIPT Penning trap. Roughly 12 hours after the temperature sensors reached their minimum values, the NbTi coil cooled below its critical temperature and entered a superconducting state, as evidenced by the resistance drop to nearly 0 Ω .

ring electrode. The output frequency spectrum was observed using the SR1 audio analyzer. Two unexpected difficulties were observed while testing the resonator in this manner. First, the combination of high magnetic field and low temperatures affected the quality factor of the varactor diodes used to tune the center frequency of the resonator. This greatly reduced the overall quality factor of the resonator when the varactor diodes were connected. Second, when the varactor diodes were disconnected to achieve a high quality factor, a very tall and narrow peak was observed right at the center frequency of the circuit. This peak appeared to be some sort of self-excitation of the detection electronics, as it remained even when no noise or driving signal was fed into the trap.

Both of these difficulties have been temporarily mitigated to proceed with cryogenic testing, and potential long-term solutions have been examined as well. For initial cryogenic tests with SIPT, the varactor diodes have been disconnected and replaced with fixed-value high-Q polystyrene capacitors. The values of these capacitors were carefully selected to place the center frequency of the resonator circuit as close as possible to the expected ν_+ frequency of $^{85}\text{Rb}^+$, which is readily available from the LEBIT thermal ion source. Additional fine-tuning was accomplished by adjusting the trapping potential to shift ν_+ according to Eq. 2.5 so that ν_+ is equal to ν_{circ} .

Stahl Electronics was contacted to discuss long-term fixes for the varactor diode issue as well. The response was that, although previous batches of these varactor diodes from the same manufacturer had not shown this issue, the current batch had shown similarly poor behavior elsewhere. The other group that experienced these issues found that the issue could be resolved by slightly elevating the temperature of the diodes. The Stahl team has therefore delivered a small, thermally insulated printed circuit board with additional varactor diodes and resistors for heating. The idea is that this board will be mounted on the 4 K stage

near the cryogenic amplifier and slightly heated by the resistors until the varactor diodes are sufficiently warm that the high Q is restored. Of course, this relies on sufficient thermal isolation to ensure the NbTi inductor is not warmed to a point where superconductivity is lost. This will be tested in the near future. Another potential long-term solution for tuning the resonator circuit is to use a variable plate capacitor which is mechanically tuned by rotation using a 4-K piezo drive. This option would allow very high Q factors, but would also require more significant modifications to the current system.

The resonator self-excitation peak was also found to be temperature-dependent, and it could be eliminated by slightly elevating the temperature of the entire 4 K stage using a heater resistor mounted to the cold head without raising the temperature sufficiently high to destroy the superconductivity. Alternatively, the self-excitation peak could mostly be eliminated by turning off the A7-2 PID control of the cryogenic supply voltages and manually adjusting the auxiliary biasing voltage by a small amount. This could be a bit risky, however, as there is only a very small window over which the supply voltage eliminates the self-excitation peak and does not exceed the acceptable supply voltage range. Without the PID loop on, it is possible that slight temperature fluctuations could bring back the self-excitation peak or push the supply voltage into a range that degrades the cryogenic amplifier performance. Additional testing and experience will likely determine whether elevating the temperature or manually adjusting the cryogenic supply voltage is the better option for eliminating the self-excitation peak.

For initial cryogenic testing, the temperature of the 4 K stage was elevated to ~ 5.2 K to eliminate the self-excitation peak. The resonator response observed at this temperature on the SR1 is shown in Fig. 5.19. A very clear, narrow resonance peak is observed at a center frequency very near the expected ν_+ frequency of $^{85}\text{Rb}^+$, and the resonator Q factor found

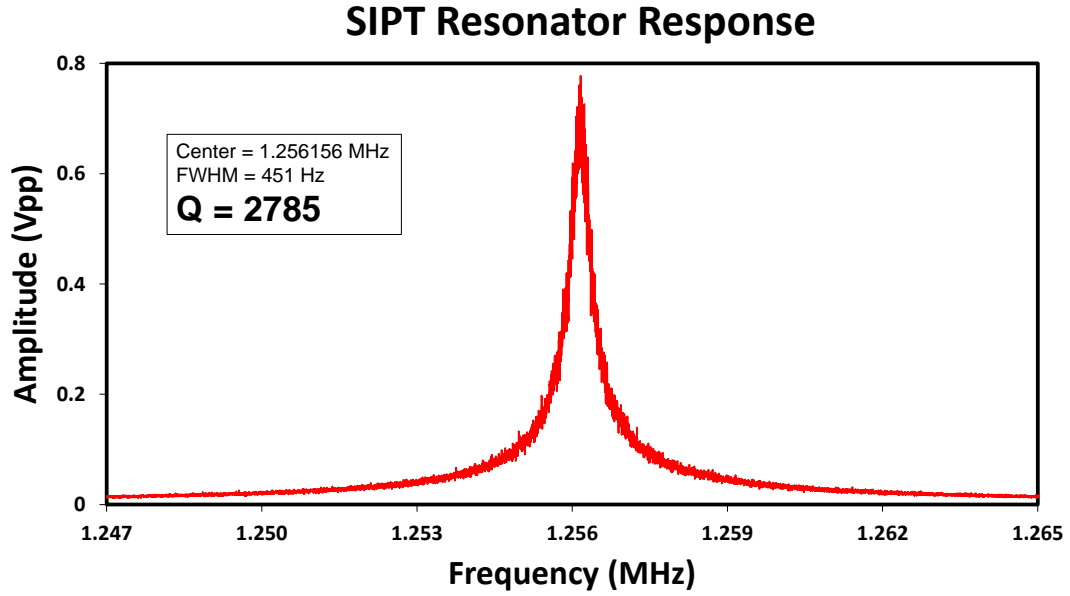


Figure 5.19: Frequency domain response of the SIPT narrowband FT-ICR cryogenic detection circuit operating at ~ 5.2 K. This very narrow frequency response corresponds to a circuit Q factor of 2785, which is greater than what is required for single ion detection.

from fitting this peak with a Lorentz function is $Q = 2785$, exceeding the Q factor of ~ 2000 advertised by the manufacturer. With such a response, single ion detection should be well within reach.

Chapter 6

Summary and Outlook

The first Penning trap mass measurements of ^{68}Co and ^{69}Co were completed at LEBIT, reducing the atomic mass uncertainties by more than an order of magnitude from the AME2016 data, allowing for detailed studies of nuclear structure in the area near $Z = 28$ and $N = 40$. Although further studies are needed to definitively establish the ordering of the two β -decaying states in $^{68,69}\text{Co}$, no evidence for a substantial subshell closure across $N = 40$ was observed in the $_{27}\text{Co}$ isotopes, consistent with S_{2n} studies already completed for $Z \geq 28$.

In order to greatly extend LEBIT's reach on the nuclear chart to exotic isotopes far from stability, the Single Ion Penning Trap has been developed. SIPT uses the non-destructive narrowband FT-ICR technique to allow complete mass measurements with a single ion. No such device has yet been employed at a rare isotope facility. When SIPT comes online, it will enable precise mass measurements of species far from stability where production rates are extremely low. This will provide a path to explore the role of magic numbers far from stability by exploring mass trends in the vicinity of magic and doubly-magic nuclei such as ^{78}Ni and ^{100}Sn .

A new Penning trap and accompanying beamline were designed and commissioned for SIPT at the LEBIT facility. TOF-ICR and broadband FT-ICR detection were demonstrated with great success at room temperature. A highly sensitive cryogenic resonating detection circuit was then added and tested. The detection circuit now demonstrates excellent behavior

compatible with precision measurements at single-ion sensitivity.

Single-ion FT-ICR detection with stable ions is expected in the coming weeks. The extension to radioactive species is then relatively straightforward, as SIPT is already set up to take full advantage of the beam production, stopping, and preparation facilities currently used for mass measurements with LEBIT at the NSCL.

With the 9.4-T TOF-ICR Penning trap producing valuable scientific results like the cobalt measurements presented in this thesis and the 7-T SIPT system now being commissioned, LEBIT is very well positioned to extend its already well-established program of precise, accurate mass measurements of rare isotopes. As FRIB reaches completion in the next few years, LEBIT will be well-poised to take full advantage of the many opportunities for cutting-edge new rare isotope research.

APPENDICES

Appendix A

Characterization of the MiniTrap

Magnetometer

LEBIT has previously demonstrated the ability to perform successful narrowband FT-ICR measurements with the development of the MiniTrap magnetometer [117]. MiniTrap is a cylindrical Penning trap currently housed in the 9.4-T LEBIT magnet just downstream from the primary LEBIT hyperbolic Penning trap and slightly off of the main beam axis. Rather than measuring rare isotopes delivered from the cyclotron facility or stable isotopes from one of the LEBIT offline sources, MiniTrap includes a self-contained electron gun which ionizes residual background gas to generate ions within the trap volume. FT-ICR resonances of these ions can then be used to track changes in the magnetic field at a high level of precision.

The ultimate aim of this project is to eliminate the need to perform reference measurements in the main hyperbolic trap during online experiments. Instead, MiniTrap can be used to perform reference measurements of stable background gas ions simultaneous to rare isotope measurements in the main hyperbolic trap. This would provide two important advantages: tracking non-linear magnetic field fluctuations and making the most use of valuable beam time. The current system of alternating rare isotope measurements with reference measurements to track changes in the magnetic field relies on a linear interpolation between reference measurements to determine the magnetic field strength at the time of the

rare isotope measurement. While non-linear changes in the magnetic field have been shown to contribute to the overall systematic mass uncertainty only on a level of $\sim 10^{-10}$ [63], MiniTrap could be used to eliminate this uncertainty altogether and monitor for unexpected spikes or anomalous field deviations. Perhaps more importantly, MiniTrap could eliminate the need to pause rare isotope measurements to take occasional reference mass measurements in the main hyperbolic trap. Online beam time at the NSCL is highly competitive and total operating costs are quite large, so eliminating the need to pause the delivery of rare isotopes to LEBIT during online operation would be a valuable contribution.

MiniTrap was originally tested in an isolated environment and performed well, monitoring magnetic field fluctuations at a relative precision of $\sim 10^{-8}$. H_3O^+ was identified as the primary residual gas component ionized by the MiniTrap electron gun. A screenshot of an FFT spectrum from these first tests of MiniTrap, reproduced from Ref. [117], is presented in Fig. A.1. Frequency components from both the true cyclotron and modified cyclotron motions can be seen in this spectrum.

Tests of MiniTrap in the 9.4-T LEBIT magnet

When MiniTrap was moved to its current location in the 9.4-T LEBIT magnet, additional tests were required to determine the optimal parameters for producing, driving, and detecting ions in the new environment. Broadband detection was initially used to detect the ions' magnetron motion, and the modified cyclotron frequency was then determined with a dipole cleaning scan. The results of this scan are shown in Fig. A.2. When the ions' modified cyclotron motion was excited at the correct frequency ν_+ , the ions were driven into the walls of the trap and lost, resulting in a reduction in the amplitude of the detected magnetron

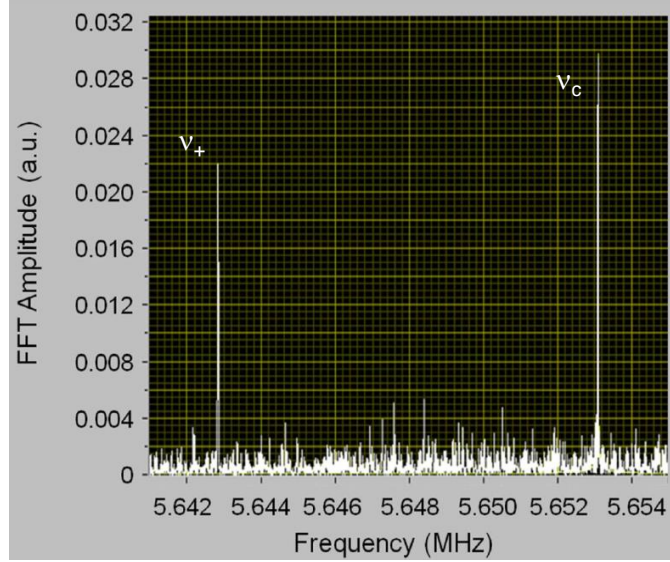


Figure A.1: A LabVIEW screenshot of FFT resonances of both modified cyclotron motion (left) and true cyclotron motion (right) of H_3O^+ ions measured with the MiniTrap magnetometer using a broadband FT-ICR quadrupole detection configuration.

signal.

Next a series of “trap tuning” scans were performed. Keeping the trap depth U_0 (the potential difference between the endcap and ring electrodes) fixed, the ratio of the endcap and ring electrode voltages was varied to determine the settings which best approximated a true quadrupolar electrostatic potential. For each voltage ratio, an RF excitation was applied near the modified cyclotron frequency ν_+ and the frequency of the detected ν_+ signal in the FFT was recorded as a function of the applied RF excitation amplitude. As the RF amplitude increased, the ions were driven to larger radii. The results of these scans are presented in Fig. A.3. An endcap potential of 9.15 V and a ring voltage of -1.25 V were chosen because, at these settings, the measured frequency showed the least variance as the ions were driven to increasingly large radii, indicating a good approximation of a true quadrupolar electrostatic potential.

The optimal frequency and amplitude for RF excitation of the modified cyclotron motion

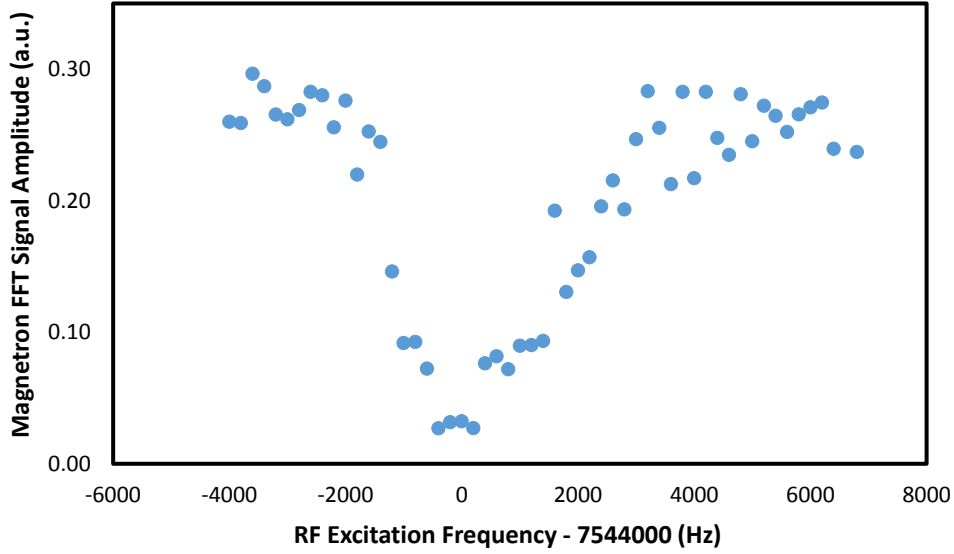


Figure A.2: Results of the dipole cleaning scan used to determine the modified cyclotron frequency ν_+ of ionized background gas molecules in the MiniTrap magnetometer after it was moved to its current location in the 9.4-T LEBIT magnet.

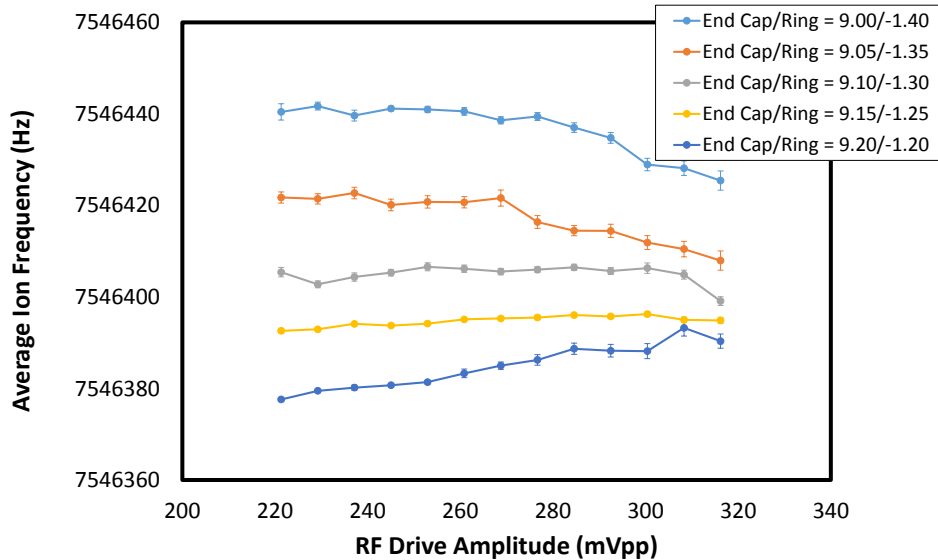


Figure A.3: MiniTrap tuning scans used to determine the optimal ratio between the endcap and ring potentials. The trap depth was held constant at 10.4 V. A ratio of 9.15 to -1.25 between the end cap and ring potentials was found to produce the best approximation of a quadrupolar electrostatic potential because, at these settings, the measured ion frequency varied the least as the ions were driven to increasingly large radii.

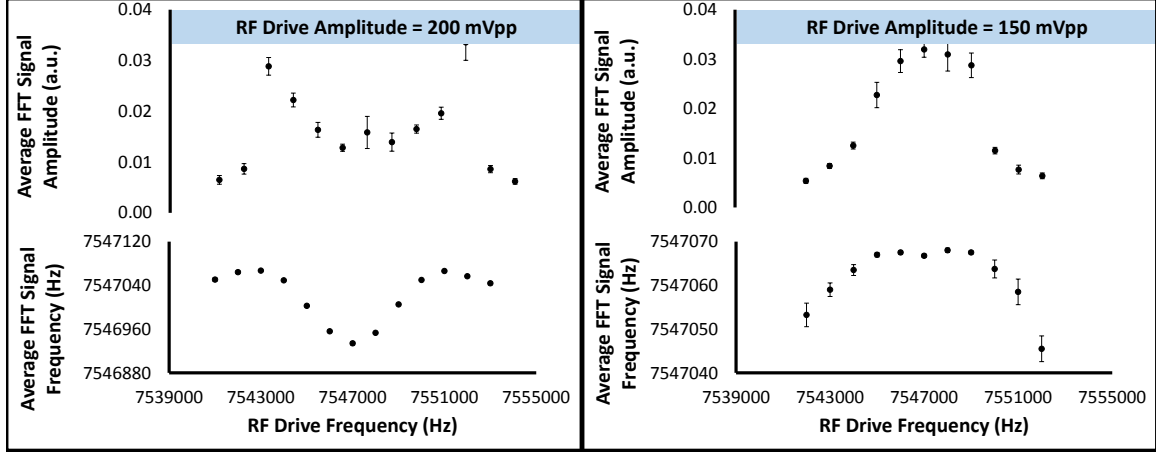


Figure A.4: Amplitude (top) and center frequency (bottom) of the ν_+ peak in the FFT spectrum as a function of the applied RF excitation frequency. The plots on the left were obtained with a 200 mVpp RF excitation and the plots on the right were obtained with a 150 mVpp RF excitation. The observed behavior is discussed in the text.

were determined by measuring the frequency and amplitude of the FT-ICR signal at ν_+ as a function of the RF frequency, as shown in Fig. A.4. When the RF amplitude was too large and the RF frequency matched ν_+ , the ion cloud was driven towards the walls of the trap, shifting the measured frequency and reducing the FFT amplitude. When the RF amplitude was set to a more appropriate value, the FFT amplitude was maximized when the RF frequency matched ν_+ and the measured frequency remained constant over a wide range of applied RF frequencies in the vicinity of ν_+ .

A new resonator circuit also had to be built for narrowband FT-ICR detection with MiniTrap in the 9.4-T LEBIT magnet. In fact, two new resonator circuits were built, one for detection of the modified cyclotron motion and one for detection of the true cyclotron motion. The modified cyclotron motion detection circuit is wired for dipole pickup and tuned to resonate near ν_+ , while the true cyclotron motion detection circuit is wired for quadrupole pickup and tuned to resonate near ν_c . The two resonators can easily be exchanged to switch between detection of the two motions. Unlike SIPT, the MiniTrap resonators are non-

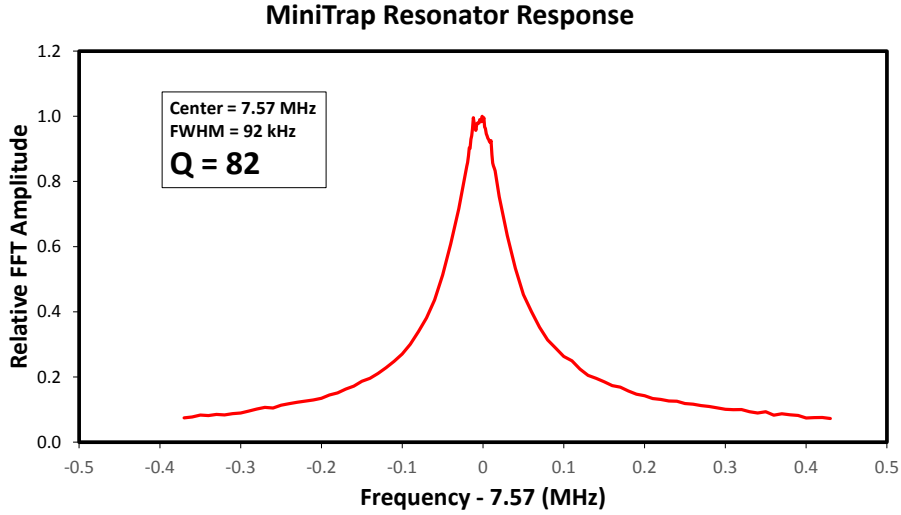


Figure A.5: Frequency domain response of the MiniTrap room temperature resonant circuit used for narrowband FT-ICR detection of the true cyclotron motion of trapped H_3O^+ ions.

superconducting and operate at room temperature. The frequency domain response of the true cyclotron motion detection circuit is presented in Fig. A.5. This resonator has a quality factor Q of ~ 82 . The center frequencies of the MiniTrap resonators can be adjusted by hand with a rotary variable capacitor.

MiniTrap Status

After the initial development and successful testing of MiniTrap documented in Ref. [117], MiniTrap was installed at its intended location in the 9.4-T LEBIT magnet. FT-ICR signals have been observed from H_3O^+ ions at ν_- , ν_+ , and ν_c , and new resonator circuits were built for narrowband detection of the modified cyclotron and true cyclotron motions. Optimal settings for FT-ICR detection have been determined from an extensive series of parameter scans.

Recent attempts to benchmark MiniTrap's ability to monitor magnetic field fluctuations against measurements with the main TOF-ICR trap proved less successful than the previous

tests (which were conducted in a more isolated environment), tracking the magnetic field only at a relative precision of $\sim 10^{-6}$ due to shot-to-shot frequency variations. Tests are currently underway to identify the causes of these variations and eliminate the causes or mitigate the effects to achieve the higher level of precision required for scientific use.

Appendix B

Evaluation of Systematic Frequency

Shifts for SIPT

Magnetic Field Uniformity

Spatial uniformity of the magnetic field must be considered to ensure that any systematic frequency shifts due to field inhomogeneity are negligible. In particular, we consider two possible effects: shifts due to trap vibrations caused by the cryocooler, and shifts caused by misalignment between the trap axis and the magnetic field. The former can be estimated by

$$\frac{\Delta\nu_c}{\nu_c} = \frac{dB_{rel}}{dZ} \Delta Z \quad (\text{B.1})$$

where $\frac{\Delta\nu_c}{\nu_c}$ is the relative frequency shift, $\frac{dB_{rel}}{dZ}$ is the gradient of the relative magnetic field strength, and ΔZ is the peak-to-peak amplitude of the trap vibrations. The Oxford magnet specifications indicate that the on-axis field homogeneity over a distance of ± 40 mm from the center of the magnet is < 3.75 ppm. Conservatively taking this inhomogeneity to be 4 ppm over just the central 10 mm of the magnet, this gives a worst-case field gradient of $4 \times 10^{-7}/\text{mm}$. The SIPT cryocooler, discussed in detail in Section 5.3.1.3, does not provide numbers for the expected oscillation amplitude. However, similar two-stage pulse

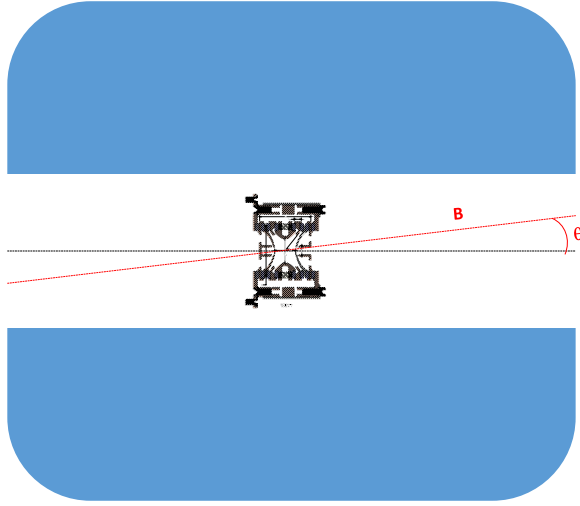


Figure B.1: Illustration of the misalignment angle θ between the magnetic field and the Penning trap axis.

tube cryocoolers specify expected peak-to-peak amplitudes less than $20 \mu\text{m}$, leading to a frequency shift of less than 8 ppb, which is below the level of precision expected for SIPT. Furthermore, these shifts will average out for measurements longer than 17 ms because the cryocooler cycle is 60 Hz.

The potential angular misalignment of the bore axis and the magnetic field, illustrated in Fig. B.1, must also be considered. The Penning trap axis is aligned to the axis of the 40-K copper cylinder which houses all of the experimental components to be inserted into the magnet bore, and this cylinder is in turn aligned to be coaxial with the magnet bore. Thus an angular misalignment between the magnetic field and the bore axis would also lead to the same misalignment with the Penning trap axis, which will systematically shift the cyclotron frequency ν_c . This shift $\Delta\nu_c$ can be approximated by

$$\Delta\nu_c \approx \nu_- \left(\frac{9}{4}\theta^2 - \frac{1}{2}\epsilon^2 \right) \quad (\text{B.2})$$

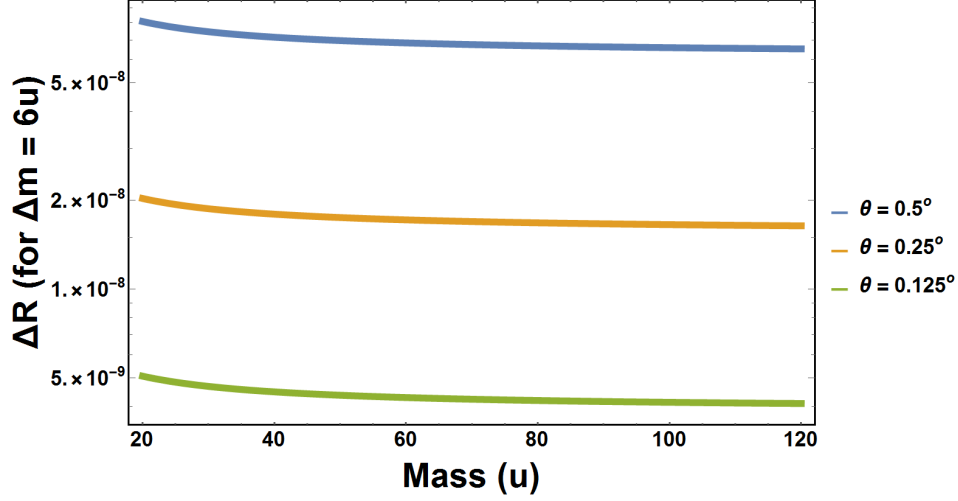


Figure B.2: Frequency ratio shifts due to misalignment between the Penning trap axis and the magnetic field as a function of ion mass, assuming a 6 u mass difference between the ion of interest and the reference ion.

where θ is the magnetic field misalignment as shown in Fig. B.1, ϵ is the trap ellipticity parameter, and ν_- is the ion magnetron frequency [53]. The frequency ratio between the ion of interest and the reference ion used for the final mass determination will then shift by

$$\Delta R = \frac{\nu_{c,1}}{\nu_{c,2}} - \frac{\nu_{c,1} + \Delta\nu_c}{\nu_{c,2} + \Delta\nu_c}. \quad (\text{B.3})$$

Assuming any trap ellipticity is negligible, ΔR was calculated over a wide range of mass values and for a variety of misalignment angles θ . The results are presented in Fig. B.2. Here we have used an extreme case where the mass difference between the ion of interest and the reference ion is 6 u (any larger difference most likely could not be supported by a single resonator). The specifications provided for the Oxford magnet indicate an angular alignment uncertainty of 0.5° . As we see from Fig. B.2, a 0.5° misalignment would result in mass shifts just slightly below 10^{-7} .

To check the actual angular alignment between the magnetic field and the bore tube, an

NMR probe was used to measure the magnetic field at a series of points along the axial planes ± 4 cm from the center of the magnet, at a radius of 2.5 cm. These data were then used to construct a set of radar plots, which are presented in Fig. B.3. From this, the center of gravity was calculated and a shift of only ~ 0.0002 mm was found, corresponding to a misalignment angle of $\theta \sim 0.002^\circ$. As seen from Fig. B.2, any shifts in the mass determination from this tiny misalignment are well below the relevant level of precision expected for SIPT.

Additional frequency shifts could be introduced from imperfect machining or misalignment of the SIPT Penning trap axis and the 40-K copper bore tube insert. These shifts will be evaluated experimentally once SIPT is operational. If necessary, these shifts can be compensated by introducing ellipticity to the trap according to Eq. (B.2).

Special Relativity Effects

Relative shifts in the modified cyclotron frequency due to special relativity are given by

$$\frac{\Delta\nu_+}{\nu_+} = -\frac{1}{2} \left(\frac{qB}{mc} \right)^2 \rho_+^2 \quad (\text{B.4})$$

where c is the speed of light and ρ_+ is the radius of the modified cyclotron motion [38]. Using this equation, frequency shifts from special relativity were calculated for ions of various masses in a 7-T magnetic field as a function of ρ_+ . The results are plotted in Fig. B.4. The inner radius of the SIPT Penning trap electrode system is 6.485 mm, and the simulated data used in Section 5.1 demonstrated that single ion mass measurements are possible with SIPT assuming a radius of $0.5\rho_0 \approx 3.2$ mm. It is clear from Fig. B.4 that, even for relatively light ions, frequency shifts due to special relativity at this radius are below 10^{-7} and therefore are

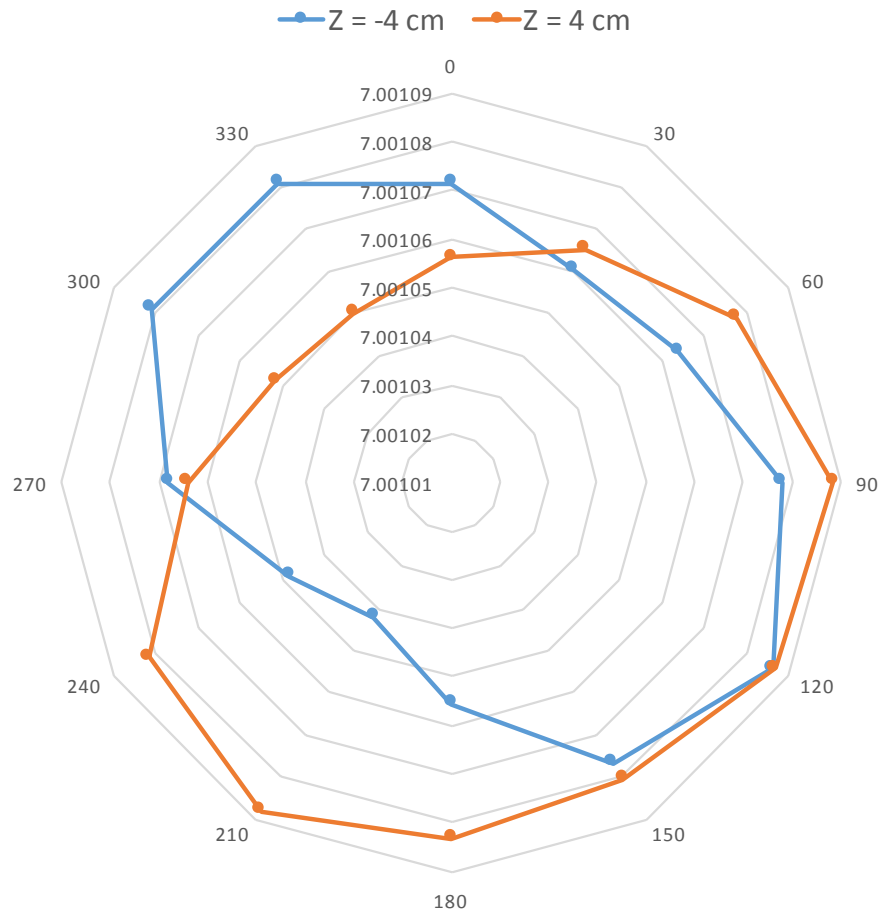


Figure B.3: Radar plots of the magnetic field strength in the SIPT magnet determined from NMR measurements after the magnet was energized.

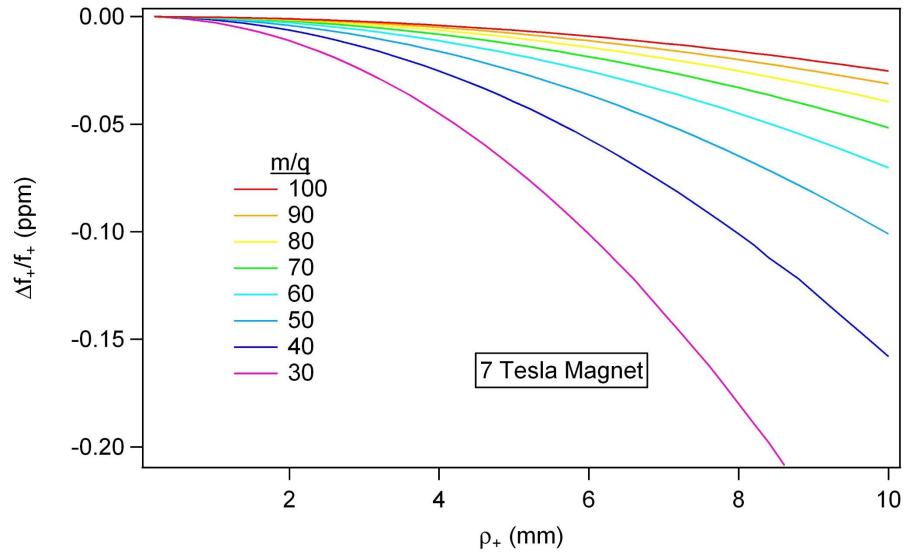


Figure B.4: Relative modified cyclotron frequency shifts due to special relativity plotted as a function of modified cyclotron radius ρ_+ for ions of various masses in a 7-T magnetic field.

unlikely to be relevant at the level of uncertainty expected for SIPT. Moreover, any special relativity shifts will largely cancel out when an ion of similar mass is used for calibration.

Appendix C

Limiting Case Ratio of ^{68}Co

β -Decaying States

As seen in Fig. 4.8, the ^{68}Co gamma spectrum shows clear peaks at 595 keV and 324 keV (associated with decay from the high-spin state) and no clear peak at 478 keV (associated with decay from the low-spin state). The goal of the following calculations is to determine, based on the number of counts observed in the gamma spectrum, a limiting case for what fraction of the ^{68}Co observed at the Penning trap during the mass measurement could have been the low-spin state.

The upper limit of the peak area for the unobserved 478 keV gamma was determined using the method presented in Ref. [118]. The probability of having a peak area a value greater than A is

$$\alpha = \int_A^\infty g(a) da. \quad (\text{C.1})$$

For a mean background value B_0 with standard deviation σ_B , the function $g(a)$ can be approximated as

$$g(a) = N \frac{e^{-(a-\bar{a})^2/2\sigma^2}}{\sqrt{2\pi}\sigma} \quad (\text{C.2})$$

where $\bar{a} = C - B_0$, C is the number of counts in the spectrum over the relevant region,

$\sigma^2 = \sigma_B^2 + C$, and N is a normalization constant such that

$$\int_0^\infty g(a) da = 1. \quad (\text{C.3})$$

A linear fit was used to estimate the background over the relevant region from 360-660 keV, and the data in the regions from 473-483 keV, from 500-520 keV, and from 550-630 keV were excluded from the background fit so that the peaks in these regions would not affect the background determination. The resulting fit was integrated over the region from 473-483 keV to determine the background for the unseen 478 keV peak. The background was found to be $B_0 = 1197$, with an uncertainty $\sigma_B = 50$. The total number of integrated counts over this region is $C = 2333$. Using these numbers, Eq. (C.1) was then solved numerically with $\alpha = 0.32$, corresponding to 68% (1σ) statistical confidence, and the upper limit was found to be $A = 1169$.

This was then compared with the 595 keV peak, which includes 2383 total counts in the region from 590-600 keV and a background of $B_0 = 788$ with an uncertainty $\sigma_B = 56$. For a lower limit on the number of counts in this peak with 1σ confidence, α was set to 0.68, and the lower limit was found to be $A = 1560$.

For an incoming rate r , the production rate of ^{68}Co is given by

$$\frac{dN}{dt} = r - \lambda N. \quad (\text{C.4})$$

Solving this differential equation gives

$$\lambda N = r(1 - e^{-\lambda t}). \quad (\text{C.5})$$

At time $t = 0$, there is no activity. As t goes to infinity, the activity approaches r , and an equilibrium is reached where the rate of decay is equal to the incoming rate. The gamma spectrum used for this work was collected for 2823 s, which is a very long time compared to the half-lives of the high-spin and low-spin β -decaying states of ^{68}Co (0.23(3) s and 1.6(3) s, respectively [88]) so the equilibrium case can be used to determine the number of decays for the low-spin state (state 1) and the high-spin state (state 2) in some amount of time t :

$$N_1 = r_1 t \tag{C.6}$$

$$N_2 = r_2 t \tag{C.7}$$

To determine the expected number of detected gammas at 478 keV and at 595 keV, the number of decays from each state must be multiplied by the absolute intensity I , the detector efficiency at that energy $\epsilon_{det}(E)$, and the geometric efficiency ϵ_{geo} . Taking the ratio of the number of expected gammas at each energy, the geometric efficiency cancels out, leaving

$$\frac{N_{478}}{N_{595}} = \frac{N_1 I_{478} \epsilon_{det,478}}{N_2 I_{595} \epsilon_{det,595}} = \frac{r_1 I_{478} \epsilon_{det,478}}{r_2 I_{595} \epsilon_{det,595}}. \tag{C.8}$$

The only reported intensity for the 595 keV gamma coming from decay from the high-spin state is 32% [88]. The only absolute intensity reported for the 478 keV gamma is 6% [95], which gives a relative intensity of 12% compared to the 2033 keV gamma, which is fairly consistent with the relative intensities of 11% and 16% reported in Refs. [88, 94].

The detector efficiency was calibrated using ^{152}Eu , ^{133}Ba , ^{60}Co , ^{137}Cs , and ^{22}Na sources. The efficiency at 444 keV was found to be 0.045(5), and the efficiency at 662 keV was found to be 0.044(4). Note that these efficiencies include some unknown geometric factor, however

as only the ratio is relevant for this discussion the geometric factor is unimportant. These two efficiencies demonstrate that any difference in detector efficiency between 478 keV and 595 keV should be negligible. Furthermore, the detector efficiency reaches its maximum value <300 keV, so if anything the detector efficiency should be lower for the 595 keV peak than the 478 keV peak, which would indicate the presence of more of the high-spin state. As these calculations aim to determine an upper limit on the amount low-spin state that could have been present, it is therefore safe to take $\epsilon_{det,478} \approx \epsilon_{det,595}$. Solving Eq. (C.8) for the ratio r_1/r_2 then gives

$$\frac{r_1}{r_2} = \frac{N_{478} I_{595}}{N_{595} I_{478}} \quad (\text{C.9})$$

and the upper limit is then

$$\frac{r_1}{r_2} < \left(\frac{1169}{1560} \right) \left(\frac{0.32}{0.06} \right) = 4. \quad (\text{C.10})$$

This indicates that, although there is no clear indication of a peak at 478 keV from decay of the low-spin state of ^{68}Co , it is possible that the low-spin state could have still been present at a rate as high as four times the rate of the high-spin state. This ratio becomes even more extreme when considering decay losses in the Penning trap, as the high-spin state has a significantly shorter half-life than the low spin state (0.23(3) s and 1.6(3) s, respectively [88]). As discussed in Section 4.3.1, the RF excitation time was not the same in all measurements, however the majority of the measurements used a 100 ms RF excitation. This is also the longest excitation time used, and therefore works for the limiting-case scenario. An additional 20 ms of dipole cleaning time was used, for a total of 120 ms in the Penning trap. The final limiting-case ratio is then

$$\frac{r_1}{r_2} < \left(\frac{r_1}{r_2} \right)_0 \frac{e^{-\lambda_1 t}}{e^{-\lambda_2 t}} = (4) \frac{e^{-\ln(2) * (0.120 \text{ s} / 1.6 \text{ s})}}{e^{-\ln(2) * (0.120 \text{ s} / 0.23 \text{ s})}} \approx 5. \quad (\text{C.11})$$

The ^{68}Co TOF-ICR resonances obtained in this work therefore could have included up to five times as many low-spin ions as high-spin ions. It is still therefore highly uncertain which state was measured in this work. Given that the gamma spectrum shown in Fig. 4.8 shows clear evidence that the high-spin state was present at the germanium detector and there is no positive evidence that the low-spin state was present, the measured state is still currently believed to be the high-spin state, but any future work based on these results should be aware of these assumptions and the associated uncertainty in the state assignment.

BIBLIOGRAPHY

BIBLIOGRAPHY

- [1] M. Wang, G. Audi, F. G. Kondev, W. J. Huang, S. Naimi, and X. Xu. The AME2016 atomic mass evaluation (II). Tables, graphs and references. *Chinese Physics C*, 41(3):030003, 2017.
- [2] Klaus Blaum. High-accuracy mass spectrometry with stored ions. *Physics Reports*, 425(1):1 – 78, 2006.
- [3] Maria G. Mayer. On Closed Shells in Nuclei. *Phys. Rev.*, 74:235–239, Aug 1948.
- [4] Otto Haxel, J. Hans D. Jensen, and Hans E. Suess. On the “Magic Numbers” in Nuclear Structure. *Phys. Rev.*, 75:1766–1766, Jun 1949.
- [5] I. Talmi and I. Unna. Order of Levels in the Shell Model and Spin of Be^{11} . *Phys. Rev. Lett.*, 4:469–470, May 1960.
- [6] C. Thibault, R. Klapisch, C. Rigaud, A. M. Poskanzer, R. Prieels, L. Lessard, and W. Reisdorf. Direct measurement of the masses of ^{11}Li and $^{26-32}\text{Na}$ with an on-line mass spectrometer. *Phys. Rev. C*, 12:644–657, Aug 1975.
- [7] G. Huber, F. Touchard, S. Büttgenbach, C. Thibault, R. Klapisch, H. T. Duong, S. Liberman, J. Pinard, J. L. Vialle, P. Juncar, and P. Jacquinot. Spins, magnetic moments, and isotope shifts of $^{21-31}\text{Na}$ by high resolution laser spectroscopy of the atomic D_1 line. *Phys. Rev. C*, 18:2342–2354, Nov 1978.
- [8] C. Détraz, D. Guillemaud, G. Huber, R. Klapisch, M. Langevin, F. Naulin, C. Thibault, L. C. Carraz, and F. Touchard. Beta decay of $^{27-32}\text{Na}$ and their descendants. *Phys. Rev. C*, 19:164–176, Jan 1979.
- [9] D. Guillemaud-Mueller, C. Detraz, M. Langevin, F. Naulin, M. de Saint-Simon, C. Thibault, F. Touchard, and M. Epherre. β -Decay schemes of very neutron-rich sodium isotopes and their descendants. *Nuclear Physics A*, 426(1):37 – 76, 1984.
- [10] Takaharu Otsuka, Toshio Suzuki, Rintaro Fujimoto, Hubert Grawe, and Yoshinori Akaishi. Evolution of Nuclear Shells due to the Tensor Force. *Phys. Rev. Lett.*, 95:232502, Nov 2005.
- [11] A. P. Zuker. Three-Body Monopole Corrections to Realistic Interactions. *Phys. Rev. Lett.*, 90:042502, Jan 2003.

- [12] Takaharu Otsuka, Toshio Suzuki, Jason D. Holt, Achim Schwenk, and Yoshinori Akaishi. Three-Body Forces and the Limit of Oxygen Isotopes. *Phys. Rev. Lett.*, 105:032501, Jul 2010.
- [13] K. Hebeler, J.D. Holt, J. Menndez, and A. Schwenk. Nuclear Forces and Their Impact on Neutron-Rich Nuclei and Neutron-Rich Matter. *Annual Review of Nuclear and Particle Science*, 65(1):457–484, 2015.
- [14] H. Savajols. The SPEG Mass Measurement Program at GANIL. *Hyperfine Interactions*, 132(1):243–252, Jan 2001.
- [15] J.M. Wouters, D.J. Vieira, H. Wollnik, G.W. Butler, R.H. Kraus, and K. Vaziri. The Time-Of-Flight Isochronous (TOFI) spectrometer for direct mass measurements of exotic light nuclei. *Nuclear Instruments and Methods in Physics Research Section B: Beam Interactions with Materials and Atoms*, 26(1):286 – 293, 1987.
- [16] D. Bazin, J.A. Caggiano, B.M. Sherrill, J. Yurkon, and A. Zeller. The S800 spectrograph. *Nuclear Instruments and Methods in Physics Research Section B: Beam Interactions with Materials and Atoms*, 204:629 – 633, 2003. 14th International Conference on Electromagnetic Isotope Separators and Techniques Related to their Applications.
- [17] S. Michimasa, M. Kobayashi, Y. Kiyokawa, S. Ota, D. S. Ahn, H. Baba, G. P. A. Berg, M. Dozono, N. Fukuda, T. Furuno, E. Ideguchi, N. Inabe, T. Kawabata, S. Kawase, K. Kisamori, K. Kobayashi, T. Kubo, Y. Kubota, C. S. Lee, M. Matsushita, H. Miya, A. Mizukami, H. Nagakura, D. Nishimura, H. Oikawa, H. Sakai, Y. Shimizu, A. Stolz, H. Suzuki, M. Takaki, H. Takeda, S. Takeuchi, H. Tokieda, T. Uesaka, K. Yako, Y. Yamaguchi, Y. Yanagisawa, R. Yokoyama, K. Yoshida, and S. Shimoura. Magic Nature of Neutrons in ^{54}Ca : First Mass Measurements of $^{55-57}\text{Ca}$. *Phys. Rev. Lett.*, 121:022506, Jul 2018.
- [18] A. S. Lalleman, G. Auger, W. Mittig, M. Chabert, M. Chartier, J. Fermé, A. Gillibert, A. Lépine-Szily, M. Lewitowicz, M. H. Moscatello, N. A. Orr, G. Politi, F. Sarazin, H. Savajols, P. Van Isacker, and A. C. C. Villari. Mass Measurements of Exotic Nuclei around $N=Z=40$ with CSS2. *Hyperfine Interactions*, 132(1):313–320, Jan 2001.
- [19] S. Issmer, M. Fruneau, J.A. Pinston, M. Asghar, D. Barnéoud, J. Genevey, Th. Kersch, and K.E.G. Löbner. Direct mass measurements of $A=80$ isobars. *The European Physical Journal A - Hadrons and Nuclei*, 2(2):173–177, Jun 1998.
- [20] Bernhard Franzke. The heavy ion storage and cooler ring project ESR at GSI. *Nuclear Instruments and Methods in Physics Research Section B: Beam Interactions with Materials and Atoms*, 24-25:18 – 25, 1987.
- [21] J.W. Xia, W.L. Zhan, B.W. Wei, Y.J. Yuan, M.T. Song, W.Z. Zhang, X.D. Yang, P. Yuan, D.Q. Gao, H.W. Zhao, X.T. Yang, G.Q. Xiao, K.T. Man, J.R. Dang, X.H. Cai,

- Y.F. Wang, J.Y. Tang, W.M. Qiao, Y.N. Rao, Y. He, L.Z. Mao, and Z.Z. Zhou. The heavy ion cooler-storage-ring project (HIRFL-CSR) at Lanzhou. *Nuclear Instruments and Methods in Physics Research Section A: Accelerators, Spectrometers, Detectors and Associated Equipment*, 488(1):11 – 25, 2002.
- [22] Robert N. Wolf, Markus Eritt, Gerrit Marx, and Lutz Schweikhard. A multi-reflection time-of-flight mass separator for isobaric purification of radioactive ion beams. *Hyperfine Interactions*, 199(1):115–122, Jul 2011.
- [23] Christian Jesch, Timo Dickel, Wolfgang R. Plaß, Devin Short, Samuel Ayet San Andres, Jens Dilling, Hans Geissel, Florian Greiner, Johannes Lang, Kyle G. Leach, Wayne Lippert, Christoph Scheidenberger, and Mikhail I. Yavor. The MR-TOF-MS isobar separator for the TITAN facility at TRIUMF. *Hyperfine Interactions*, 235(1):97–106, Nov 2015.
- [24] T. Dickel, W.R. Plaß, A. Becker, U. Czok, H. Geissel, E. Haettner, C. Jesch, W. Kinsel, M. Petrick, C. Scheidenberger, A. Simon, and M.I. Yavor. A high-performance multiple-reflection time-of-flight mass spectrometer and isobar separator for the research with exotic nuclei. *Nuclear Instruments and Methods in Physics Research Section A: Accelerators, Spectrometers, Detectors and Associated Equipment*, 777:172 – 188, 2015.
- [25] P. Schury, M. Wada, Y. Ito, D. Kaji, F. Arai, M. MacCormick, I. Murray, H. Haba, S. Jeong, S. Kimura, H. Koura, H. Miyatake, K. Morimoto, K. Morita, A. Ozawa, M. Rosenbusch, M. Reponen, P.-A. Söderström, A. Takamine, T. Tanaka, and H. Wollnik. First online multireflection time-of-flight mass measurements of isobar chains produced by fusion-evaporation reactions: Toward identification of superheavy elements via mass spectroscopy. *Phys. Rev. C*, 95:011305, Jan 2017.
- [26] F. Wienholtz, D. Beck, K. Blaum, Ch Borgmann, M. Breitenfeldt, R. B. Cakirli, S. George, F. Herfurth, J. D. Holt, M. Kowalska, S. Kreim, D. Lunney, V. Manea, J. Menéndez, D. Neidherr, M. Rosenbusch, L. Schweikhard, A. Schwenk, J. Simonis, J. Stanja, R. N. Wolf, and K. Zuber. Masses of exotic calcium isotopes pin down nuclear forces. *Nature*, 498:346 – 349, Jun 2013.
- [27] Edmund G. Myers. The most precise atomic mass measurements in Penning traps. *International Journal of Mass Spectrometry*, 349-350:107 – 122, 2013. 100 years of Mass Spectrometry.
- [28] A. A. Valverde, G. Bollen, M. Brodeur, R. A. Bryce, K. Cooper, M. Eibach, K. Gulyuz, C. Izzo, D. J. Morrissey, M. Redshaw, R. Ringle, R. Sandler, S. Schwarz, C. S. Sumithrarachchi, and A. C. C. Villari. First Direct Determination of the Superallowed β -Decay Q_{EC} Value for ^{14}O . *Phys. Rev. Lett.*, 114:232502, Jun 2015.

- [29] G Bollen, S Becker, H.-J Kluge, M König, R.B Moore, T Otto, H Raimbault-Hartmann, G Savard, L Schweikhard, and H Stolzenberg. ISOLTRAP: a tandem Penning trap system for accurate on-line mass determination of short-lived isotopes. *Nuclear Instruments and Methods in Physics Research Section A: Accelerators, Spectrometers, Detectors and Associated Equipment*, 368(3):675 – 697, 1996.
- [30] V.S. Kolhinen, T. Eronen, J. Hakala, A. Jokinen, S. Kopecky, S. Rinta-Antila, J. Szerypo, and J. yst. Penning trap for isobaric mass separation at IGISOL. *Nuclear Instruments and Methods in Physics Research Section B: Beam Interactions with Materials and Atoms*, 204:502 – 506, 2003. 14th International Conference on Electromagnetic Isotope Separators and Techniques Related to their Applications.
- [31] G. Savard, R.C. Barber, D. Beeching, F. Buchinger, J.E. Crawford, S. Gulick, X. Feng, E. Hagberg, J.C. Hardy, V.T. Koslowsky, J.K.P. Lee, R.B. Moore, K.S. Sharma, and M. Watson. The Canadian Penning trap mass spectrometer. *Nuclear Physics A*, 626(1):353 – 356, 1997. Proceedings of the Third International Conference on Nuclear Physics at Storage Rings.
- [32] G. Sikler, D. Ackermann, F. Attallah, D. Beck, J. Dilling, S.A. Elisseev, H. Geissel, D. Habs, S. Heinz, F. Herfurth, F. Heberger, S. Hofmann, H.-J. Kluge, C. Kozhuharov, G. Marx, M. Mukherjee, J. Neumayr, W.R. Pla, W. Quint, S. Rahaman, D. Rodriguez, C. Scheidenberger, M. Tarisien, P. Thirolf, V. Varentsov, C. Weber, and Z. Zhou. First on-line test of SHIPTRAP. *Nuclear Instruments and Methods in Physics Research Section B: Beam Interactions with Materials and Atoms*, 204:482 – 486, 2003. 14th International Conference on Electromagnetic Isotope Separators and Techniques Related to their Applications.
- [33] Ryan Ringle, Stefan Schwarz, and Georg Bollen. Penning trap mass spectrometry of rare isotopes produced via projectile fragmentation at the LEBIT facility. *International Journal of Mass Spectrometry*, 349-350:87 – 93, 2013. 100 years of Mass Spectrometry.
- [34] A. A. Kwiatkowski, C. Andreoiu, J. C. Bale, T. Brunner, A. Chaudhuri, U. Chowdhury, P. Delheij, S. Ettenauer, D. Frekers, A. T. Gallant, A. Grossheim, G. Gwinner, F. Jang, A. Lennarz, T. Ma, E. Mané, M. R. Pearson, B. E. Schultz, M. C. Simon, V. V. Simon, and J. Dilling. TITAN: An ion trap facility for on-line mass measurement experiments. *Hyperfine Interactions*, 225(1):143–155, Jan 2014.
- [35] A. A. Valverde, M. Brodeur, G. Bollen, M. Eibach, K. Gulyuz, A. Hamaker, C. Izzo, W.-J. Ong, D. Puentes, M. Redshaw, R. Ringle, R. Sandler, S. Schwarz, C. S. Sumithrarachchi, J. Surbrook, A. C. C. Villari, and I. T. Yandow. High-Precision Mass Measurement of ^{56}Cu and the Redirection of the rp -Process Flow. *Phys. Rev. Lett.*, 120:032701, Jan 2018.
- [36] H. Raimbault-Hartmann, D. Beck, G. Bollen, M. Knig, H.-J. Kluge, E. Schark, J. Stein, S. Schwarz, and J. Szerypo. A cylindrical Penning trap for capture, mass selective

- cooling, and bunching of radioactive ion beams. *Nuclear Instruments and Methods in Physics Research Section B: Beam Interactions with Materials and Atoms*, 126(1):378 – 382, 1997. International Conference on Electromagnetic Isotope Separators and Techniques Related to Their Applications.
- [37] G. Gabrielse, L. Haarsma, and S.L. Rolston. Open-endcap Penning traps for high precision experiments. *International Journal of Mass Spectrometry and Ion Processes*, 88(2):319 – 332, 1989.
- [38] Lowell S. Brown and Gerald Gabrielse. Geonium theory: Physics of a single electron or ion in a Penning trap. *Rev. Mod. Phys.*, 58:233–311, Jan 1986.
- [39] G. Gabrielse. Why Is Sideband Mass Spectrometry Possible with Ions in a Penning Trap? *Phys. Rev. Lett.*, 102:172501, Apr 2009.
- [40] M. König, G. Bollen, H.-J. Kluge, T. Otto, and J. Szerypo. Quadrupole excitation of stored ion motion at the true cyclotron frequency. *International Journal of Mass Spectrometry and Ion Processes*, 142(1):95 – 116, 1995.
- [41] R. Ringle. *High-Precision Mass Measurement of ^{38}Ca and Development of the LEBIT 9.4-T Penning Trap System*. PhD thesis, Michigan State University, 2013.
- [42] Marshall Alan G., Hendrickson Christopher L., and Jackson George S. Fourier transform ion cyclotron resonance mass spectrometry: A primer. *Mass Spectrometry Reviews*, 17(1):1–35, 1998.
- [43] S. Eliseev, K. Blaum, M. Block, C. Droese, M. Goncharov, E. Minaya Ramirez, D. A. Nesterenko, Yu. N. Novikov, and L. Schweikhard. Phase-Imaging Ion-Cyclotron-Resonance Measurements for Short-Lived Nuclides. *Phys. Rev. Lett.*, 110:082501, Feb 2013.
- [44] R. Ringle, G. Bollen, A. Prinke, J. Savory, P. Schury, S. Schwarz, and T. Sun. The LEBIT 9.4T Penning trap mass spectrometer. *Nuclear Instruments and Methods in Physics Research Section A: Accelerators, Spectrometers, Detectors and Associated Equipment*, 604(3):536 – 547, 2009.
- [45] S. George, K. Blaum, F. Herfurth, A. Herlert, M. Kretschmar, S. Nagy, S. Schwarz, L. Schweikhard, and C. Yazidjian. The Ramsey method in high-precision mass spectrometry with Penning traps: Experimental results. *International Journal of Mass Spectrometry*, 264(2):110 – 121, 2007.
- [46] S. Ulmer, C. Smorra, A. Mooser, K. Franke, H. Nagahama, G. Schneider, T. Higuchi, S. Van Gorp, K. Blaum, Y. Matsuda, W. Quint, J. Walz, and Y. Yamazaki. High-precision comparison of the antiproton-to-proton charge-to-mass ratio. *Nature*, 524:196 EP –, Aug 2015.

- [47] C. Smorra, S. Sellner, M. J. Borchert, J. A. Harrington, T. Higuchi, H. Nagahama, T. Tanaka, A. Mooser, G. Schneider, M. Bohman, K. Blaum, Y. Matsuda, C. Ospelkaus, W. Quint, J. Walz, Y. Yamazaki, and S. Ulmer. A parts-per-billion measurement of the antiproton magnetic moment. *Nature*, 550:371 EP –, Oct 2017.
- [48] D. Hanneke, S. Fogwell, and G. Gabrielse. New Measurement of the Electron Magnetic Moment and the Fine Structure Constant. *Phys. Rev. Lett.*, 100:120801, Mar 2008.
- [49] S. Sturm, A. Wagner, B. Schabinger, J. Zatorski, Z. Harman, W. Quint, G. Werth, C. H. Keitel, and K. Blaum. g Factor of Hydrogenlike $^{28}\text{Si}^{13+}$. *Phys. Rev. Lett.*, 107:023002, Jul 2011.
- [50] R. Ringle, G. Bollen, A. Prinke, J. Savory, P. Schury, S. Schwarz, and T. Sun. A “Lorentz” steerer for ion injection into a Penning trap. *International Journal of Mass Spectrometry*, 263(1):38 – 44, 2007.
- [51] P. Duhamel and M. Vetterli. Fast fourier transforms: A tutorial review and a state of the art. *Signal Processing*, 19(4):259 – 299, 1990.
- [52] J.B. Jeffries, S.E. Barlow, and G.H. Dunn. Theory of space-charge shift of ion cyclotron resonance frequencies. *International Journal of Mass Spectrometry and Ion Processes*, 54(1):169 – 187, 1983.
- [53] G. Bollen, R. B. Moore, G. Savard, and H. Stolzenberg. The accuracy of heavyion mass measurements using time of flight ion cyclotron resonance in a Penning trap. *Journal of Applied Physics*, 68(9):4355–4374, 1990.
- [54] D.J. Morrissey, B.M. Sherrill, M. Steiner, A. Stolz, and I. Wiedenhoever. Commissioning the A1900 projectile fragment separator. *Nuclear Instruments and Methods in Physics Research Section B: Beam Interactions with Materials and Atoms*, 204:90 – 96, 2003. 14th International Conference on Electromagnetic Isotope Separators and Techniques Related to their Applications.
- [55] K. Minamisono, P.F. Mantica, A. Klose, S. Vinnikova, A. Schneider, B. Johnson, and B.R. Barquest. Commissioning of the collinear laser spectroscopy system in the BECOLA facility at NSCL. *Nuclear Instruments and Methods in Physics Research Section A: Accelerators, Spectrometers, Detectors and Associated Equipment*, 709:85 – 94, 2013.
- [56] O Kester, D Bazin, C Benatti, J Bierwagen, G Bollen, Suzane Bricker, A C Crawford, S Chouhan, Cyle Compton, K Davidson, J Delauter, M Doleans, Lindsay Dubbs, K Elliott, A Lapierre, W Hartung, M Johnson, Shannon Krause, F Marti, and J Schmidt. ReA3 - The rare isotope reaccelerator at MSU. 01 2010.

- [57] K. Cooper, C.S. Sumithrarachchi, D.J. Morrissey, A. Levand, J.A. Rodriguez, G. Savard, S. Schwarz, and B. Zabransky. Extraction of thermalized projectile fragments from a large volume gas cell. *Nuclear Instruments and Methods in Physics Research Section A: Accelerators, Spectrometers, Detectors and Associated Equipment*, 763:543 – 546, 2014.
- [58] S. Schwarz, G. Bollen, S. Chouhan, J.J. Das, M. Green, C. Magsig, D.J. Morrissey, J. Ottarson, C. Sumithrarachchi, A.C.C. Villari, and A. Zeller. The NSCL cyclotron gas stopper Entering commissioning. *Nuclear Instruments and Methods in Physics Research Section B: Beam Interactions with Materials and Atoms*, 376:256 – 259, 2016. Proceedings of the XVIIth International Conference on Electromagnetic Isotope Separators and Related Topics (EMIS2015), Grand Rapids, MI, U.S.A., 11-15 May 2015.
- [59] C. Izzo, G. Bollen, S. Bustabad, M. Eibach, K. Gulyuz, D.J. Morrissey, M. Redshaw, R. Ringle, R. Sandler, S. Schwarz, and A.A. Valverde. A laser ablation source for offline ion production at LEBIT. *Nuclear Instruments and Methods in Physics Research Section B: Beam Interactions with Materials and Atoms*, 376:60 – 63, 2016. Proceedings of the XVIIth International Conference on Electromagnetic Isotope Separators and Related Topics (EMIS2015), Grand Rapids, MI, U.S.A., 11-15 May 2015.
- [60] N. D. Gamage, G. Bollen, M. Eibach, K. Gulyuz, C. Izzo, R. M. E. B. Kandegedara, M. Redshaw, R. Ringle, R. Sandler, and A. A. Valverde. Precise determination of the ^{113}Cd fourth-forbidden non-unique β -decay Q value. *Phys. Rev. C*, 94:025505, Aug 2016.
- [61] R. M. E. B. Kandegedara, G. Bollen, M. Eibach, N. D. Gamage, K. Gulyuz, C. Izzo, M. Redshaw, R. Ringle, R. Sandler, and A. A. Valverde. β -decay Q values among the $A = 50$ Ti-V-Cr isobaric triplet and atomic masses of $^{46,47,49,50}\text{Ti}$, $^{50,51}\text{V}$, and $^{50,52-54}\text{Cr}$. *Phys. Rev. C*, 96:044321, Oct 2017.
- [62] K. Gulyuz, J. Ariche, G. Bollen, S. Bustabad, M. Eibach, C. Izzo, S. J. Novario, M. Redshaw, R. Ringle, R. Sandler, S. Schwarz, and A. A. Valverde. Determination of the direct double- β -decay Q value of ^{96}Zr and atomic masses of $^{90-92,94,96}\text{Zr}$ and $^{92,94-98,100}\text{Mo}$. *Phys. Rev. C*, 91:055501, May 2015.
- [63] M. Eibach, G. Bollen, K. Gulyuz, C. Izzo, M. Redshaw, R. Ringle, R. Sandler, and A. A. Valverde. Double resonant enhancement in the neutrinoless double-electron capture of ^{190}Pt . *Phys. Rev. C*, 94:015502, Jul 2016.
- [64] Matthew Redshaw, Georg Bollen, Maxime Brodeur, Scott Bustabad, David L. Lincoln, Samuel J. Novario, Ryan Ringle, and Stefan Schwarz. Atomic mass and double- β -decay Q value of ^{48}Ca . *Phys. Rev. C*, 86:041306, Oct 2012.

- [65] S. Bustabad, G. Bollen, M. Brodeur, D. L. Lincoln, S. J. Novario, M. Redshaw, R. Ringle, S. Schwarz, and A. A. Valverde. First direct determination of the ^{48}Ca double- β decay Q value. *Phys. Rev. C*, 88:022501, Aug 2013.
- [66] S. Bustabad, G. Bollen, M. Brodeur, D. L. Lincoln, S. J. Novario, M. Redshaw, R. Ringle, and S. Schwarz. Examination of the possible enhancement of neutrinoless double-electron capture in ^{78}Kr . *Phys. Rev. C*, 88:035502, Sep 2013.
- [67] David L. Lincoln, Jason D. Holt, Georg Bollen, Maxime Brodeur, Scott Bustabad, Jonathan Engel, Samuel J. Novario, Matthew Redshaw, Ryan Ringle, and Stefan Schwarz. First Direct Double- β Decay Q -Value Measurement of ^{82}Se in Support of Understanding the Nature of the Neutrino. *Phys. Rev. Lett.*, 110:012501, Jan 2013.
- [68] S. Schwarz, G. Bollen, R. Ringle, J. Savory, and P. Schury. The LEBIT ion cooler and buncher. *Nuclear Instruments and Methods in Physics Research Section A: Accelerators, Spectrometers, Detectors and Associated Equipment*, 816:131 – 141, 2016.
- [69] P. Schury, G. Bollen, M. Block, D. J. Morrissey, R. Ringle, A. Prinke, J. Savory, S. Schwarz, and T. Sun. Beam purification techniques for low energy rare isotope beams from a gas cell. *Hyperfine Interactions*, 173(1):165–170, Nov 2006.
- [70] N. R. Daly. Scintillation Type Mass Spectrometer Ion Detector. *Review of Scientific Instruments*, 31(3):264–267, 1960.
- [71] C. Izzo, G. Bollen, M. Brodeur, M. Eibach, K. Gulyuz, J. D. Holt, J. M. Kelly, M. Redshaw, R. Ringle, R. Sandler, S. Schwarz, S. R. Stroberg, C. S. Sumithrarachchi, A. A. Valverde, and A. C. C. Villari. Precision mass measurements of neutron-rich Co isotopes beyond $N = 40$. *Phys. Rev. C*, 97:014309, Jan 2018.
- [72] R. Broda, B. Fornal, W. Królas, T. Pawłat, D. Bazzacco, S. Lunardi, C. Rossi-Alvarez, R. Menegazzo, G. de Angelis, P. Bednarczyk, J. Rico, D. De Acuña, P. J. Daly, R. H. Mayer, M. Sferrazza, H. Grawe, K. H. Maier, and R. Schubart. $N = 40$ Neutron Subshell Closure in the ^{68}Ni Nucleus. *Phys. Rev. Lett.*, 74:868–871, Feb 1995.
- [73] O. Sorlin, S. Leenhardt, C. Donzaud, J. Duprat, F. Azaiez, F. Nowacki, H. Grawe, Zs. Dombrádi, F. Amorini, A. Astier, D. Baiborodin, M. Bellegric, C. Borcea, C. Bourgeois, D. M. Cullen, Z. Dlouhy, E. Dragulescu, M. Górska, S. Grévy, D. Guillemaud-Mueller, G. Hagemann, B. Herskind, J. Kiener, R. Lemmon, M. Lewitowicz, S. M. Lukyanov, P. Mayet, F. de Oliveira Santos, D. Pantalica, Yu.-E. Penionzhkevich, F. Pougheon, A. Poves, N. Redon, M. G. Saint-Laurent, J. A. Scarpaci, G. Sletten, M. Stanoiu, O. Tarasov, and Ch. Theisen. $^{68}\text{Ni}_{40}$: Magicity versus Superfluidity. *Phys. Rev. Lett.*, 88:092501, Feb 2002.

- [74] B. Pritychenko, M. Birch, B. Singh, and M. Horoi. Tables of E2 transition probabilities from the first 2+ states in even-even nuclei. *Atomic Data and Nuclear Data Tables*, 107:1 – 139, 2016.
- [75] H Grawe and M Lewitowicz. Shell structure of nuclei far from stability. 693:116–132, 10 2001.
- [76] K. Langanke, J. Terasaki, F. Nowacki, D. J. Dean, and W. Nazarewicz. How magic is the magic ^{68}Ni nucleus? *Phys. Rev. C*, 67:044314, Apr 2003.
- [77] D. Lunney, J. M. Pearson, and C. Thibault. Recent trends in the determination of nuclear masses. *Rev. Mod. Phys.*, 75:1021–1082, Aug 2003.
- [78] A. Bohr, B. R. Mottelson, and D. Pines. Possible Analogy between the Excitation Spectra of Nuclei and Those of the Superconducting Metallic State. *Phys. Rev.*, 110:936–938, May 1958.
- [79] D. J. Dean and M. Hjorth-Jensen. Pairing in nuclear systems: from neutron stars to finite nuclei. *Rev. Mod. Phys.*, 75:607–656, Apr 2003.
- [80] C. F. von Weizsäcker. Zur Theorie der Kernmassen. *Z. Phys.*, 96:431, Jul 1935.
- [81] C. Guénaut, G. Audi, D. Beck, K. Blaum, G. Bollen, P. Delahaye, F. Herfurth, A. Kellerbauer, H.-J. Kluge, J. Libert, D. Lunney, S. Schwarz, L. Schweikhard, and C. Yazidjian. High-precision mass measurements of nickel, copper, and gallium isotopes and the purported shell closure at $N = 40$. *Phys. Rev. C*, 75:044303, Apr 2007.
- [82] S. Rahaman, J. Hakala, V. V. Elomaa, T. Eronen, U. Hager, A. Jokinen, A. Kankainen, I. D. Moore, H. Penttilä, S. Rinta-Antila, J. Rissanen, A. Saastamoinen, C. Weber, and J. Äystö. Masses of neutron-rich Ni and Cu isotopes and the shell closure at $Z = 28$, $N = 40$. *The European Physical Journal A*, 34(1):5–9, Oct 2007.
- [83] R. Ferrer, M. Block, C. Bachelet, B. R. Barquest, G. Bollen, C. M. Campbell, M. Facina, C. M. Folden, C. Guénaut, A. A. Kwiatkowski, D. L. Lincoln, D. J. Morrissey, G. K. Pang, A. M. Prinke, R. Ringle, J. Savory, P. Schury, and S. Schwarz. Penning trap mass spectrometry of neutron-rich Fe and Co isotopes around $N = 40$ with the LEBIT mass spectrometer. *Phys. Rev. C*, 81:044318, Apr 2010.
- [84] R. Graham Cooks. Special feature: Historical. Collision-induced dissociation: Readings and commentary. *Journal of Mass Spectrometry*, 30(9):1215–1221.
- [85] Andrew R. Johnson and Erin E. Carlson. Collision-Induced Dissociation Mass Spectrometry: A Powerful Tool for Natural Product Structure Elucidation. *Analytical Chemistry*, 87(21):10668–10678, 2015.

- [86] J. Mitchell Wells and Scott A. McLuckey. Collision-Induced Dissociation (CID) of Peptides and Proteins. In *Biological Mass Spectrometry*, volume 402 of *Methods in Enzymology*, pages 148 – 185. Academic Press, 2005.
- [87] A.A. Kwiatkowski, G. Bollen, M. Redshaw, R. Ringle, and S. Schwarz. Isobaric beam purification for high precision Penning trap mass spectrometry of radioactive isotope beams with SWIFT. *International Journal of Mass Spectrometry*, 379:9 – 15, 2015.
- [88] W. F. Mueller, B. Bruyneel, S. Franchoo, M. Huyse, J. Kurpeta, K. Kruglov, Y. Kudryavtsev, N. V. S. V. Prasad, R. Raabe, I. Reusen, P. Van Duppen, J. Van Roosbroeck, L. Vermeeren, L. Weissman, Z. Janas, M. Karny, T. Kszczot, A. Płochocki, K.-L. Kratz, B. Pfeiffer, H. Grawe, U. Köster, P. Thirolf, and W. B. Walters. β decay of ^{66}Co , ^{68}Co , and ^{70}Co . *Phys. Rev. C*, 61:054308, Apr 2000.
- [89] S. N. Liddick, W. B. Walters, C. J. Chiara, R. V. F. Janssens, B. Abromeit, A. Ayres, A. Bey, C. R. Bingham, M. P. Carpenter, L. Cartegni, J. Chen, H. L. Crawford, I. G. Darby, R. Grzywacz, J. Harker, C. R. Hoffman, S. Ilyushkin, F. G. Kondev, N. Larson, M. Madurga, D. Miller, S. Padgett, S. V. Paulauskas, M. M. Rajabali, K. Rykaczewski, D. Seweryniak, S. Suchyta, and S. Zhu. Analogous intruder behavior near Ni, Sn, and Pb isotopes. *Phys. Rev. C*, 92:024319, Aug 2015.
- [90] M. Block, C. Bachelet, G. Bollen, M. Facina, C. M. Folden, C. Guénaut, A. A. Kwiatkowski, D. J. Morrissey, G. K. Pang, A. Prinke, R. Ringle, J. Savory, P. Schury, and S. Schwarz. Discovery of a Nuclear Isomer in ^{65}Fe with PenningTrap Mass Spectrometry. *Phys. Rev. Lett.*, 100:132501, Apr 2008.
- [91] A. A. Valverde, G. Bollen, K. Cooper, M. Eibach, K. Gulyuz, C. Izzo, D. J. Morrissey, R. Ringle, R. Sandler, S. Schwarz, C. S. Sumithrarachchi, and A. C. C. Villari. Penning trap mass measurement of ^{72}Br . *Phys. Rev. C*, 91:037301, Mar 2015.
- [92] A. Kramida, Yu. Ralchenko, J. Reader, and and NIST ASD Team. NIST Atomic Spectra Database (ver. 5.3), [Online]. Available: <http://physics.nist.gov/asd> [2016, December 21]. National Institute of Standards and Technology, Gaithersburg, MD., 2015.
- [93] Raymond T. Birge. The Calculation of Errors by the Method of Least Squares. *Phys. Rev.*, 40:207–227, Apr 1932.
- [94] F. Flavigny, D. Pauwels, D. Radulov, I. J. Darby, H. De Witte, J. Diriken, D. V. Fedorov, V. N. Fedosseev, L. M. Fraile, M. Huyse, V. S. Ivanov, U. Köster, B. A. Marsh, T. Otsuka, L. Popescu, R. Raabe, M. D. Seliverstov, N. Shimizu, A. M. Sjödin, Y. Tsunoda, P. Van den Bergh, P. Van Duppen, J. Van de Walle, M. Venhart, W. B. Walters, and K. Wimmer. Characterization of the low-lying 0^+ and 2^+ states in ^{68}Ni via β decay of the low-spin ^{68}Co isomer. *Phys. Rev. C*, 91:034310, Mar 2015.

- [95] C. J. Prokop. *Shape coexistence in the neutron-rich nickel isotopes near $N=40$* . PhD thesis, Michigan State University, 2016.
- [96] M. H. Brennan and A. M. Bernstein. jj Coupling Model in Odd-Odd Nuclei. *Phys. Rev.*, 120:927–933, Nov 1960.
- [97] S. N. Liddick, B. Abromeit, A. Ayres, A. Bey, C. R. Bingham, M. Bolla, L. Cartegni, H. L. Crawford, I. G. Darby, R. Grzywacz, S. Ilyushkin, N. Larson, M. Madurga, D. Miller, S. Padgett, S. Paulauskas, M. M. Rajabali, K. Rykaczewski, and S. Suchyta. Low-energy structure of ${}^{66}_{27}\text{Co}_{39}$ and ${}^{68}_{27}\text{Co}_{41}$ populated through β decay. *Phys. Rev. C*, 85:014328, Jan 2012.
- [98] D. Pauwels, O. Ivanov, N. Bree, J. Büscher, T. E. Cocolios, J. Gentens, M. Huyse, A. Korgul, Yu. Kudryavtsev, R. Raabe, M. Sawicka, I. Stefanescu, J. Van de Walle, P. Van den Bergh, P. Van Duppen, and W. B. Walters. Shape isomerism at $N = 40$: Discovery of a proton intruder state in ${}^{67}\text{Co}$. *Phys. Rev. C*, 78:041307, Oct 2008.
- [99] K. Tsukiyama, S. K. Bogner, and A. Schwenk. In-medium similarity renormalization group for open-shell nuclei. *Phys. Rev. C*, 85:061304, Jun 2012.
- [100] S. K. Bogner, H. Hergert, J. D. Holt, A. Schwenk, S. Binder, A. Calci, J. Langhammer, and R. Roth. Nonperturbative Shell-Model Interactions from the In-Medium Similarity Renormalization Group. *Phys. Rev. Lett.*, 113:142501, Oct 2014.
- [101] S. R. Stroberg, H. Hergert, J. D. Holt, S. K. Bogner, and A. Schwenk. Ground and excited states of doubly open-shell nuclei from ab initio valence-space Hamiltonians. *Phys. Rev. C*, 93:051301, May 2016.
- [102] H. Hergert, S.K. Bogner, T.D. Morris, A. Schwenk, and K. Tsukiyama. The In-Medium Similarity Renormalization Group: A novel ab initio method for nuclei. *Physics Reports*, 621:165 – 222, 2016. Memorial Volume in Honor of Gerald E. Brown.
- [103] S. R. Stroberg, A. Calci, H. Hergert, J. D. Holt, S. K. Bogner, R. Roth, and A. Schwenk. Nucleus-Dependent Valence-Space Approach to Nuclear Structure. *Phys. Rev. Lett.*, 118:032502, Jan 2017.
- [104] E. Epelbaum, H.-W. Hammer, and Ulf-G. Meißner. Modern theory of nuclear forces. *Rev. Mod. Phys.*, 81:1773–1825, Dec 2009.
- [105] R. Machleidt and D.R. Entem. Chiral effective field theory and nuclear forces. *Physics Reports*, 503(1):1 – 75, 2011.
- [106] S.K. Bogner, R.J. Furnstahl, and A. Schwenk. From low-momentum interactions to nuclear structure. *Progress in Particle and Nuclear Physics*, 65(1):94 – 147, 2010.

- [107] K. Hebeler, S. K. Bogner, R. J. Furnstahl, A. Nogga, and A. Schwenk. Improved nuclear matter calculations from chiral low-momentum interactions. *Phys. Rev. C*, 83:031301, Mar 2011.
- [108] J. Simonis, K. Hebeler, J. D. Holt, J. Menéndez, and A. Schwenk. Exploring *sd*-shell nuclei from two- and three-nucleon interactions with realistic saturation properties. *Phys. Rev. C*, 93:011302, Jan 2016.
- [109] J. Simonis, S. R. Stroberg, K. Hebeler, J. D. Holt, and A. Schwenk. Saturation with chiral interactions and consequences for finite nuclei. *Phys. Rev. C*, 96:014303, Jul 2017.
- [110] T. D. Morris, J. Simonis, S. R. Stroberg, C. Stumpf, G. Hagen, J. D. Holt, G. R. Jansen, T. Papenbrock, R. Roth, and A. Schwenk. Structure of the Lightest Tin Isotopes. *Phys. Rev. Lett.*, 120:152503, Apr 2018.
- [111] T. D. Morris, N. M. Parzuchowski, and S. K. Bogner. Magnus expansion and in-medium similarity renormalization group. *Phys. Rev. C*, 92:034331, Sep 2015.
- [112] B.A. Brown and W.D.M. Rae. The Shell-Model Code NuShellX@MSU. *Nuclear Data Sheets*, 120:115 – 118, 2014.
- [113] J. B. Johnson. Thermal Agitation of Electricity in Conductors. *Phys. Rev.*, 32:97–109, Jul 1928.
- [114] David A Dahl. SIMION for the personal computer in reflection. *International Journal of Mass Spectrometry*, 200(1):3 – 25, 2000. Volume 200: The state of the field as we move into a new millenium.
- [115] A. A. Valverde. SIPTCryocooler. Technical report, 2014.
- [116] J. Savory. *High-Precision Mass Measurement of $N \approx Z \approx 34$ Nuclides for rp -Process Simulations and Developments for the LEBIT Facility*. PhD thesis, Michigan State University, 2009.
- [117] D. L. Lincoln. *First Direct Double-Beta Decay Q -Value Measurement of the Neutrinoless Double-Beta Decay Candidate ^{82}Se and Development of a High-Precision Magnetometer*. PhD thesis, Michigan State University, 2013.
- [118] O. Helene. Upper limit of peak area. *Nuclear Instruments and Methods in Physics Research*, 212(1):319 – 322, 1983.